

# OXYGEN ADSORPTION AND PHOTOCONDUCTION MODELS FOR METAL OXIDE PHOTODETECTORS

**Amelia Peterson**

Submitted in Partial Fulfillment of the Requirements  
for the Degree of

*DOCTOR OF PHILOSOPHY*

Approved by:  
Dr. Shayla Sawyer, Chair  
Dr. Michael Shur  
Dr. Paul Chow  
Dr. Joel Plawsky



*Department of Electrical and Computer Systems Engineering*  
Rensselaer Polytechnic Institute  
Troy, New York

[May 2022]  
Submitted April 2022

# CONTENTS

LIST OF TABLES.....	v
LIST OF FIGURES .....	vii
ACKNOWLEDGEMENTS.....	xiii
DEDICATION.....	xiv
ABSTRACT.....	xv
1. INTRODUCTION .....	1
1.1 Bacterial Fluorescence Detection.....	1
1.2 Metal Oxide UV Photodetectors.....	2
1.3 Thesis Overview .....	3
2. EXISTING METAL OXIDE PHOTOCONDUCTION MODELS.....	5
2.1 Surface Photovoltage .....	5
2.2 Oxygen Adsorption Kinetics.....	7
2.3 Oxygen Photodesorption Kinetics .....	11
2.4 Photoconduction .....	15
2.5 Carrier Lifetime Models .....	17
2.6 Conclusions.....	18
3. METAL OXIDE PHOTOCONDUCTION MODEL.....	20
3.1 Introduction.....	20
3.2 Planar Adsorption .....	20
3.3 Steady-State .....	25

3.4 Illumination Kinetics .....	27
3.5 Completely Depleted Device .....	35
3.6 Completely Depleted Illumination Kinetics.....	40
3.7 Nanowires .....	41
3.8 Quantum Dots .....	48
3.9 Junctions .....	51
3.9.1 Homojunction .....	51
3.9.2 Heterojunction.....	55
3.10 Multiple Traps.....	58
3.10.1 Multiple Acceptor Type Traps.....	58
3.10.2 Donor Type Traps .....	60
3.10.3 Humidity .....	62
3.11 Photocurrent.....	68
3.11.1 General Case .....	68
3.11.2 Back Gate Capacitance .....	70
4. PERFORMANCE METRICS AND DESIGN CONSIDERATIONS .....	72
4.1 Resistive and Photoconductive Gain.....	81
4.2 Response Time, Bandwidth, and Optical Bode Plots .....	92
4.3 Minimum Detectable Power .....	97
4.4 Device Design for Bacterial Fluorescence.....	102
5. PARAMETER EXTRACTION AND FITTING.....	109

5.1 Adsorption Rate Constant Measurement .....	109
5.1.1 Kelvin Probe Force Microscopy Measurement Method .....	109
5.1.2 Current Measurement Method .....	110
6. DEVICES.....	111
6.1 ZnO Thin Film on Thermal Oxide.....	111
6.1.1 Backgate Control of Adsorption Rate.....	113
6.1.2 Measurement Injection and Ejection Current .....	115
7. SIMULATIONS .....	118
7.1 Sentaurus Simulations.....	118
7.1.1 Partially Depleted Case.....	123
7.1.2 Injection and Ejection Current .....	127
7.1.3 Completely Depleted Case.....	129
8. CONCLUSIONS.....	133
REFERENCES .....	136
APPENDIX A SUPPLEMENTAL FILES .....	142
A.1 Permissions for Figure 3 .....	142
A.2 Permissions for Figure 5 .....	142
A.3 Permissions for Figure 32 (c).....	142

## LIST OF TABLES

Table 1: Material parameters for adsorption calculations shown in Figure 9.....	23
Table 2: Material parameters for calculations in Figure 8.....	32
Table 3: Parameters for CD device calculations in Figure 16.....	39
Table 4: Material parameters used to calculate photodesorption transient in Figure 17.....	41
Table 5: Adsorption parameters for simultaneous oxygen and water adsorption shown in Figure 31. P <sub>Th</sub> is the physically adsorbed water concentration under high humidity, and P <sub>Tl</sub> is the physically adsorbed water concentration under low humidity.....	63
Table 6: Device parameters for current calculations of simultaneous oxygen and water adsorption shown in Figure 31.....	63
Table 7: Adsorption rate parameters for simultaneous oxygen and water adsorption with dissociated water molecules shown in Figure 32(b). The physically adsorbed donor-type water concentration, N <sub>T,H<sub>2</sub>O</sub> , is equal to the physically adsorbed donor-type water concentration, P <sub>Th</sub> or P <sub>Tl</sub> .....	66
Table 8: Photocurrent calculation parameters for Figure 34.....	69
Table 9: Photoconductor and OPA627 Op-amp parameters [72] for calculations in Table 9.....	78
Table 10: Device parameters for calculation in Figure 42. The value q <sub>c,d</sub> is the adsorbed concentration in the dark.....	82
Table 11: Device parameters for Figure 44. The adsorbed concentration in the dark is the adsorbed concentration after 1 second for an initial concentration of 0. The device width is the depletion width corresponding to the adsorbed concentration in the dark.....	85
Table 12: Device parameters for Figure 45. The adsorbed concentration in the dark is the adsorbed concentration after 1 second for an initial concentration of 0. The device width is the depletion width corresponding to the adsorbed concentration in the dark.....	86
Table 13: Material parameters for calculations in Figure 47.....	88
Table 14: Parameters for calculations in Figure 48. The adsorbed concentration in the dark, q <sub>c,d</sub> is set to ensure both devices are in CD.....	89
Table 15: Parameters for calculations in Figure 53.....	95
Table 16: Parameters for CD device shown in Figure 54.....	96
Table 17: Parameters for Figure 55.....	98
Table 18: Parameters for CD devices in Figure 54.....	99
Table 19: Parameters for Figure 58.....	101

Table 20: Parameters for Figure 61.....	102
Table 21: Parameters for Figure 62.....	103
Table 22: Parameters for Figure 63.....	104
Table 23: Parameters for Figure 66. Backgate voltage is pulsed only applied when the illumination is off.....	107
Table 24: Bulk Material Parameters for Metal-Oxide Semiconductor material in Sentaurus. $N_c$ and $N_v$ are calculated from the density-of-states effective mass values from the equation given by [68] and the effective mass values $m_n^* = 0.29$ , $m_p^* = 1.21$ given by [51]. .....	119
Table 25: Interface material parameters for Metal-Oxide Semiconductor in Sentaurus.....	120
Table 26: Device parameters and simulation settings for partially depleted simulation. ....	124
Table 27: Measured and calculated steady-state illumination values at $t = 40\mu s$ for the simulation parameters shown in Table 26. ....	126
Table 28: Settings for simulating injection current. The rise time refers to the rise time of the illumination pulse.....	127
Table 29: Settings for completely depleted devices.....	130

## LIST OF FIGURES

Figure 1: Comparison of device performance for various UV photodetectors [10]–[22]. The target for species differentiation with fluorescence detection is shown by the star.....	3
Figure 2: Energy band diagram for semiconductor with an oxide on the surface (right) and negative trapped charge at the oxide-semiconductor interface or the oxide surface. A donor-type surface trap is represented by $E_{TD}$ , and an acceptor-type trap is represented by $E_{TA}$ . Adapted from [23]. . . . .	6
Figure 3: Energy band diagram for an n-type metal oxide surface. Reprinted with permission from A. H. Peterson and S. M. Sawyer, “Oxygen adsorption and photoconduction models for metal oxide semiconductors: a review,” <i>IEEE Sens. J.</i> , vol. 21, no. 15, pp. 16409–16427, Aug. 2021, Copyright 2021 IEEE, [23]. . . . .	7
Figure 4: Energy band diagrams for illuminated metal oxide surface. (a) Surface recombination: photogenerated carriers are separated by the surface potential, (b) Surface excitation: trapped electrons absorb photons and are excited to the conduction band. . . . .	11
Figure 5: Experimental results of porous ZnO sample with different illumination histories. Reprinted with permission from D. A. Melnick, “Zinc oxide photoconduction, an oxygen adsorption process,” <i>J. Chem. Phys.</i> , vol. 26, no. 5, pp. 1136–1146, May 1957, Copyright 1957 AIP, [8]. . . . .	14
Figure 6: Metal oxide quantum dots (blue) with oxygen adsorbates (white) creating spherical depletion widths represented by dashed lines. These depletion widths create barriers in the direction of current flow. A qualitative energy band diagram is shown as well. . . . .	16
Figure 7: (a) Sample with porous geometry and edge of the depletion region indicated by dashed lines. Current flows across necks; (b) Energy band diagram of neck cross-section; solid lines indicate a partially depleted neck, and dashed lines depict the energy band diagram after complete depletion. Current flows into the page. . . . .	16
Figure 8: Adsorption rate equation solution for $q_{c0} = 0$ , $b = 1$ . Solid black line is solution for (22) using MATLAB’s built-in solver ode15s, and dotted blue line is exact solution using the dimensionless form of (21). . . . .	22
Figure 9: (a) Adsorption transient calculated with (21) with material parameters shown in Table 1; (b) the same transient from (a) compared to Elovich Kinetics at Taylor Series expansion points $q_{c0} = 1 \times 10^{11}$ , $3 \times 10^{11}$ , and $7 \times 10^{11} \text{ cm}^{-2}$ . . . . .	23
Figure 10: (a) Multiplying factor between Elovich kinetics rate and exact rate as given by (24) for $n_b = 1 \times 10^{17} \text{ cm}^{-3}$ ; (b) Percent error between exact adsorbed concentration and that calculated by Elovich kinetics for $q_{c0} = 1 \times 10^{11} \text{ cm}^{-2}$ in Figure 9 (b). . . . .	25
Figure 11: Metal-oxide photoconduction process: (a) Illumination creates electron-hole pair in a system with initial adsorption rate $R_{ads,0}$ , depletion width $W_{D,0}$ , and adsorbed concentration $q_{c,0}$ ; (b) hole recombines with trapped electron bound by oxygen on the surface, changing the depletion width to $W_{D,L}$ and the adsorption rate to $R_{ads,L}$ ; photogenerated electron resides in the neutral region of the bulk; (c) Illuminated steady-state is reached for $R_{ads,SS} = R_{des}$ ; (d) after illumination is removed, electrons are recaptured by oxygen. . . . .	28

Figure 12: Photodesorption transients for material with parameters in Table 1 and Table 2 using (29)....	33
Figure 13: (a) Photodesorption transient from Figure 12 with $I_{opt} = 2\text{mW}$ and Elovich kinetics transients. The value of the steady-state concentration is $q_{c,ss} = 5.986 \times 10^{11}\text{cm}^{-2}$ and the initial value is $q_{c0} = 7 \times 10^{11}\text{cm}^{-2}$ ; (b) Error between (29) and (31) normalized to the range of the transient.....	34
Figure 14: Completely depleted semiconductor with adsorbed molecules on the surface forming depletion region. ....	36
Figure 15: Diagram of electric field and voltage in the completely depleted case. The red and blue lines (Voltage and Electric field respectively) are shown extended through the oxide to demonstrate what they would be in the partially depleted case. This is meant only as a visual tool to show how $\mathcal{E}_{ox}$ and $W_D - W$ are defined in this system. The actual voltage and electric field in the oxide are shown by the black lines labelled $V_{ox}(x)$ and $\mathcal{E}_{ox}$ .....	36
Figure 16: Adsorption transients for material parameters give in Table 1 and Table 3, different oxide thicknesses, and (a) backgate voltage of $V_{BG} = 0\text{V}$ and (b) $V_{BG} = 5\text{V}$ .....	40
Figure 17: Photodesorption transients for material with parameters given in Table 1, Table 3, and Table 4. ....	41
Figure 18: Nanowire with adsorbed molecules (white) and corresponding depletion region. Current moves parallel to surface and is modulated by depletion region. ....	42
Figure 19: Nanowire electrostatics model, (a) orthogonal view, and (b) top view.....	42
Figure 20: Adsorption transients for material parameters given in Table 1 and various diameters.....	45
Figure 21: Nanowire cross-section with infinitesimally thin rectangle centered on $x = x_0$ and with width $\Delta t$ .....	46
Figure 22: Quantum electrostatics model and Gaussian surface (dashed blue line).....	48
Figure 23: Adsorption transients for quantum dots with different radii and material parameters given in Table 1. ....	50
Figure 24: Homojunction device with two different carrier concentrations. ....	51
Figure 25: (a) Adsorption transients, (b) depletion width transients, and (c) rate of adsorption over time for homojunctions with the material parameters listed in Table 1 and $W_2 = 50\text{nm}$ .....	54
Figure 26: (a) Adsorption transients, (b) depletion width transients, and (c) rate of adsorption over time for homojunctions with the material parameters listed in Table 1.....	55
Figure 27: Example ZnO-Si heterojunction.....	56
Figure 28: Adsorption transients for homojunction with $N_{d1} = N_{d2} = 1 \times 10^{17}\text{cm}^{-3}$ , $W_2 = 50\text{nm}$ , $\epsilon_{r,1} = 11.9$ , $\epsilon_{r,2} = 8.4$ , and junction with $n_b = 1 \times 10^{17}\text{cm}^{-3}$ , $\epsilon_{r,2} = 11.9$ .....	57

Figure 29: Adsorption transients for multiple traps with $n_b = 1 \times 10^{17} \text{cm}^{-3}$ , $N_{t1} = N_{t2} = 1 \times 10^{15} \text{cm}^{-2}$ , $q_{c1}(0) = 0$ , $q_{c2}(0) = 0$ .....	60
Figure 30: Energy band diagram for an n-type metal oxide with a shallow-hole acceptor trap and a trapped hole.....	60
Figure 31: Current for device with parameters given by Table 6 under different humidity conditions. Current is calculated using (65). For dry oxygen, only (56) is used. For high humidity, both equation (56) and (57) are solved simultaneously with $P_T = P_{Th}$ . For low humidity, $P_T = P_{T1}$ .....	63
Figure 32: Photocurrent under different humidity conditions. For (a) and (b), photocurrent for dry O2 is calculated using (56), Table 6, and oxygen adsorption rate parameters in Table 7. For all transients in (a) and (b), $\lambda = 340\text{nm}$ and $I_{opt} = 60\text{mW}/\text{cm}^2$ . (a) Photocurrent for low and high humidity calculated using (60), (61), Table 6, and Table 7. (b) Photocurrent for low and high humidity calculated using (62), (63), Table 6, and Table 7. (c) Experimental measurements of ZnO nanowire photocurrent transients under different relative humidity conditions. Reprinted with permission from Y. Li, F. Della Valle, M. Simonnet, I. Yamada, and J.-J. Delaunay, "Competitive surface effects of oxygen and water on UV photoresponse of ZnO nanowires," <i>Appl. Phys. Lett.</i> , vol. 94, no. 2, Jan. 2009, Art. no. 023110, Copyright 2009 AIP, [69].	67
Figure 33: Geometry of sample analyzed in this section. Not shown is the depth 'd' into the page. 'S' is source contact, 'D' is drain contact. ....	68
Figure 34: Photocurrent transients for different illumination intensities using the device parameters given by Table 8.....	69
Figure 35: Photoconductor diagram.....	72
Figure 36: TIA circuit. ....	74
Figure 37: Voltage divider circuit for photodetector. ....	76
Figure 38: SNR for parameters shown in Table 9.....	78
Figure 39: (a) SNR for TIA with ideal op-amp compared to voltage divider (VD); (b) SNR for TIA with op-amp parameters given in Table 9 compared to VD. ....	79
Figure 40: (a) SNR as a function of $V_s$ for $R_{phl} = 100\Omega$ , $R_{phd} = 1\text{k}\Omega$ , $V_{cc} = 20\text{V}$ , and $B_0 = 16\text{MHz}$ , $v_{n,BB} = 5\text{nV}/\text{Hz}$ , $v_{n,f} = 50\text{nV}/\text{Hz}$ , $i_{BB} = 1.6\text{fA}/\text{Hz}$ at $f_0 = 1\text{Hz}$ , $I_Q = 7\text{mA}$ (b) SNR as a function of $V_{cc}$ for $R_{phl} = 100\Omega$ , $R_{phd} = 1\text{k}\Omega$ , $V_s = 10\text{V}$ , and $B_0 = 16\text{MHz}$ , $v_{n,BB} = 5\text{nV}/\text{Hz}$ , $v_{n,f} = 50\text{nV}/\text{Hz}$ , $i_{BB} = 1.6\text{fA}/\text{Hz}$ at $f_0 = 1\text{Hz}$ , $I_Q = 7\text{mA}$ .....	80
Figure 41: SNR for voltage divider with 1mW of power consumption and $B = 1\text{GHz}$ . ....	81
Figure 42: Resistive gain and dark resistance as a function of device width for a device with parameters given by Table 1 and Table 10. ....	83
Figure 43: Gain and dark current for device with width $W = 68.6\text{nm}$ and parameters given by Table 1 and Table 10.....	84

Figure 44: (a) Gain relative to the reference gain at $n_b = 1 \times 10^{14} \text{cm}^{-3}$ ; (b) Depletion width relative to the reference depletion width for $n_b = 1 \times 10^{14} \text{cm}^{-3}$ , fit is calculated with (81); Both plots calculated using parameters in Table 11. ....	85
Figure 45: Gain as a function of carrier concentration for CD case with parameters given by Table 12 and $t_{ox} = 100 \text{nm}$ . ....	86
Figure 46: (a) Gain as a function of dielectric permittivity; (b) Gain as a function of the adsorption constant. ....	87
Figure 47: Gain as a function of nanowire radius for parameters shown in Table 13. ....	88
Figure 48: Ratio of nanowire gain to planar gain as a function of planar device depth.....	89
Figure 49: Experimental measurements of ZnO thin film resistive gain as a function of thickness, (a) deposited by magnetron sputtering [85], and (b) deposited by sol-gel method [86]. ....	90
Figure 50: Intensity normalized gain as a function of nanowire diameter for various ZnO nanowires created with different fabrication processes [9], [69], [87], [88]. ....	91
Figure 51: Intensity normalized gain as a function of recovery time for various ZnO photoconductor devices [9], [11], [13], [41], [43], [50], [69], [85]–[91]. ....	92
Figure 52: Photocurrent and response time definitions.....	93
Figure 53: Performance metrics as a function of optical frequency for parameters in Table 1 and Table 15. (a) Resistive gain, (b) dark resistance, (c) SNR and average power consumption for voltage divider circuit, voltage measured across biasing resistor and using a bandwidth of 1MHz (d) photovoltage and voltage responsivity for the voltage divider circuit. ....	95
Figure 54: Performance metrics as a function of optical frequency for parameters in Table 1 and Table 16. (a) Resistive gain, (b) dark resistance, (c) SNR and average power consumption for voltage divider circuit, voltage measured across biasing resistor with a bandwidth of 1MHz, and (d) photovoltage and voltage responsivity for the voltage divider circuit. ....	97
Figure 55: Minimum detectable optical intensity for parameters given in Table 17. ....	98
Figure 56: Minimum detectable optical power for different adsorption rate constants. Parameters are given in Table 17 and $n_b = 1 \times 10^{17} \text{cm}^{-3}$ . ....	99
Figure 57: Minimum detectable optical intensity for completely depleted device (Table 18) and partially depleted device (Table 17) and $n_b = 1 \times 10^{17} \text{cm}^{-3}$ . ....	100
Figure 58: Minimum detectable optical power over time for nanowires with parameters given in Table 19. ....	101
Figure 59: Comparison of minimum detectable optical intensity for nanowire with $r = 100 \text{nm}$ and parameters in Table 19 and PD planar device with parameters in Table 17 and $n_b = 1 \times 10^{17} \text{cm}^{-3}$ . ....	101
Figure 60: Effect of partial absorption according to (45) on minimum detectable optical intensity. Parameters are given in Table 19 and $r = 100 \text{nm}$ . ....	102

Figure 61: Minimum detectable optical intensity for CD device with backgate bias of 1V and parameters given by Table 1 and Table 20. ....	103
Figure 62: Minimum detectable intensity for a pulsed backgate. Parameters are from Table 1 and Table 21. ....	104
Figure 63: Pulsed mode CD device for the parameters shown in Table 1 and Table 22. ....	105
Figure 64: CD nanowire cross-section schematic. ....	105
Figure 65: Capacitive mode circuit. The dark blue sections indicate the contacts. ....	107
Figure 66: Photoresponse of a capacitive mode circuit. Parameters given by Table 1 and Table 23. ....	108
Figure 67: Capacitive mode device in a TIA circuit. ....	108
Figure 68: CD ZnO UV photodetector device. ....	111
Figure 69: SEM image of ZnO thin film. Columns are ~20nm in width. ....	112
Figure 70: High magnification of ZnO thin film. Columns appear to have roughly hexagonal geometry. ....	113
Figure 71: Experimental setup for adsorption rate control via backgate bias. ....	114
Figure 72: Photocurrent for different backgate biases. For $V_{bg} = 0V$ , the backgate bias is turned on at $t = 4.17s$ and turned off at $t = 50.13s$ ; for $V_{bg} = 16V$ , 1 (grey) the backgate bias is turned on at $t = 5.84s$ and turned off at $V_{bg} = 41.53s$ ; for $V_{bg} = 16V$ , 2 (yellow) the backgate bias is turned on at $t = 4.21s$ and turned off at $t = 57.83s$ . ....	115
Figure 73: Experimental setup for measuring backgate current. ....	116
Figure 74: (a) Ejection back gate current under illumination with a biasing resistor of $300k\Omega$ . The light is turned on at $t=0s$ ; (b) Injection backgate current after illumination is removed. The light is turned off at $t=0s$ . ....	117
Figure 75: (a) Ejection back gate current under illumination with a biasing resistor of $1k\Omega$ . The light is turned on at $t=0s$ ; (b) Injection backgate current after illumination is removed. The light is turned off at $t=0s$ . ....	117
Figure 76: Example metal oxide photoconductor structure with metal oxide width $W=50nm$ , oxide thickness $t_{ox}=1\mu m$ , device length $l=1\mu m$ , and illumination at the surface of the device. ....	122
Figure 77: Adsorption kinetics for $k_n = 1 \times 10^{-14}cm^3/s$ simulated in Matlab and Sentaurus. ....	123
Figure 78: Adsorption kinetics for $k_n = 1 \times 10^{-10}cm^3/s$ simulated in Matlab and Sentaurus. ....	123
Figure 79: Current measured from MATLAB and Sentaurus. ....	125
Figure 80: (top) Band diagram for device prior to illumination and (bottom) at steady-state adsorption during illumination. Oxide/metal oxide interface at $x=0$ and metal oxide surface at $0.5\mu m$ . .	126

Figure 81: Electron distribution near the surface of the device. Oxide/Metal oxide interface at $x=0$ , and air/metal oxide interface at $x = 5 \times 10^{-5}$ cm. ....	127
Figure 82: Ejection and Injection current for settings in Set 1 of Table 28. ....	128
Figure 83: Ejection and Injection current for the settings in Set 2 of Table 28. ....	129
Figure 84: Simulated and calculated drain current for metal oxide width of 25nm, oxide thickness 10nm, applied bias 1mV, and intensity of illumination of 10W/cm <sup>2</sup> . The rise and fall time of the illumination pulse is 1ns. ....	130
Figure 85: Simulated and calculated source current for metal oxide width of 25nm, oxide thickness 10nm, applied bias 1mV, and intensity of illumination of 10W/cm <sup>2</sup> . The rise and fall time of the illumination pulse is 1ns. ....	131
Figure 86: Simulated and calculated current for parameter Set 2 in Table 29. ....	132

## ACKNOWLEDGEMENTS

Thank you to everyone who made this work possible. First, thank you to Professor Sawyer for taking in a lost graduate student and giving me the time and space to find my way. Thank you to the amazing Sawyer research group: Lauren Brady, Dylan Reese, Prachi Sharma, Dali Shao, Anindita Ghosh, and James Davis. You have all been so supportive both academically and emotionally. Special thanks to Anindita Ghosh for her help with my experimental work. Thank you to the MNCR staff: John Barthel, Bryant Crowell, Sarah An, David Frey, and Kent Way. Thanks for your patience with me and teaching me so much. Thanks to my committee, Paul Chow, Michael Shur, and Joel Plawsky for all of your valuable feedback and guidance. Special thanks to Paul Chow, who first sparked my interest in semiconductor physics. Thanks to my family for helping me to chase my dream of changing the world with science. Special thanks to my brother, Sean Peterson, for checking in on me constantly. Thanks to my cat, Luna, who helped me get up every morning and stayed up with me when I couldn't sleep. Thanks to all my friends who helped me forget about all this for a while. And of course, thanks to James Davis, the love of my life. You are the reason I got through this.

# DEDICATION

*For everyone and everything*

*I lost along the way*

# ABSTRACT

There is a need for real-time biohazard detection in hospitals, water-treatment facilities, bodies of water, and food processing facilities to prevent bacterial infections and outbreaks. Detection of small concentrations of bacteria requires photodetectors with a large photoresponsivity and fast response time. Metal oxide Ultraviolet (UV) photodetectors are a good candidate for this application due to their large photoresponsivity compared to other material systems. However, metal oxide photodetectors generally have a response time that is too slow for bacterial detection, and it is difficult to predict device performance because the oxygen adsorption and photodesorption processes which control the UV response are not well understood.

To aid in the development of metal oxide photodetectors for bacterial fluorescence detection, this thesis presents a new model for metal oxide photodetectors. This is accomplished by deriving and solving the oxygen adsorption and photodesorption rate equations which control the UV response of these devices. This interaction with oxygen molecules is modelled by a variation in the space charge width at surfaces, grain boundaries, and necks which in turn provides the surface concentration of electrons available for adsorption of oxygen. The model provides the transient photocurrent given the device geometry, material parameters, atmospheric environment, and illumination intensity and wavelength. From the transient photocurrent, figures of merit such as the photoresponsivity, current on-to-off ratio, response time, and signal-to-noise (SNR) ratio are derived. The model is integrated into a Graphical User Interface (GUI) in MATLAB to allow for fast design of metal oxide photodetectors. This model enables a comparison of the performance of metal oxide photodetectors based on material, geometry, morphology, doping, and atmospheric environment.

This new model sheds light on the operation of metal oxide devices, and it also points to the types of devices that will enable remote bacterial fluorescence detection. Based on this model, a novel photodetector structure, called a Capacitive Mode photodetector, is proposed. This type of device enables ultra-fast response time for very low illumination intensities. A prototype of this device is fabricated and

characterized. A ZnO thin film on Silicon thermal oxide with a p<sup>+</sup>-Si backgate is created. We demonstrate the ability to control the oxygen adsorption rate with the backgate, thereby reducing the recovery time and enabling detection of very low optical powers. The device is also operated in a novel mode, called Capacitive Mode, which decreases the response time from minutes to milliseconds at low optical powers. This work opens the door for real time biological detection. Significant future work is still required in the form of characterizing some material parameters and implementing novel photodetector device designs.

# 1. INTRODUCTION

## 1.1 Bacterial Fluorescence Detection

Contamination of medical equipment in hospitals is estimated to result in over 90,000 deaths per year and cost hospitals \$28 billion to \$45 billion in the U.S. alone [1], [2]. Studies of previous breakouts of Methicillin-resistant Staphylococcus (MRSA) and Clostridium difficile in a hospital were traced back to contamination of a blood pressure cuff [3], [4]. Prevention of these infections would require frequent monitoring of all medical equipment and surfaces. Common methods such as polymerase chain reaction (PCR) which require samples to be taken is not a viable option for monitoring large areas and surfaces. One way of monitoring bacterial growth is by detecting the light emitted from fluorophores present in bacteria. For example, the fluorophore tryptophan has an emission peak at 340nm and an excitation wavelength at 280nm [5]. Thus, bacterial concentration can be determined by sensing the ultraviolet light emitted by tryptophan. Such a system based on this would require a UV photodetector with a high photoresponsivity, high on-current to off-current ratio, and high UV to visible rejection ratio, and the system would need to detect bacterial concentrations as low as 10 colony-forming units (cfu)/mL ideally at a distance of a few meters [6]. Sharma demonstrated that a commercial Si photodetector with a responsivity of 0.13A/W was able to detect only  $7.81 \times 10^5$  cfu/mL of E. coli at a distance of 1 meter [7]. Sharma further estimates that a sample of E. coli with a concentration of  $10^2$  cfu/mL would emit a fluorescent signal on the order of nW/cm<sup>2</sup> or less at a distance of 3 meters. For a photodiode to detect such a signal it would need to have a dark current of less than 1nA, a photoresponsivity greater than  $10^3$  A/W, and a response time less than 1ms. For the photodiode to also differentiate between bacterial species, the response time needs to be on the order of 1ns. Currently, commercial GaN, SiC, AlGaN, GaP, and Si UV photodetectors do not meet the requirements for such a system as they have low responsivities on the order of 0.2A/W near 340nm [7].

## 1.2 Metal Oxide UV Photodetectors

Metal oxide UV photodetectors have a large photoresponsivity and on-current to off-current ratio compared to photodetectors based on other material systems, and they also have a high UV-to-visible rejection ratio (UVVRR). This makes them a good candidate for remote bacterial fluorescence detection. The photoresponsivity and on-current to off-current ratio has been attributed to the adsorption and desorption of oxygen molecules on the metal oxide surface [8], [9]. Oxygen molecules trap free electrons at the surface of metal oxides, creating a space charge region (SCR) at the surface. Under illumination, the SCR separates electrons and holes and the photogenerated holes recombine with the trapped electrons at the surface thereby reducing the size of the SCR. The change in the width of the space-charge region under illumination is determined by the initial rate of electrons to the surface in the dark and the rate of holes to the surface induced by illumination, and steady-state is achieved when the rate of electrons equals the rate of holes to the surface. As will be discussed in this thesis, this photo-detection method can result in large photoconductive gains and enable relatively low levels of luminous flux to be detected compared to other material systems.

## UV Photodetector Performance Comparison

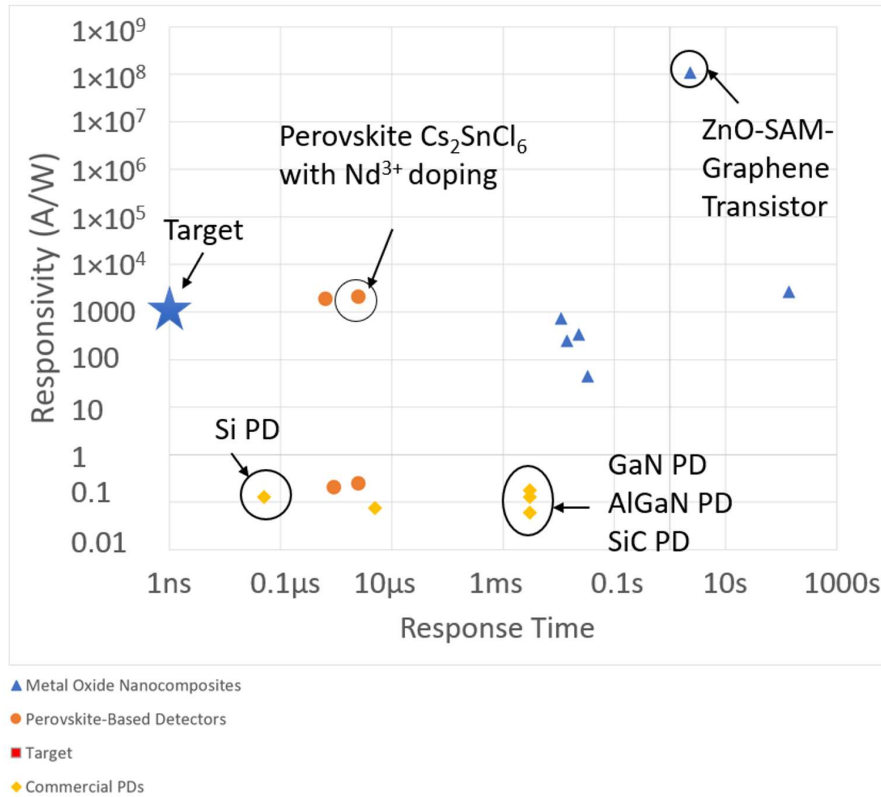


**Figure 1: Comparison of device performance for various UV photodetectors [10]–[22]. The target for species differentiation with fluorescence detection is shown by the star.**

The drawback to metal oxide photodetectors is their slow response time. As shown in Figure 1, metal oxide based photodetectors tend to have higher responsivity and higher response times compared to commercial photodiode devices. This slow response time is attributed to adsorption process which is self-limiting in nature.

### 1.3 Thesis Overview

Because the adsorption process controls the photoresponse of metal oxide photodetectors, a model describing this process would be advantageous in interpreting photodetector measurements and designing photodetectors because it could yield critical insights, allow scientists to model designs before fabrication, and direct research to important areas. Previous work has been done to describe the general oxygen adsorption and photodesorption process. However, there is not yet a photoconduction model for

metal oxide UV photodetectors which predicts important figures of merit such as response time and photoresponsivity and accounts for device structure and morphology. Thus, in this thesis, a new metal oxide photoconduction model is developed. This model provides a new interpretation for the behavior of photogenerated carriers in the SCR, allows closed-form expressions to be derived for photoresponsivity, on-current to off-current ratio, and response time, and explains the dependence of device geometry, morphology, and material parameters on performance.

Chapter 2 discusses existing work on metal oxide adsorption and photoconduction models. Issues and shortcomings within the models are discussed, and the requirements for a new model are outlined. Chapter 3 covers the new model. The exact solutions to the adsorption and photodesorption rate equations on a partially and a completely depleted planar surface are derived. Then the rate equations are derived for nanowires, quantum dots, and junction devices. Finally, the photocurrent and performance metrics as a function of adsorbates are derived and discussed. Chapter 4 translates the adsorption equations from Chapter 3 into photodetector performance metrics. New photoconductor performance metrics are derived, and the optimal device designs for bacterial fluorescence detection are discussed. Chapter 5 proposes new parameter extraction methods for measuring the adsorption rate constant of metal oxide semiconductors. Chapter 6 discussed the development of a novel device called a Capacitive Mode photodetector. The control of the adsorption rate via a backgate electrode is demonstrated. Chapter 7 presents a solution of the adsorption rate equations through the program Sentauros. Chapter 8 concludes with a discussion of future work and the application of the model to other fields.

## 2. EXISTING METAL OXIDE PHOTOCONDUCTION MODELS

In this section, a review of the current adsorption and photoconduction models are presented. These models provide valuable insights and interpretations upon which the new model is built. Each section will highlight the important insights while explaining the limitations and shortcomings of the model. Not all published models are discussed here, so the models that are discussed have been chosen based on the frequency of their usage in other publications and their similarity to the new model. Additionally, a model for metal oxide gas sensors without illumination is discussed because it provides an insightful perspective on the surface chemistry occurring on metal oxides and is the starting point for the new photoconductive model. For a more in-depth review of these models, we refer to the reader to the author's complete review on them [23].

### 2.1 Surface Photovoltage

Brattain, Bardeen, and Garrett were among the first to examine gaseous adsorbates and defect-related traps on semiconductor surfaces [24]–[27]. They observed a surface potential which varied with illumination on the surface of semiconductors, and thus they called the phenomenon “surface photovoltage” (SPV). Germanium was primarily used in these studies. The surface of Germanium develops a native oxide in air, and therefore has an energy band diagram as shown in Figure 2. In the energy band diagram, trapped charges are present at both the oxide surface and the oxide-semiconductor interface. This produces both a potential drop across the oxide,  $V_D$ , and a surface potential at the semiconductor surface,  $V_S$ . The charge at the semiconductor-oxide interface is created by carriers trapped at defect sites and interface states, whereas the charge on the oxide surface is primarily created by adsorbed gas molecules. Brattain determined that under illumination, photo-generated carriers recombine with these trapped charges and thus change the surface potential.

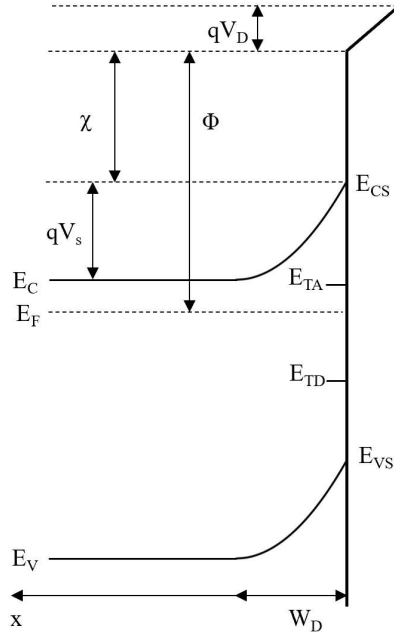


**Figure 2: Energy band diagram for semiconductor with an oxide on the surface (right) and negative trapped charge at the oxide-semiconductor interface or the oxide surface. A donor-type surface trap is represented by  $E_{TD}$ , and an acceptor-type trap is represented by  $E_{TA}$ . Adapted from [23].**

Metal oxides have a different surface structure to Germanium. They do not have a native oxide in ambient conditions. Instead, oxygen acts as an adsorbate directly on the surface of the metal oxide. This results in a system with the energy band diagram shown in Figure 3. Oxygen molecules act as acceptor-type traps with trap energy  $E_T$ . Thus, oxygen adsorption causes a build-up of negative charge on the surface and creates a surface potential and depletion region with width  $W_D$ . This surface potential reduces the concentration of electrons at the surface, and therefore adsorption is a self-limiting process.

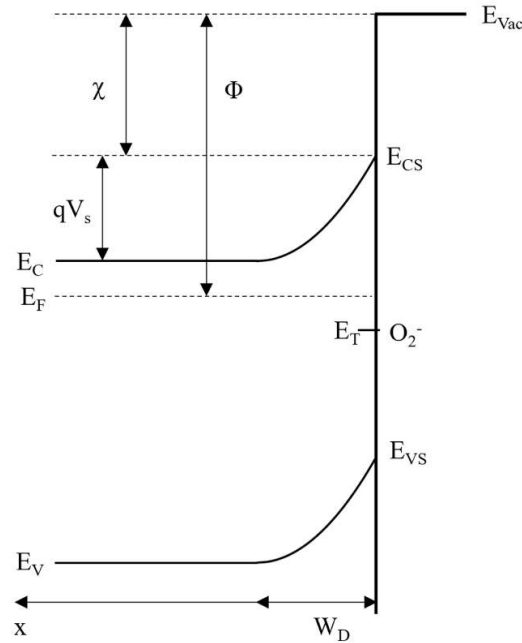


**Figure 3: Energy band diagram for an n-type metal oxide surface. A. H. Peterson and S. M. Sawyer, “Oxygen adsorption and photoconduction models for metal oxide semiconductors: a review,” *IEEE Sens. J.*, vol. 21, no. 15, pp. 16409–16427, Aug. 2021, Copyright 2021 IEEE, [23].**

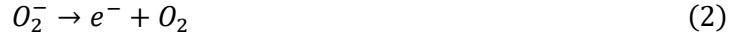
To mathematically derive the magnitude of the surface potential and depletion width, the concentration of trapped electrons must be known. In general, trap occupation at thermal equilibrium can be mathematically described via Fermi-Dirac statistics. However, oxygen adsorption on metal oxides has been experimentally shown to last for hours or days [8], [28]–[30]; thermal equilibrium of the oxygen adsorption process is not a reasonable assumption for most metal oxide systems. Therefore, a transient analysis of trap occupation will provide a more accurate description of metal oxide systems.

## 2.2 Oxygen Adsorption Kinetics

In the Adsorption Kinetics model, the transient evolution of oxygen trap occupation can be mathematically described by the concentrations of oxygen and electrons at the surface and the probability of the oxygen to interact with these carriers. Morrison describes the adsorption kinetics of a molecule onto a metal oxide surface by first considering the chemical reactions which occur on the surface [31]. The adsorption chemical reaction on the surface at room temperature and atmospheric pressure can be described as:



Which is the primary reaction considered in most literature and represents a conduction band electron binding to an oxygen molecule. The emission of a trapped electron to the conduction band must also be considered:



Through mass action law, the chemical equations (1) and (2) can be written as a rate equation [31]:

$$\frac{dq_c}{dt} = k_n(n_s(N_T - q_c) - n_1q_c) \quad (3)$$

$$k_n = v_{th}\sigma \quad (4)$$

where  $q_c$  is the surface concentration of electrons trapped by the molecule (also referred to as the chemically adsorbed concentration),  $k_n$  is the rate constant (given by the product of the average thermal velocity of the electrons,  $v_{th}$ , and the capture cross-section of the trap,  $\sigma$ ),  $n_s$  is the density of electrons at the surface,  $N_T$  is the concentration of available adsorption sites (also referred to as the physically adsorbed concentration), and  $n_1$  represents the probability of thermal emission of a trapped electron to the conduction band. Thus Eqn. 3 describes the rate of adsorption by the probability of the capture of free surface electron by an available trap. Morrison writes the surface electron concentration in terms of the bulk electron concentration,  $n_b$ , through Boltzmann statistics:

$$n_s = n_b e^{\frac{qV_s}{kT}} \quad (5)$$

where  $q$  is the elementary charge,  $k$  is Boltzmann's constant, and  $T$  is temperature. Likewise, the emission constant is given by

$$n_1 = N_c e^{-\frac{E_{CS} - E_T}{kT}} \quad (6)$$

where  $E_{CS}$  is the conduction band energy at the surface, and  $E_T$  is the trap level as shown in Figure 3. Similarly, expressions for the rate of capture and emission of holes in the trap is given by:

$$\frac{dp_t}{dt} = k_p(p_s q_c - p_1 p_t) \quad (7)$$

$$p_s = p_b e^{\frac{qV_s}{kT}} \quad (8)$$

$$p_1 = N_V e^{\frac{E_T - E_{VS}}{kT}} \quad (9)$$

However, these equations are generally not considered since the hole concentrations in metal oxide semiconductors tend to be negligibly small.

The surface potential can be written in terms of the adsorbed concentration via the depletion approximation:

$$V_s = -\frac{qn_b W_D^2}{2\epsilon_s} \quad (10)$$

where  $W_D$  is the depletion width. The depletion width can be written in terms of the adsorbed concentration through charge neutrality, that is, the number of trapped electrons is equal to the number of exposed donors in the depletion width:

$$W_D = \frac{q_c}{n_b} \quad (11)$$

To simplify (7), Morrison assumes that the physically adsorbed concentration is much larger than the chemically adsorbed concentration and that thermal desorption is small compared to adsorption.

Combining (7), (10), and (11) and including these assumptions yields the adsorption rate equation:

$$\frac{dq_c}{dt} = k_n N_T n_b e^{-\frac{q^2 q_c^2}{2kT\epsilon_s n_b}} \quad (12)$$

To simplify the solution of (12), a truncated Taylor series expansion of the surface potential is often used [8], [29], [31]–[34]. The Taylor series expansion of  $V_s$  with respect to  $q_c$  about some concentration  $q_{c0}$  is:

$$V_s = V_{s0} - (q_c - q_{c0}) \frac{2qq_{c0}}{2n_b\epsilon_s} - (q_c - q_{c0})^2 \frac{q}{2n_b\epsilon_s} \quad (13)$$

where  $V_{s0}$  is the potential for  $q_c = q_{c0}$ , and  $q_{c0}$  can be arbitrarily chosen. Equation (13) is truncated to yield:

$$V_s \approx V_{s0} - (q_c - q_{c0}) \frac{2qq_{c0}}{2n_b\epsilon_s} \quad (14)$$

Substituting (14) into (12) yields the Elovich rate equation or Elovich kinetics equation:

$$\frac{dq_c}{dt} = k_n N_T n_b e^{\frac{q}{kT} (V_{s0} - (q_c - q_{c0}) \frac{2qq_{c0}}{2n_b\epsilon_s})} \quad (15)$$

This equation is usually simplified to the form:

$$\frac{dq_c}{dt} = a e^{-\beta q_c} \quad (16)$$

$$a = k_n N_T n_b e^{-\frac{qV_{s0}}{kT}} \quad (17)$$

$$\beta = \frac{q^2 q_{c0}}{kT n_b \epsilon_s} \quad (18)$$

Equation (16) has time domain solution:

$$q_c(t) = \frac{1}{\beta} \ln(e^{\beta q_c(0)} + \beta a t) \quad (19)$$

The rate equations presented in this section align well with many experimental measurements of metal oxide photoconductive decays. The adsorption rate equation predicts that at the onset of adsorption, oxygen will rapidly chemisorb on the surface. This will establish a potential barrier which will limit further adsorption of oxygen, and therefore the rate of adsorption will continually decrease. In

photoconductive decays, this presents as a rapid decrease in current followed by a slow decrease in current [9], [11], [28], [35]. Additionally, the rate equation shows a dependence of the adsorption rate on temperature and oxygen pressure through the term  $N_T$ . An increase in either temperature or oxygen pressure will increase the adsorption rate which is consistent with experimental measurements [8], [32], [36]–[38]. The Elovich kinetics have been successfully used to describe current transients in metal oxides, however because they are dependent on a Taylor series expansion, they are only valid for small changes in current.

### 2.3 Oxygen Photodesorption Kinetics

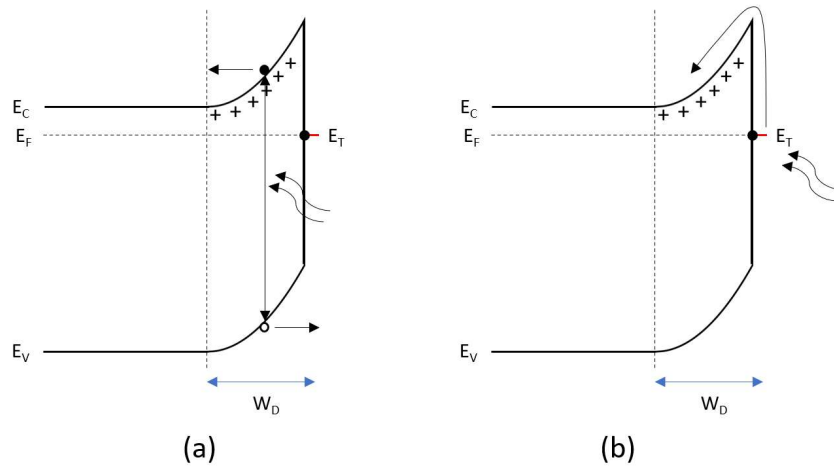


**Figure 4: Energy band diagrams for illuminated metal oxide surface. (a) Surface recombination: photogenerated carriers are separated by the surface potential, (b) Surface excitation: trapped electrons absorb photons and are excited to the conduction band.**

The photodesorption of oxygen molecules from the surface of metal oxides occurs by two possible processes: surface excitation and surface recombination. In surface recombination, a photogenerated electron-hole pair created in the depletion width or a diffusion length away from the depletion width will be separated by the electric field. Holes will move to the surface where they recombine with electrons trapped by oxygen. This process is represented by the chemical equation:



This process is shown in Figure 4(a). In surface excitation, the photons are absorbed by the trapped surface electrons and excited directly to the conduction band. This process is shown in Figure 4(b). When trapped electrons are removed from the surface by either process, the surface charge is reduced thereby reducing the magnitude of the surface potential and the depletion width.

Morrison describes bulk recombination as a change in the rate of holes to the surface [31].

Assuming that photogenerated holes are the dominant form of holes to the surface, (7) can be written as:

$$\frac{dp_t}{dt} = \gamma I_{opt} \quad (21)$$

where  $\gamma$  is a constant and  $I_{opt}$  is the illumination intensity. Illumination can also have the effect of increasing the bulk concentration of electrons which may lead to photoadsorption. Medved and Morrison model this effect by modifying (12) to include a photogenerated electron term:

$$\frac{dq_c}{dt} = k_n(n_b + \Delta n)N_T e^{\frac{qV_s}{kT}} \quad (22)$$

Medved incorporates (21) into (22) to create a photodesorption rate equation [32]:

$$\frac{dq_c}{dt} = k_n N_T (n_b + \Delta n_b) e^{\frac{qV_s}{kT}} - \gamma I_{opt} \quad (23)$$

For sufficiently small illumination  $\Delta n_b \ll n_b$ , and only photodesorption needs to be considered. In this case, oxygen molecules will continue to desorb until the rate of electrons and holes to the surface are equal. The equation then becomes:

$$\frac{dq_c}{dt} = k_n N_T n_b e^{\frac{qV_s}{kT}} - \gamma I_{opt} \quad (24)$$

The steady state potential is calculated by setting the adsorption rate equal to the desorption rate:

$$V_{s,ss} = \frac{kT}{q} \ln \left( \frac{\gamma I_{opt}}{k_n n_b N_T} \right) \quad (25)$$

Equation (25) is often written in terms of the SPV. The SPV is defined as the change in the surface potential from a reference surface potential:

$$SPV = V_s - V_{s,0} \quad (26)$$

where  $V_{s,0}$  is the reference potential, usually defined as the potential in the dark. Experimental measurements of the SPV versus illumination demonstrate a mathematical form given by:

$$SPV = \eta \frac{kT}{q} \ln(KI) \quad (27)$$

where  $\eta$  and  $K$  are fitting parameters. As will be shown later in this thesis,  $\eta$  represents a deviation from (25) and generally has value between 1 and 2 [39], [40].

The qualitative behavior of these photodesorption equations is consistent with experimental studies of photocurrent in metal oxides. Equation (24) predicts for  $\gamma I_{opt} \gg k_n N_T n_b \exp(qV_s/kT)$ , there will be a linear decrease in the adsorbed concentration over time until the system approaches steady-state. Additionally, under these conditions, an increase in  $I_{opt}$  will increase the rate of desorption. Both phenomena can be seen in phototransients of metal oxide photodetectors [41]–[44]. Note that the photocurrent is inversely proportional to the adsorbed concentration, as will be discussed in Section 3.11. Equation (24) indicates that there is a minimum detectable illumination intensity. For  $\gamma I_{opt} < k_n N_T n_b \exp(qV_s/kT)$ , the rate of holes will be less than the rate of electrons to the surface and adsorption will continue to occur. In literature about the SPV, this is called the “null-regime” [45], and can be seen in many experimental measurements [9], [46], [47].

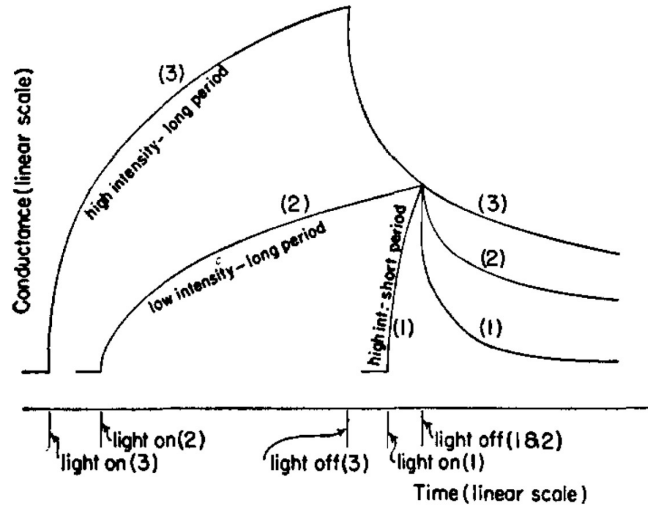


Figure 5: Experimental results of porous ZnO sample with different illumination histories. Reprinted with permission from D. A. Melnick, "Zinc oxide photoconduction, an oxygen adsorption process," *J. Chem. Phys.*, vol. 26, no. 5, pp. 1136–1146, May 1957, Copyright 1957 AIP, [8].

The photoresponse of porous metal oxides differ somewhat from these equations. One of the earliest models on photoconduction in metal oxide semiconductors was published by Melnick [8]. This work examines porous sintered ZnO samples and attempts to account for the nonlinear behavior observed in their photoconductance transients which cannot be describe by monomolecular, bimolecular, or higher order models. His experimental results are shown in Figure 5. These plots show the photoconduction of the ZnO samples under different illumination intensities and times, and they reveal that the photoconductance is a function of illumination intensity and duration. That is, the conduction decay transient is not a function of the conduction itself:

$$\frac{dG}{dt} \neq -f(G) \quad (28)$$

where G is the conductance. This is clearly seen in Figure 5 where three decay transients for the same sample with different prior illuminations all pass through the same point, but they have different transients for times after that point. The same is true of the rise transient shown in Figure 5. From these experiments he concludes that the observed photoconduction transient is a summation of multiple

independent local conductance values with different time constants. That is, due to the porous nature of the sample, there are multiple parallel surfaces which all adsorb oxygen. Under illumination, they each experience different illumination intensities and therefore different photodesorption rates and steady-states. Thus, this can be modeled as several independent Elovich kinetics transients in parallel.

The second form of photodesorption is surface excitation of trapped electrons. Here, trapped electrons at the surface are resonantly excited to the conduction band. The desorption rate then has the form [48]:

$$R^* = \sigma_{ph}^S q_c \Phi_{opt} \quad (29)$$

where  $\sigma_{ph}^S$  is the optical capture cross-section of electrons at the surface, and  $\Phi_{opt}$  is the light flux. This type of photodesorption also reduces the surface charge and therefore also reduces the surface potential and depletion width at the metal oxide surface.

## 2.4 Photoconduction

The current in metal oxide semiconductors is modulated by the width of the depletion region at the surface. As oxygen molecules adsorb and increase the width of the depletion region, the current decreases. Under illumination, oxygen molecules desorb, and the depletion width decreases the current increases resulting in a photocurrent. The current can be related to the adsorbed concentration through (11). In planar devices, the depletion width is directly proportional to the adsorbed concentration. For a rectangular sample with thickness  $W$ , conductivity  $\sigma$ , applied voltage  $V$ , length  $l$ , depth  $d$ , and depletion width  $W_D$  has current:

$$I = \frac{V\sigma d}{l} (W - W_D) \quad (30)$$

Equation 30 only describes the current based on depletion width changes. If photogenerated carriers are generated in the bulk away from the surface, then the bulk photocurrent must be incorporated into (30) as a change in the sample conductivity.

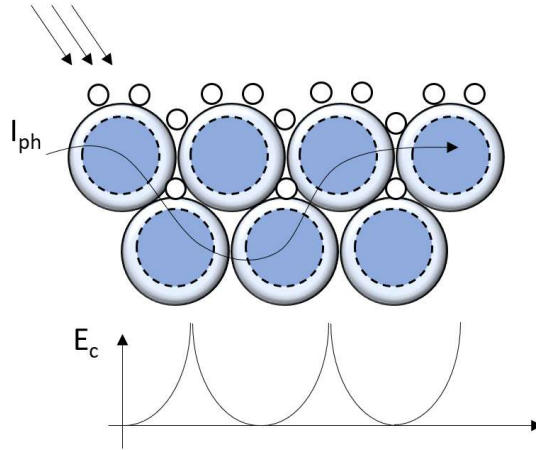


**Figure 6: Metal oxide quantum dots (blue) with oxygen adsorbates (white) creating spherical depletion widths represented by dashed lines. These depletion widths create barriers in the direction of current flow. A qualitative energy band diagram is shown as well.**

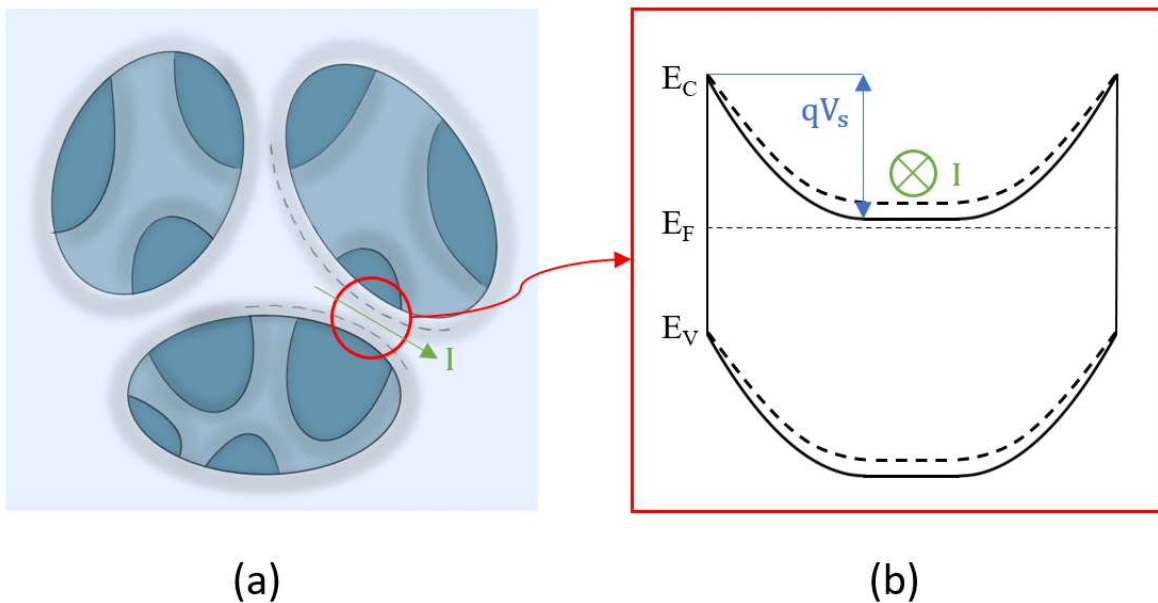


**Figure 7: (a) Sample with porous geometry and edge of the depletion region indicated by dashed lines. Current flows across necks; (b) Energy band diagram of neck cross-section; solid lines indicate a partially depleted neck, and dashed lines depict the energy band diagram after complete depletion. Current flows into the page.**

In the case of porous samples, nanostructured materials, or polycrystalline materials the depletion width may develop parallel to the flow of current. Such a scenario is shown in Figure 6 where potential barriers are developed between the interfaces of metal oxide quantum dots. In porous materials, the depletion width may also develop on multiple surfaces surrounding the current flow as depicted in Figure

7. In these cases, the current must be described using the equations for diffusion and thermionic emission over a barrier [49]. Depletion across necks or grains will present barriers to conduction. Depending on the size of the neck relative to the Debye length of the material, different equations should be used to calculate the current. In the case where the depletion width is on the order of or less than the Debye length, electrons travel across the barrier either by thermionic emission or diffusion. For diffusion, the conductance across the barrier can be written as:

$$G_{diff} = \frac{A^* q^2 \mu_n}{kT} \sqrt{\frac{2n_b |V_s|}{\epsilon_s}} \exp\left(-\frac{q|V_s|}{\eta^* kT}\right) \quad (31)$$

where  $A^*$  is the effective area, and  $\eta^*$  is the ideality factor of the barrier [49]. The conductance for a barrier dominated by thermionic emission can be written as [49]:

$$G_{TE} = \frac{A^* q^2 n_b v_{th}}{4kT} \exp\left(-\frac{q|V_s|}{kT}\right) \quad (32)$$

## 2.5 Carrier Lifetime Models

In addition to the physical models presented in the prior sections, several phenomenological models have been developed to model the metal oxide photoresponse. The most common of these is the bi-exponential model [9], [11], [35], [50]–[53]. This model assumes that the fast initial decay of the photocurrent in metal oxide devices is caused by bulk recombination with time constant  $\tau_1$  and that the slow decay is caused by adsorption with time constant  $\tau_2$ . It assumes that adsorption has an exponential decay and can therefore be characterized through a single time constant,  $\tau_2$ . The photocurrent is then written as:

$$I_{ph} = a_1 e^{-\frac{t}{\tau_1}} + a_2 e^{-\frac{t}{\tau_2}} \quad (33)$$

This model has been used to fit to individual photocurrent decay transients, but it is not successful at predicting any other transient but the one to which it is fit. The adsorption kinetics models demonstrate

that adsorption cannot be characterized by exponential functions, and therefore (33) is a poor model for metal oxide semiconductors whose photoresponse is dominated by adsorption.

## 2.6 Conclusions

The oxygen adsorption and photodesorption models outlined in Sections 2.1-2.4 are consistent with many experimental results. These models predict key qualitative features of the photocurrent transient: the linear rise in photocurrent under illumination and the rapid decay followed by slow decay of the photocurrent. They can also account for the effect of oxygen pressure and temperature, the presence of a minimum detectable illumination intensity below which the surface potential will not respond, and the effect of porous structures on the form of the photocurrent. Some performance metrics can be calculated from these equations. The steady-state photocurrent for a given illumination can be calculated from (25). The time domain form of the photocurrent decay can be approximately represented by the Elovich Kinetics, allowing for analysis of the response time.

However, these models have many limitations. The Elovich kinetics equations is only valid for a small change in  $q_c$ . As shown in [23], the Elovich kinetics rate of adsorption can be related to the actual rate of adsorption by:

$$\left. \frac{dq_{c,e}}{dt} \right|_{q_{c,e}=q_c} = \exp\left(\frac{q^2 \Delta q_{c,e}^2}{2kT\epsilon_s n_b}\right) \frac{dq_c}{dt} \quad (34)$$

$$\Delta q_{c,e} = q_c - q_{c0} \quad (35)$$

where  $q_{c,e}$  is the adsorbed concentration as calculated by Elovich kinetics in (12),  $q_c$  is the actual adsorbed concentration in (16), and  $\Delta q_{c,e}$  is the difference between the adsorbed concentration and the Taylor series expansion point. Equation (34) shows that the Elovich Kinetics rate deviates from the actual rate by a factor proportional to  $\exp(\Delta q_{c,e}^2)$ , which can become quite large for even small deviations. Therefore, Elovich kinetics cannot be applied to photodetectors in which there are significant changes in

$q_c$ . As will be discussed later, the change in  $q_c$  is determined by material parameters and illumination intensity. Thus, for many devices, Elovich kinetics does not apply.

These models can only be applied to planar devices; they do not apply to structures with curved surfaces such as nanowires, quantum dots, or other nanostructures. Additionally, they cannot be applied to systems in which the depletion width may cross a junction created either by dissimilar materials or by a difference in doping. Finally, the effect of additional adsorbates such as water are not considered. These considerations are important for predicting the performance of novel devices. The next section of this thesis will further develop these models to overcome these limitations.

## 3. METAL OXIDE PHOTOCONDUCTION MODEL

### 3.1 Introduction

The models presented in chapter 2 only apply for thick, planar devices, for small changes in  $q_c$ , and an exact time-domain form of the adsorption transient is not available. This makes analysis of high-gain and non-planar devices impossible. In this chapter we will expand on the metal oxide adsorption and photodesorption models presented in chapter 2. Here we derive new adsorption and photodesorption equations for modern photodetector structures such as thin films, nanowires, and heterojunctions. We will also discuss the effect of non-oxygen adsorbates on the photoresponse. Finally, we will discuss how to calculate the current of a photodetector from the adsorbed concentration.

### 3.2 Planar Adsorption

Here we explore the simplest case of adsorption kinetics on a thick, planar surface. This case shows the adsorbed concentration over time under the following assumptions:

1. The molecular trap level is close to the middle of the bandgap:  $E_T \sim E_i$
2. The bulk hole concentration is much smaller than the bulk electron concentration:  $p_b \ll n_b$
3. The physically adsorbed concentration is constant and much larger than the chemisorbed concentration:  $N_T \gg q_c$  and  $N_T$  is constant.
4. Thermal desorption is negligible:  $n_s N_T \gg n_1 q_c$
5. The material is much thicker than the depletion width:  $W \gg W_D$

This case is generally applicable to initial adsorption on the surface or photocurrent decays. Under these conditions, the general adsorption equation given by (12) is used. To solve for the time-domain solution of (12), we first rewrite it in a simplified form:

$$\frac{dq_c}{dt} = c_1 e^{-c_2 q_c^2} \quad (36)$$

$$c_1 = k_n N_T n_b \quad (37)$$

$$c_2 = \frac{q^2}{2kT\epsilon_s n_b} \quad (38)$$

Then we can rearrange the equation to take the integral:

$$\int_{q_c(0)}^{q_c(t)} e^{c_2 q_c^2} dq_c = \int_0^t c_1 dt \quad (39)$$

Then we make the substitution:

$$z = \sqrt{c_2} q_c \quad (40)$$

$$dz = \sqrt{c_2} dq_c \quad (41)$$

$$\frac{1}{\sqrt{c_2}} \int_{z(0)}^{z(t)} e^{z^2} dz = \int_0^t c_1 dt \quad (42)$$

$$\frac{\sqrt{\pi}}{2\sqrt{c_2}} \left( \operatorname{erfi}(z(t)) - \operatorname{erfi}(z(0)) \right) = c_1 t \quad (43)$$

$$q_c(t) = \frac{1}{\sqrt{c_2}} \operatorname{erfi}^{-1} \left( \frac{2\sqrt{c_2}}{\sqrt{\pi}} c_1 t + \operatorname{erfi}(\sqrt{c_2} q_c(0)) \right) \quad (44)$$

where  $q_c(0)$  is the initial condition,  $\operatorname{erfi}$  is the imaginary error function, and  $\operatorname{erfi}^{-1}$  is the imaginary inverse error function. To the author's knowledge, no program seems to provide the inverse imaginary error function, but the imaginary error function is available in MATLAB. Equation (44) can be written in terms of the imaginary error function:

$$t = \frac{\sqrt{\pi}}{2\sqrt{c_2} c_1} \left( \operatorname{erfi}(\sqrt{c_2} q_c) - \operatorname{erfi}(\sqrt{c_2} q_c(0)) \right) \quad (45)$$

Because (45) is a function of adsorbed concentration instead of time, sometimes it may be more convenient to solve (12) through numerical integration methods in order to specify the final time. For numerical stability and accuracy, it is better to solve the rate equation in its dimensionless form:

$$\frac{dQ_c}{d\tau} = \exp(-bQ_c^2) \quad (46)$$

$$Q_c = \frac{q_c}{N_T} \quad (47)$$

$$\tau = \frac{t}{k_n n_b} \quad (48)$$

$$b = \frac{q^2 N_T^2}{2kT\epsilon_s n_b} \quad (49)$$

Figure 8 shows an example plot of adsorption kinetics using (45) and (46) and  $q_c(0) = 0$ ,  $b = 1$ . The MATLAB built-in ordinary differential equation (ODE) solver ode15s is used to solve for  $q_c(t)$ . The calculated values from the ode solver are used in the calculation of the corresponding time values in (45).

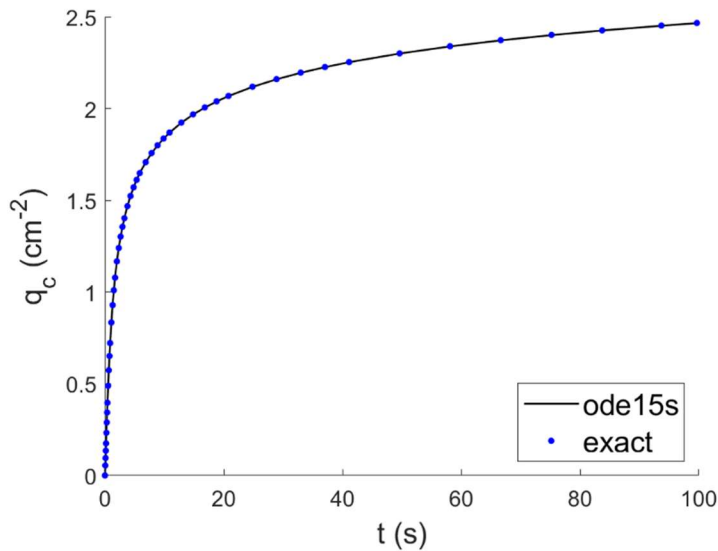


**Figure 8:** Adsorption rate equation solution for  $q_c(0) = 0$ ,  $b = 1$ . Solid black line is solution for (46) using MATLAB's built-in solver ode15s, and dotted blue line is exact solution using the dimensionless form of (45).

The transients in Figure 8 show the sharp initial rise in adsorbed concentration followed by a slow rise that is characteristic of metal oxide photoconductive decays. The numerical solution and the exact solution align closely. It is difficult to assess the error between the two because  $q_c$  is not calculated in (45).

The adsorption kinetics for a typical ZnO sample with parameters given in Table 1 is shown in Figure 9 (a). The adsorption transient again shows the rapid rise followed by the slow rise. With the exact solution to the adsorption rate equation, we can assess the accuracy of the Elovich kinetics equation for a typical sample. Figure 9 (b) shows Elovich kinetics transients for three different Taylor series expansion points. The plots show that each of the three Elovich kinetics transients quickly diverges from the exact solution as they move away from the Taylor series expansion point.

**Table 1: Material parameters for adsorption calculations shown in Figure 9.**

$k_n$ ( $\text{cm}^3/\text{s}$ )	$N_T$ ( $\text{cm}^{-2}$ )	$n_b$ ( $\text{cm}^{-3}$ )	$\epsilon_s$ ( $\text{F}/\text{cm}$ )
$1 \times 10^{-10}$	$1 \times 10^{15}$	$1 \times 10^{17}$	$7.434 \times 10^{-13}$

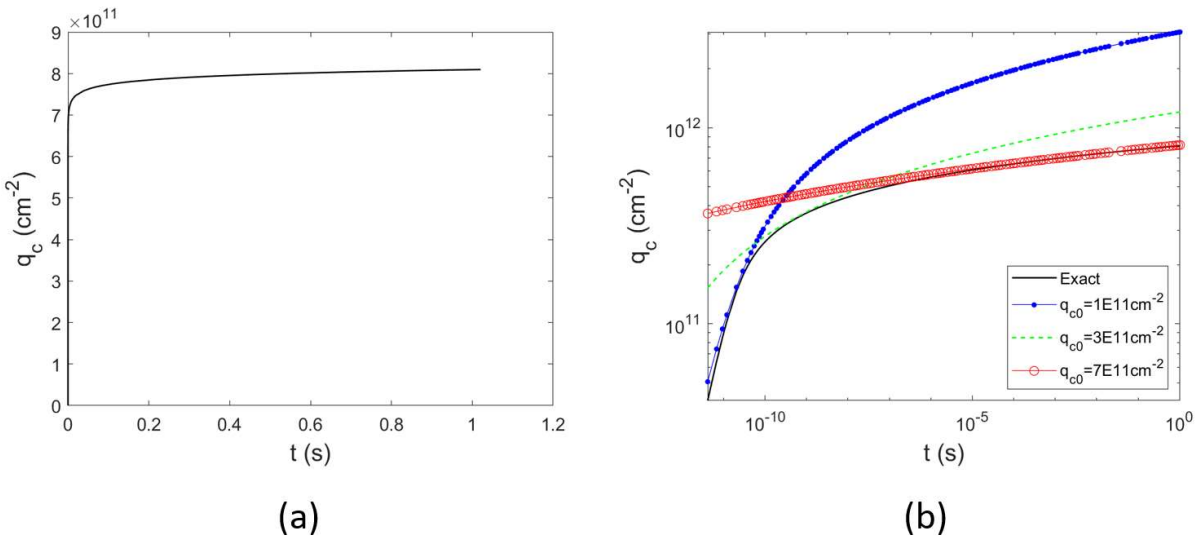


**Figure 9: (a) Adsorption transient calculated with (45) with material parameters shown in Table 1; (b) the same transient from (a) compared to Elovich Kinetics at Taylor Series expansion points  $q_{c0} = 1 \times 10^{11}$ ,  $3 \times 10^{11}$ , and  $7 \times 10^{11}$   $\text{cm}^{-2}$ .**

The error in the Elovich kinetics equation can be evaluated exactly by the difference between the exact solution and the Elovich kinetics time domain solution:

$$q_{c,err} = \frac{1}{\sqrt{c_2}} \operatorname{erfi}^{-1} \left( \frac{2\sqrt{c_2}}{\sqrt{\pi}} c_1 t + \operatorname{erfi}(\sqrt{c_2} q_c(0)) \right) - \frac{1}{\beta} \ln(e^{\beta q_c(0)} + \beta a t) \quad (50)$$

However, without access to  $\operatorname{erfi}^{-1}$ , (50) cannot be solved. A more useful way of examining the error may be to calculate the error in the rate of adsorption as in (34). From [23], the rate of adsorption as calculated by Elovich Kinetics can be related to the actual rate by:

$$\frac{dq_{c,e}}{dt} = A \frac{dq_c}{dt} \quad (51)$$

$$A = \exp \left( \frac{q^2 \Delta q_{c,e}^2}{2kT\epsilon_s n_b} \right) \quad (52)$$

$$\Delta q_{c,e} = q_c - q_{c0} \quad (53)$$

where  $q_{c,e}$  is the adsorbed concentration as calculated from Elovich kinetics. From (51) we can see that (1) Elovich kinetics always overestimates the adsorbed concentration, and (2) the difference between the rates increases exponentially as the adsorbed concentration changes from the Taylor series expansion point. We define the point at which the Elovich kinetics begin to diverge from the exact solution as value of  $\Delta q_{c,e}$  for which the Elovich kinetics rate is 10% greater than the actual rate:

$$\Delta q_{c,10\%} = \sqrt{\frac{2kT\epsilon_s n_b}{q^2} \ln(1.1)} \quad (54)$$

For the material parameters given in Table 1,  $\Delta q_{c,10\%} = 4.78 \times 10^{10} \text{cm}^{-2}$ . This means that the Elovich kinetics equation will begin to deviate from the exact solution significantly when the difference between the adsorbed concentration and the Taylor series expansion point is greater than  $4.78 \times 10^{10} \text{cm}^{-2}$ . Figure 10 (a) shows a plot of the  $A$  vs  $\Delta q_{c,e}$  for  $n_b = 1 \times 10^{17} \text{cm}^{-3}$ . It shows that  $A$  begins to increase rapidly after  $\Delta q_{c,e} = 4.78 \times 10^{10} \text{cm}^{-2}$ . Figure 10 (b) shows the percent error between the exact adsorbed

concentration and that calculated by Elovich kinetics for  $q_{c0} = 1 \times 10^{11} \text{ cm}^{-2}$  in Figure 9. The error is given by

$$error = \frac{q_{c,e} - q_c}{q_c} \times 100\% \quad (55)$$

The plot shows that the error starts to increase significantly after  $\Delta q_{c,e} = 4.78 \times 10^{10} \text{ cm}^{-2}$ .

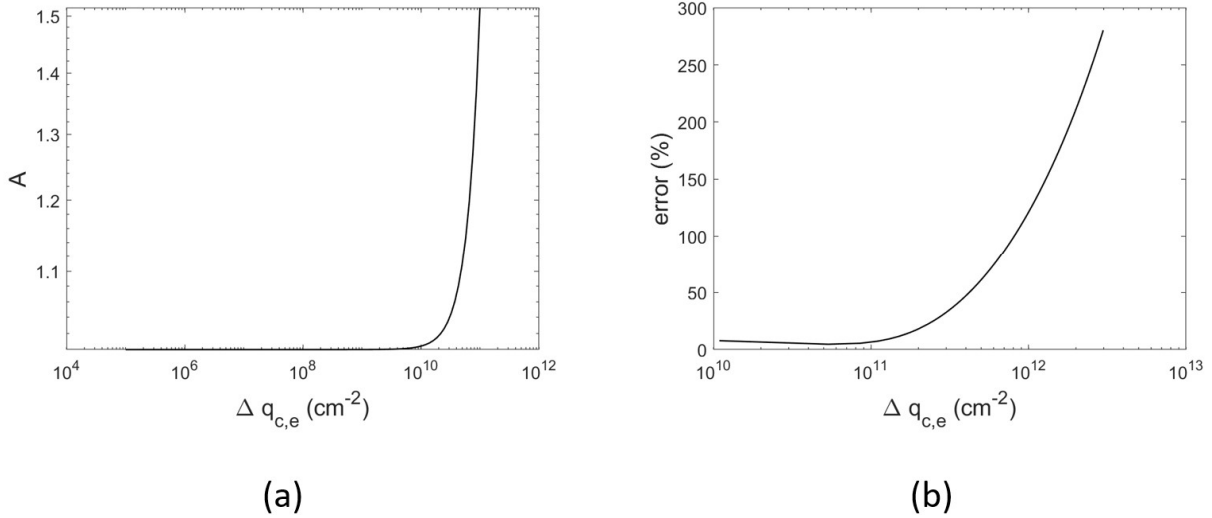


**Figure 10: (a) Multiplying factor between Elovich kinetics rate and exact rate as given by (51) for  $n_b = 1 \times 10^{17} \text{ cm}^{-3}$ ; (b) Percent error between exact adsorbed concentration and that calculated by Elovich kinetics for  $q_{c0} = 1 \times 10^{11} \text{ cm}^{-2}$  in Figure 9 (b).**

Finally, although (51) seems to imply that the error will be smaller for larger  $n_b$ , this is not the case. For larger  $n_b$ , the adsorption rate will increase and therefore will lead to larger adsorbed concentrations.

Therefore  $\Delta q_{c,10\%}$  will not increase significantly relative to the adsorbed concentration.

### 3.3 Steady-State

Steady-state occurs when the desorption rate becomes equal to the adsorption rate. Desorption can happen in two ways. A trapped electron can be thermally excited into the conduction band, or a hole can recombine with the trapped electron. So far, we have only considered the case where electron emission from the trap to the conduction band, called thermal desorption, is negligible. For sufficiently large  $q_c$ , we must consider electron emission from the adsorbed oxygen to the conduction band:

$$\frac{dq_c}{dt} = k_n \left[ N_T n_b \exp\left(\frac{qV_s}{kT}\right) - q_c N_c \exp\left(-\frac{E_{CS} - E_T}{kT}\right) \right] \quad (56)$$

This has steady-state:

$$q_{c,ss} = \sqrt{\frac{W\left(\frac{2bd^2}{c^2}\right)}{2b}} \quad (57)$$

$$b = N_t n_b \quad (58)$$

$$c = \frac{q^2}{2kT\epsilon_s n_b} \quad (59)$$

$$d = N_c \exp\left(-\frac{E_{CS} - E_T}{kT}\right) \quad (60)$$

where  $W$  is the Lambert-W function. The steady-state value depends strongly on the position of the trap-level. In ZnO, the oxygen trap is approximately 0.9eV below the conduction band ( $E_{CS} - E_T \approx 0.9\text{eV}$ ) [54], [55], and  $N_c = 1.76\text{E}17\text{cm}^{-3}$  [23]. For the material parameters given in Table 1, the steady-state value is  $q_c = 9.96 \times 10^{11}\text{cm}^{-2}$ . Applying (45), it would take  $9.48 \times 10^5\text{s}$  for the system to reach steady-state from an initial value of  $q_c = 0$ . Because the oxygen trap tends to be far below the conduction band in metal oxides, steady-state takes a very long time to reach and thermal desorption can be ignored.

A similar derivation can be made for bulk hole recombination with traps. Under sufficient band-bending, holes will recombine with captured electrons in the trap to limit adsorbed concentration:

$$\frac{dq_c}{dt} = k_n N_T n_b \exp\left(\frac{qV_s}{kT}\right) - k_p q_c p_b \exp\left(-\frac{qV_s}{kT}\right) \quad (61)$$

$$q_{c,ss} = \sqrt{\frac{\ln(e/f)}{-2c}} \quad (62)$$

$$e = k_p p_b \quad (63)$$

$$f = k_n N_T n_b \quad (64)$$

Metal oxides generally have small hole concentrations due to their wide bandgaps, so bulk hole recombination can be ignored.

### 3.4 Illumination Kinetics

Under illumination, photogenerated holes recombine with trapped electrons at the surface and reduce the surface potential. This process is shown in Figure 11. In Figure 11(a), a photon creates an electron-hole pair in the depletion region with initial width  $W_{D,0}$ . The electric field separates the electron-hole pair, pulling the hole to the surface and the electron to the bulk. The hole recombines with a trapped electron at the surface, leaving the photogenerated electron unpaired, as shown in Figure 11 (b). This causes a reduction in the depletion width and surface potential. The reduction in surface potential increases the rate of adsorption,  $R_{ads}$ . The reduction in surface potential will continue until the rate of adsorption is equal to the rate of desorption,  $R_{des}$ , which is equal to the rate of photogenerated holes to the surface. This steady-state is shown in Figure 11(c) where the rate of adsorption,  $R_{ads,SS}$ , is equal to the rate of desorption. Under illumination, the unpaired electrons contribute to the photocurrent. Once illumination is removed, the photogenerated electrons will become trapped again through adsorption and the depletion width will change from its illumination value,  $W_{D,SS}$ , to its initial value,  $W_{D,0}$ .

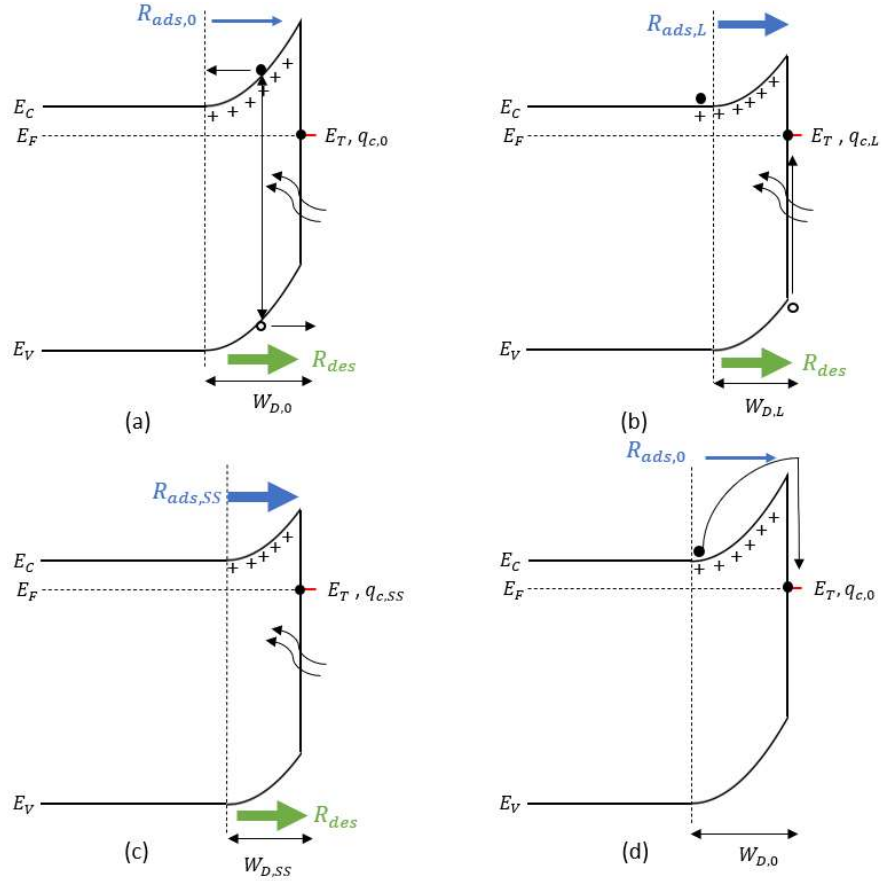


**Figure 11: Metal-oxide photoconduction process: (a) Illumination creates electron-hole pair in a system with initial adsorption rate  $R_{ads,0}$ , depletion width  $W_{D,0}$ , and adsorbed concentration  $q_{c,0}$ ; (b) hole recombines with trapped electron bound by oxygen on the surface, changing the depletion width to  $W_{D,L}$  and the adsorption rate to  $R_{ads,L}$ ; photogenerated electron resides in the neutral region of the bulk; (c) Illuminated steady-state is reached for  $R_{ads,SS} = R_{des}$ ; (d) after illumination is removed, electrons are recaptured by oxygen.**

Generally, in photoconductors, photogenerated carriers are excess carriers which change the bulk concentration of carriers. However, the photogenerated electrons whose hole pair has recombined at the surface will act as bulk electrons rather than excess carriers. Intuitively, this can be verified by seeing that the desorption process is the reverse of the adsorption process; trapped electrons are effectively released to the bulk under illumination. Such a process would create no excess carriers. Mathematically we can verify this by showing that the charge required to change the depletion width due to illumination is exactly equal to the charge created by the photogenerated electrons. The change in chemisorbed concentration due to recombination of holes is given by:

$$\Delta q_c = W_{D,0} p_L = W_{D,0} n_L \quad (65)$$

where  $p_L$  and  $n_L$  are the photogenerated hole and electron concentrations. The change in depletion width is then:

$$\Delta W_D = \frac{\Delta q_c}{N_D} = \frac{W_{D,0} n_L}{N_D} \quad (66)$$

The change in charge corresponding to this change in depletion width is:

$$\Delta Q = q N_D \Delta W_D A_D = q W_{D,0} n_L A_D \quad (67)$$

where  $A_D$  is the device area. This change in charge is equal to the total photogenerated electron charge:

$$Q_n = q n_L W_{D,0} A_D \quad (68)$$

Thus, the electron charge created by illumination,  $Q_n$ , is equal to the change in charge induced by the change in depletion width,  $\Delta Q$ ; all photogenerated electrons create a *neutral* region in the width  $\Delta W_D$ . They are in equilibrium ( $\Delta n_b = 0$  in this region) thus no recombination with holes in the bulk occurs. Instead, their lifetime is determined entirely by adsorption kinetics.

All photogenerated carriers created in the depletion width and a diffusion width away from the edge of the depletion width will have this type of response. If carriers are generated outside of this region, excess bulk carriers will be generated. These will increase the bulk carrier concentration but will not affect surface since they will recombine before diffusing into the depletion region. Therefore, bulk generation does not act to increase  $n_b$  in the adsorption rate equation.

In the case where photogenerated pairs are generated close to the surface and are not separated, the photogenerated electrons may be trapped by oxygen at the surface. This is referred to as photoadsorption and its effect is generally included in the  $\Delta n_b$  term. However, for a negative surface potential, the unpaired photogenerated hole will remain close to the trapped photogenerated hole and screen its charge and quickly recombine with it. Therefore, photoadsorbed electrons will have no effect on the potential other than to degrade the internal quantum efficiency of the device.

Based on these arguments for the behavior of photogenerated carriers in the depletion region and bulk, the excess carrier concentration term in (12) is assumed to be zero. Bulk generation is considered to occur parallel to photodesorption, and therefore it does not need to be considered in the photodesorption equation. To incorporate this photogeneration process into the adsorption process, a generation term is added to (12). Here we assume front-side illumination:

$$\frac{dq_c}{dt} = k_n N_T n_b \exp\left(\frac{qV_s}{kT}\right) - \int_0^{W_D + L_p} G_L(x) dx \quad (69)$$

$$L_p = \sqrt{\mu_p \frac{kT}{q} \tau_p} \quad (70)$$

$$G_L(x) = G_L(0)e^{-\alpha x} \quad (71)$$

where  $L_p$  is the hole diffusion length,  $\mu_p$  is the hole mobility,  $\tau_p$  is the hole lifetime,  $G_L$  is the carrier generation rate,  $G_L(0)$  is the generation rate at the surface, and  $\alpha$  is the absorption coefficient. The depletion width can be expressed in terms of the adsorbed concentration through (11). Evaluating the integral and simplifying yields:

$$\frac{dq_c}{dt} = k_n N_T n_b \exp\left(\frac{qV_s}{kT}\right) - \frac{G_L(0)}{\alpha} \left(1 - \exp\left(-\alpha \left(\frac{q_c}{n_b} + L_p\right)\right)\right) \quad (72)$$

To the author's knowledge, this equation is not soluble. It can, however, be solved numerically. To improve the accuracy of the numerical solution, we rearrange (72) into a dimensionless form:

$$\frac{dQ_c}{dT} = \exp(-bQ_c^2) - \Gamma + \Gamma \exp(-BQ_c - C) \quad (73)$$

$$\Gamma = \frac{G_L(0)}{k_n N_T n_b \alpha} \quad (74)$$

$$B = \frac{\alpha N_T}{n_b} \quad (75)$$

$$C = \alpha L_p \quad (76)$$

For sufficiently large depletion widths (both initial and final), the majority of the photogenerated electrons and holes occur within the depletion width, and we can ignore the third term:

$$\frac{dQ_c}{dT} = \exp(-bQ_c^2) - \Gamma \quad (77)$$

This equation has steady state:

$$Q_{c,ss} = \sqrt{\frac{\ln(\Gamma)}{-b}} \quad (78)$$

A typical ZnO sample has an absorption coefficient on the order of  $1 \times 10^5 \text{cm}^{-1}$  for 365nm light [56], a hole mobility of  $0.5 - 25 \text{cm}^2/\text{Vs}$  [57], and a recombination lifetime of  $\tau_p = 1 \mu\text{s}$ . The hole diffusion length for a sample with  $\mu_p = 0.5 \text{cm}^2/\text{Vs}$  would be  $L_p = 8 \mu\text{m}$ , and the exponential factor in (73) would be  $\exp(-\alpha L_p) = 1.8 \times 10^{-35}$ . This is sufficiently small to assume all photogenerated holes reach the surface. Ignoring the carriers swept up in the diffusion length, for a sample with  $\alpha = 1 \times 10^5 \text{cm}^{-1}$  a 10% difference in the illumination term will occur for  $W_D = 230 \text{nm}$ .

Note that (69) assumes that the photogenerated holes are swept to the surface relatively quickly. While this is true for holes generated within the depletion width, it may not be true for holes diffusing from the bulk to the surface. The time it takes for the bulk holes to reach the surface depends on their mobility and their distance from the edge of the depletion width. For some systems, (69) may need to be modified to account for the delay in the bulk photogenerated holes.

To account for surface excitation, we can include the term in (69). When surface excitation is included, we need to adjust  $G_L(x)$  to account for the reduction in incident photons on the bulk. Thus, (69) can be rewritten as:

$$\frac{dq_c}{dt} = k_n N_T n_b e^{\frac{qV_s}{kT}} - \int_0^{W_D+L_p} G'_L(x) dx - \sigma_{ph}^S q_c \Phi_{opt} \quad (79)$$

$$G'_L(x) = \alpha(1 - \sigma_{ph}^S q_c) \Phi_{opt} h\nu e^{-\alpha x} \quad (80)$$

where  $G'_L$  is the adjusted generation term,  $h$  is Planck's constant, and  $\nu$  is the frequency of the light. Although the optical capture cross-section has not yet been measured for most metal oxides, it is likely that devices with a high UV-Vis rejection ratio have a negligibly small capture cross-section. Any wavelength with energy above  $E_{CS} - E_T$  can excite the trapped electron to the conduction band. Therefore, materials which do not have a significant below bandgap response likely do not have significant surface excitation compared to bulk UV excitation.

Figure 12 shows illumination transients for a material with properties given in Table 1 and Table 2 and using (77). Equation (77) is solved in MATLAB with the numerical solver ode15s. The plots show that the decay is initially linear as  $\Gamma \gg \exp(-bQ_c^2)$ . The slope of the decay is then proportional to the illumination intensity, as demonstrated in the plot. As the adsorption rate approaches the desorption rate, there is a roll off in the transient and a steady-state is reached.

**Table 2: Material parameters for calculations in Figure 8.**

$\alpha$ ( $cm^{-1}$ )	$\tau_p$ ( $\mu s$ )	$\mu_p$ ( $cm^2/Vs$ )	$q_c(0)$ ( $cm^{-2}$ )
$1 \times 10^5$	1	0.5	$7 \times 10^{11}$

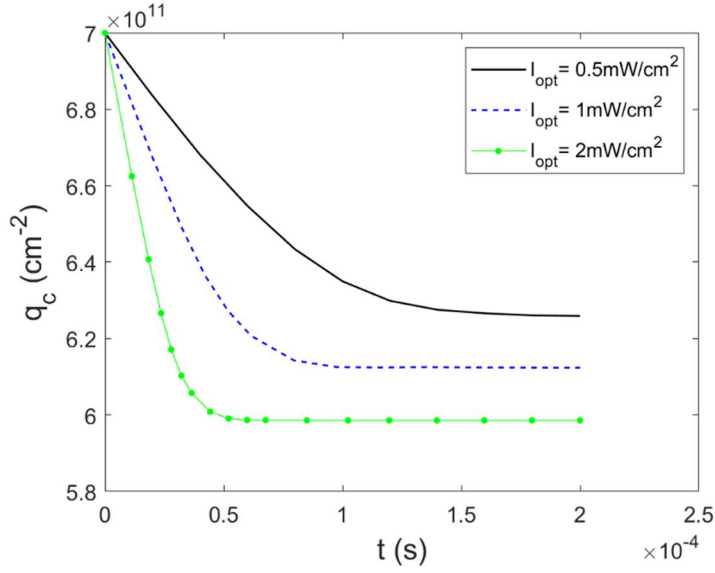


**Figure 12: Photodesorption transients for material with parameters in Table 1 and Table 2 using (77).**

Although there is not a time-domain solution to (73) or (77), Elovich kinetics can be used to obtain an accurate approximate solution. We substitute (16) in (72) and assume all photogenerated holes reach the surface:

$$\frac{dq_c}{dt} = ae^{-\beta q_c} - L \quad (81)$$

$$L = \frac{G_L(0)}{\alpha} \quad (82)$$

The time-domain solution to (81) is:

$$q_c(t) = \frac{1}{\beta} \ln \left( \frac{e^{\beta L(c-t)} + a}{L} \right) \quad (83)$$

$$c = \frac{1}{\beta L} \ln(L e^{\beta q_c(0)} - a) \quad (84)$$

Figure 13 shows (81) applied to the photodesorption transient from Figure 12. The error between the numerical solution and the fits is calculated as the difference between the two normalized to the change in adsorbed concentration from the initial value,  $q_c(0)$ . The plot with the Taylor series expansion point

$q_{c0} = q_c(0)$  has small error close to the point where  $q_c = q_{c0}$ , but it deviates significantly from the numerical solution in the steady-state region, as shown by the error plot in Figure 13 (b). The second plot has the Taylor series expansion point  $q_{c0} = q_{c,ss}$  which is calculated by (78). This plot has a much smaller error for both the rise and the steady-state portions of the transient. In general, (81) has a very small error when the Taylor series expansion point is chosen as the steady-state value. For  $q_c < q_{c,ss}$ , both (77) and (81) have desorption rates equal to  $L$ , and (77) and (81) have the same steady-state value. In the roll-off region, (81) will match (77) closely since  $\Delta q_c$  is small.

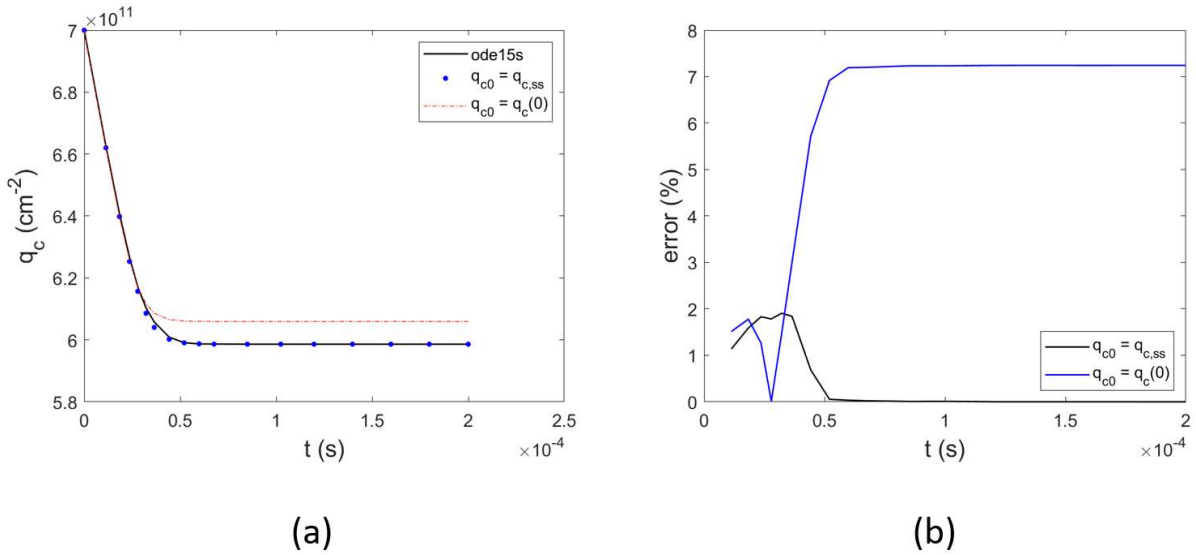


**Figure 13: (a) Photodesorption transient from Figure 12 with  $I_{\text{opt}} = 2\text{mW}$  and Elovich kinetics transients. The value of the steady-state concentration is  $q_{c,ss} = 5.986 \times 10^{11}\text{cm}^{-2}$  and the initial value is  $q_c(0) = 7 \times 10^{11}\text{cm}^{-2}$ ; (b) Error between (77) and (81) normalized to the range of the transient.**

Because (81) is approximately equal to (77) for  $q_{c0} = q_{c,ss}$ , we can use (81) to calculate the time to reach steady-state. The steady-state value is reached as  $t \rightarrow \infty$ , so we define the fall time as the time it takes to reach 95% of the steady-state value normalized to the transient range. The fall time is then given by:

$$t_F = \frac{1}{\beta L} \ln \left( \frac{L e^{\beta q_c(0)} - a}{L e^{\beta q_{c,F}} - a} \right) \quad (85)$$

$$q_{c,F} = q_c(0) - 0.95(q_c(0) - q_{c,ss}) \quad (86)$$

where  $q_{c,F}$  is 95% of the steady-state value.

The qualitative results shown here align well with experimental results of metal oxide photocurrent transients. Measurements of metal oxides photodetectors generally demonstrate a linear increase in photocurrent under illumination whose slope is proportional to the intensity of illumination [9], [46], [47], [58]. Some devices show a response which is not linear and does not seem to saturate [50], [59]. These materials are likely porous. As discussed in Section 2.4, porous materials have several parallel surfaces. Each surface will follow (72) but will have different incident illumination intensities. Thus, the response is the superposition of several photocurrents with different time constants. The deepest layers will have very low incident illumination intensities and therefore very slow response times that might not saturate for several hours.

### 3.5 Completely Depleted Device

Sections 3.2-3.4 consider the case of a very thick sample such that the depletion width is less than the total width of the device. However, many modern metal oxide photodetectors are thin films and the depletion width may extend past the width of the material. In this case, the surface potential will extend into the underlying substrate. In this section, we examine the case where that substrate is an insulating oxide layer, as shown in Figure 14. The figure shows a thin metal oxide semiconductor of width  $W$  on an insulating oxide layer. The conducting electrodes source (S) and drain (D) conduct current parallel to the adsorbing surface. A backgate electrode (BG) is placed on the insulating oxide surface. If no backgate is included in the device, then complete depletion will occur when all electrons in the sample have been adsorbed. After this, adsorption will stop. However, if there is a backgate, the surface potential will extend through to the backgate and allow adsorption to continue. This case is referred to as the completely depleted (CD) case whereas the case where  $W_D < W$  is referred to as partially depleted (PD).

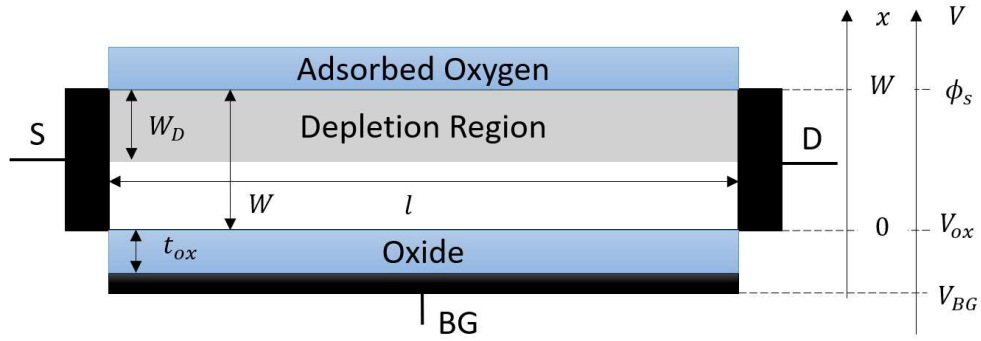


Figure 14: Completely depleted semiconductor with adsorbed molecules on the surface forming depletion region.

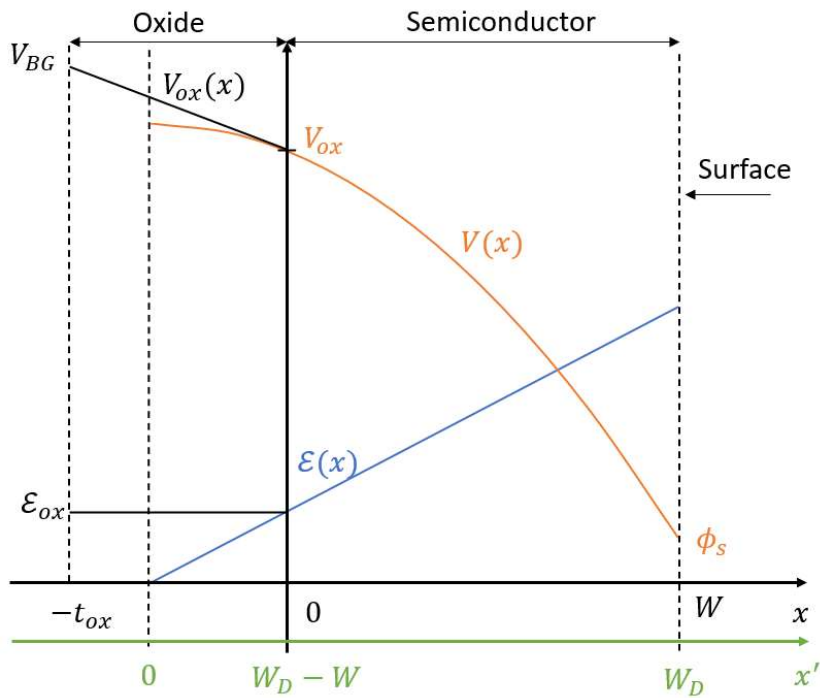


Figure 15: Diagram of electric field and voltage in the completely depleted case. The red and blue lines (Voltage and Electric field respectively) are shown extended through the oxide to demonstrate what they would be in the partially depleted case. This is meant only as a visual tool to show how  $\mathcal{E}_{ox}$  and  $W_D - W$  are defined in this system. The actual voltage and electric field in the oxide are shown by the black lines labelled  $V_{ox}(x)$  and  $\mathcal{E}_{ox}$ .

A diagram of the electrostatics for the system is shown in Figure 15. The figure shows two sets of axes:  $x$  and  $x'$ . The former is used to express the electrostatic variables in terms of the completely depleted geometry. The latter is used to represent a partially depleted system with the depletion width that would exist if it were allowed to extend into an infinitely thick semiconductor. To solve for the surface potential, we must first determine the electric field at the oxide-semiconductor interface,  $\mathcal{E}_{ox}$ . We can do

this by integrating  $\mathcal{E}(x')$  from  $x' = 0$  to  $W_D - W$ , where  $W_D$  is the depletion width that would exist for the given  $q_c$  in the partially depleted case. The equation for the electric field in the partially depleted case is:

$$\mathcal{E}(x') = \frac{qn_b}{\epsilon_s} x' \quad (87)$$

Thus, the field at the oxide-semiconductor interface is (87) evaluated at  $x' = W_D - W$ . The electric field can be related to the adsorbed concentration through (11):

$$\mathcal{E}_{ox} = \frac{qn_b}{\epsilon_s} \left( \frac{q_c}{n_b} - W \right) \quad (88)$$

Then,  $V_{ox}$  can be calculated from the electric field at the Oxide-Semiconductor interface:

$$V_{ox} = V_{BG} - \frac{t_{ox}\epsilon_s}{\epsilon_{ox}} \mathcal{E}_{ox} \quad (89)$$

$$V_{ox} = V_{BG} - \frac{qn_b t_{ox}}{\epsilon_{ox}} \left( \frac{q_c}{n_b} - W \right) \quad (90)$$

where  $\epsilon_{ox}$  is the dielectric permittivity of the oxide. Then, to find the semiconductor potential,  $V(x)$ , we use Poisson's Equation:

$$\int_{V(x=0)}^{V(x)} dV = - \int_0^x \mathcal{E}(x) dx \quad (91)$$

where

$$\mathcal{E}(x) = \frac{qn_b}{\epsilon_s} x + \mathcal{E}_{ox} \quad (92)$$

$$V(x = 0) = V_{ox} \quad (93)$$

Solving yields:

$$V(x) = -\frac{qn_b x^2}{2\epsilon_s} - \epsilon_{ox}x + V_{ox} \quad (94)$$

Then, the surface potential is:

$$\phi_s = V(W) = -qq_c \left( \frac{W}{\epsilon_s} - \frac{t_{ox}}{\epsilon_{ox}} \right) + \frac{qn_b W^2}{2\epsilon_s} + \frac{qn_b t_{ox} W}{\epsilon_{ox}} + V_{BG} \quad (95)$$

We can substitute  $\phi_s$  for  $V_s$  in (12), yielding the kinetics equation for the completely depleted case:

$$\frac{dq_c}{dt} = k_n N_T n_b e^{\frac{q\phi_s}{kT}} \quad (96)$$

This can be written in terms of  $q_c$  as:

$$\frac{dq_c}{dt} = c_1 e^{-\zeta q_c + \omega} \quad (97)$$

$$\zeta = \frac{q^2}{kT} \left( \frac{W}{\epsilon_s} - \frac{t_{ox}}{\epsilon_{ox}} \right) \quad (98)$$

$$\omega = \frac{qV_{BG}}{kT} + \frac{q^2 n_b W^2}{2kT\epsilon_s} + \frac{qn_b t_{ox} W}{kT\epsilon_{ox}} \quad (99)$$

The solution to (97) is:

$$q_c(t) = \frac{1}{\zeta} \ln(e^{\zeta q_c(0)} + \zeta c_1 e^{\omega t}) \quad (100)$$

In computation, evaluation of the term  $\exp(\omega)$  often yields infinity. To avoid this the equation is rearranged as:

$$q_c(t) = \frac{1}{\zeta} (\ln(e^{\zeta q_c(0) - \omega} + \zeta c_1 t) + \omega) \quad (101)$$

The approximate onset of CD occurs when the PD device would trap all electrons in the material. This occurs at adsorbed concentration given by:

$$q_{c,CD} = N_D W \quad (102)$$

This is the approximate onset because the depletion approximation has been used. The CD equations are only valid for  $q_c > q_{c,CD}$ . In a device with no backgate, at the onset of CD the adsorption rate will go to zero and no further adsorption will occur. However, in the CD device, the metal backgate will effectively be depleted and the surface will obtain electrons through the source and drain contacts.

Figure 16 shows example adsorption transients in the CD case. Figure 16 (a) shows transients for a sample with the parameters shown in Table 1 and Table 3 and a backgate voltage of  $V_{BG} = 0V$ . Three different oxide thicknesses are shown to demonstrate its effect on adsorption. Figure 9 shows the PD adsorption transient for the same material parameters but with  $W > W_D$  for all  $q_c$ . Comparing Figure 9 and Figure 16 (a), we can see that the presence of the oxide and backgate acts to slow down adsorption. Thicker oxides result in slower adsorption rates, with  $t_{ox} \rightarrow \infty$  being mathematically equivalent removal of the backgate. The backgate also allows for control over the adsorption rate. Negative biases reduce the rate of adsorption and positive biases increase the rate. This is shown in Figure 16 (b) where a bias of  $V_{BG} = 5V$  is applied. The adsorption rate increases significantly, and for the case of  $t_{ox} = 100nm$  is exceeds that of the PD case shown in Figure 9.

**Table 3: Parameters for CD device calculations in Figure 16.**

$W$ (nm)	$\epsilon_{ox}$ (F/cm)	$q_c(0)$ ( $cm^{-2}$ )
50	$7.425 \times 10^{-12}$	$5 \times 10^{11}$

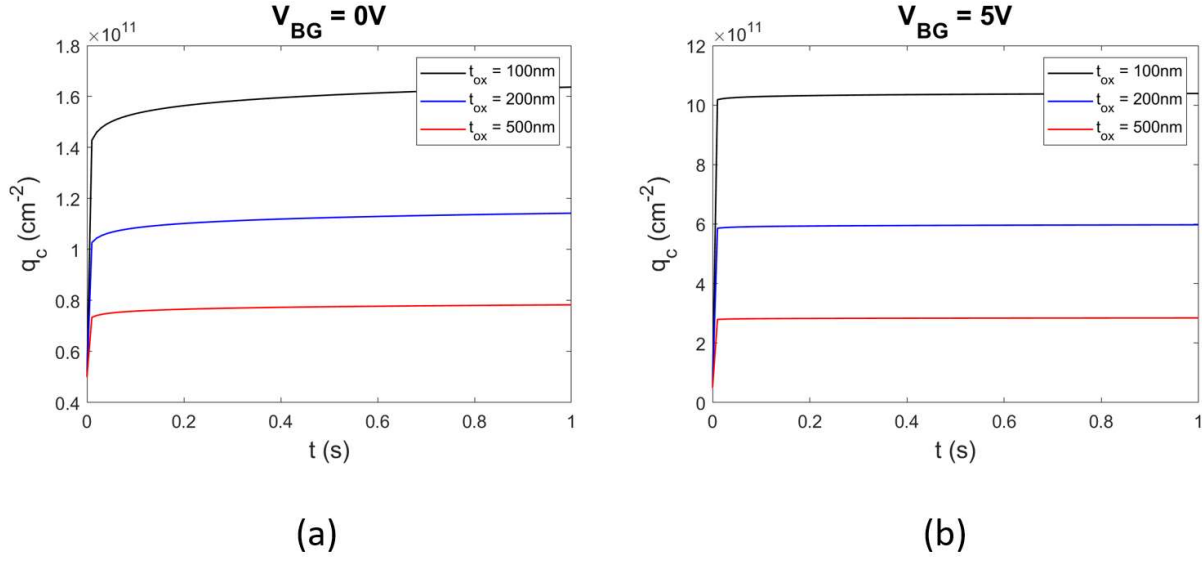


Figure 16: Adsorption transients for material parameters give in Table 1 and Table 3, different oxide thicknesses, and (a) backgate voltage of  $V_{BG} = 0V$  and (b)  $V_{BG} = 5V$ .

### 3.6 Completely Depleted Illumination Kinetics

The CD illumination kinetics equation can be determined by including an illumination term in (96). In the CD case, the depletion width occupies the entire width of the sample, so the generation term is integrated from  $x = 0$  to  $x = W$ :

$$\frac{dq_c}{dt} = k_n N_T n_b e^{-\zeta q_c + \omega} - \frac{G_L(0)}{\alpha} (1 - e^{-\alpha}) \quad (103)$$

The solution to (103) is:

$$q_c(t) = \frac{1}{\zeta} \left( \ln \left( \frac{1}{L} (c_1 - c_3 e^{-\zeta L t}) \right) + \omega \right) \quad (104)$$

$$c_3 = c_1 - L_{CD} e^{\zeta q_c(0) - \omega} \quad (105)$$

$$L_{CD} = \frac{G_L(0)}{\alpha} (1 - e^{-\alpha W}) \quad (106)$$

The system has steady-state adsorbed concentration given by:

$$q_{c,ss} = \frac{1}{\zeta} \left( \omega - \ln \left( \frac{L_{CD}}{c_1} \right) \right) \quad (107)$$

Figure 17 shows some example photodesorption transients for a CD sample with material parameters given by Table 1, Table 3, and Table 4. The shape of the transient is the same as for the PD case: a linear rise with slope  $L_{CD}$  and a roll off to a steady-state value.

**Table 4: Material parameters used to calculate photodesorption transient in Figure 17.**

$\alpha \text{ (cm}^{-1}\text{)}$	$q_c(0) \text{ cm}^{-2}$
$2 \times 10^5$	$5.45 \times 10^{11}$

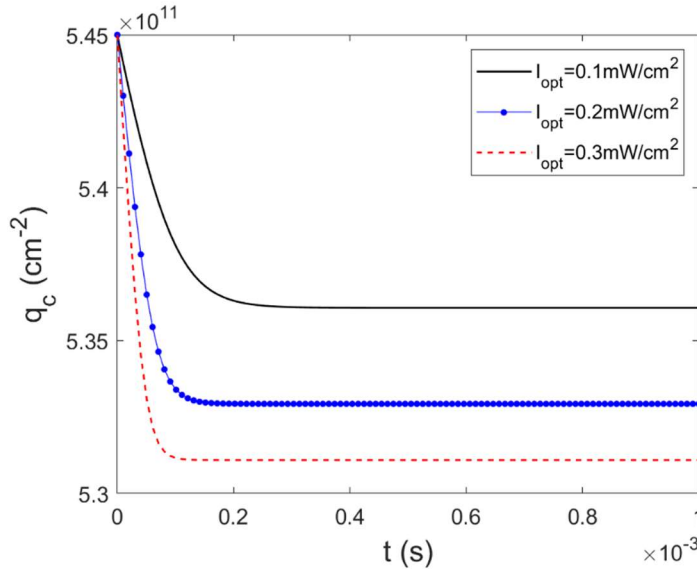


**Figure 17: Photodesorption transients for material with parameters given in Table 1, Table 3, and Table 4.**

### 3.7 Nanowires

The system electrostatics change with sample geometry. Therefore, (12) cannot be used for nanostructures such as nanowires or quantum dots. Here we examine the adsorption rate equation for metal oxide nanowires by solving for the surface potential in a cylindrical system with a surface charge and substituting that potential into the adsorption rate equation. The system analyzed is shown in Figure

18. The current flows parallel to the adsorption surface, and illumination is incident perpendicular to the flow of current.

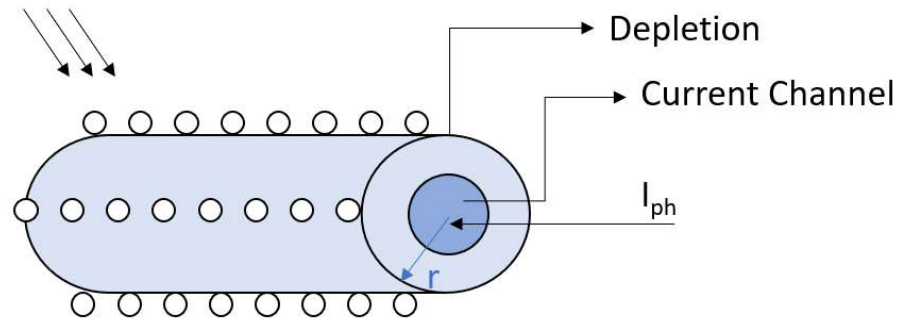


Figure 18: Nanowire with adsorbed molecules (white) and corresponding depletion region. Current moves parallel to surface and is modulated by depletion region.

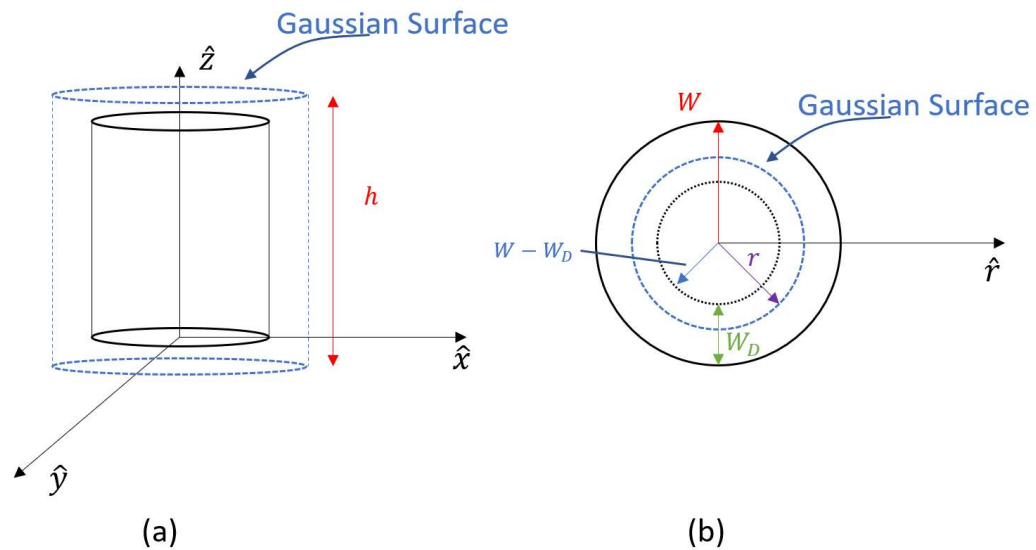


Figure 19: Nanowire electrostatics model, (a) orthogonal view, and (b) top view.

The adsorption rate equation for nanowires can be solved by using a Gaussian surface to solve for the electrostatics. We use the system shown in Figure 19 to represent the nanowire. The nanowire has radius  $W$ , depletion width  $W_D$ , volumetric charge density within the depletion region  $\rho_v = qN_D$ , and surface charge density  $\rho_s = qq_c$ . The electric flux density can be written as:

$$\vec{D} = D\hat{r} \quad (108)$$

The charge enclosed in the Gaussian surface is equal to the surface integral of the electric flux density:

$$Q_{inc} = \int_S \vec{D} \cdot d\vec{s} \quad (109)$$

The total charge enclosed within the Gaussian surface is equal to the charge in the encircled depletion region:

$$\int_0^{2\pi} \int_0^h \vec{D} \hat{r} \cdot \hat{r} r d\phi dz = qn_b h (\pi r^2 - \pi(W - W_D)^2) \quad (110)$$

Rearranging, we obtain the electric flux density as a function of radius:

$$D(r) = \frac{qn_b(r^2 - (W - W_D)^2)}{2r} \quad (111)$$

This yields the electric field:

$$\vec{E}(r) = \frac{\vec{D}}{\epsilon} = qn_b \frac{(r^2 - (W - W_D)^2)}{2r\epsilon_s} \hat{r} \quad (112)$$

From the electric field, the surface potential can be derived from Poisson's equation. We integrate the electric field from the edge of the depletion region to the surface:

$$V_{s,nw} = - \int_{(W-W_D)}^W \frac{qn_b(r^2 - (W - W_D)^2)}{2r\epsilon_s} \hat{r} \cdot \hat{r} dr \quad (113)$$

$$V_{s,nw} = - \frac{qn_b}{2\epsilon_s} \left( \frac{1}{2}(W^2 - (W - W_D)^2) + (W - W_D)^2 \ln \left( \frac{W - W_D}{W} \right) \right) \quad (114)$$

We can relate the surface potential to the surface charge by equating the surface charge with the net charge within the nanowire:

$$qn_b h \pi (W^2 - (W - W_D)^2) = qh 2\pi W q_c \quad (115)$$

$$W - W_D = \sqrt{W^2 - \frac{2q_c W}{n_b}} \quad (116)$$

Substituting (116) into (114), we obtain the surface potential in terms of the adsorbed concentration:

$$V_{s,nw} = -\frac{qn_b}{2\epsilon_s} \left( \frac{q_c W}{n_b} + W \left( 1 - \frac{2q_c}{Wn_b} \right) \ln \left( \sqrt{1 - \frac{2q_c}{Wn_b}} \right) \right) \quad (117)$$

The surface potential in (117) can be substituted into (12) to solve for  $q_c$ .

$$\frac{dq_c}{dt} = k_n N_T n_b e^{\frac{qV_{s,nw}}{kT}} \quad (118)$$

The current can be calculated from the depletion width equation as a function of  $q_c$  by:

$$W_D = W \left( 1 - \sqrt{1 - \frac{2q_c}{Wn_b}} \right) \quad (119)$$

The system must be solved by numerical methods, so we rewrite the adsorption rate equation in dimensionless form:

$$\frac{dQ_c}{dT} = \exp(-\delta Q_c - \theta(1 - \gamma Q_c) \ln(\sqrt{1 - \gamma Q_c})) \quad (120)$$

$$\gamma = \frac{2N_T}{Wn_b}, \quad \delta = \frac{q^2 N_T W}{2kT\epsilon_s}, \quad \theta = \frac{q^2 n_b W}{2kT\epsilon_s} \quad (121)$$

Example nanowire adsorption transients are shown in Figure 20. The plot shows that the adsorption rate decreases with increasing surface curvature. Nanowires generally have a much smaller volume than thin films and single crystals, and therefore will be depleted much faster. The onset of CD will occur for  $W = W_D$ . From (116), CD occurs at the adsorbed concentration of

$$q_{c,CD} = \frac{Wn_b}{2} \quad (122)$$

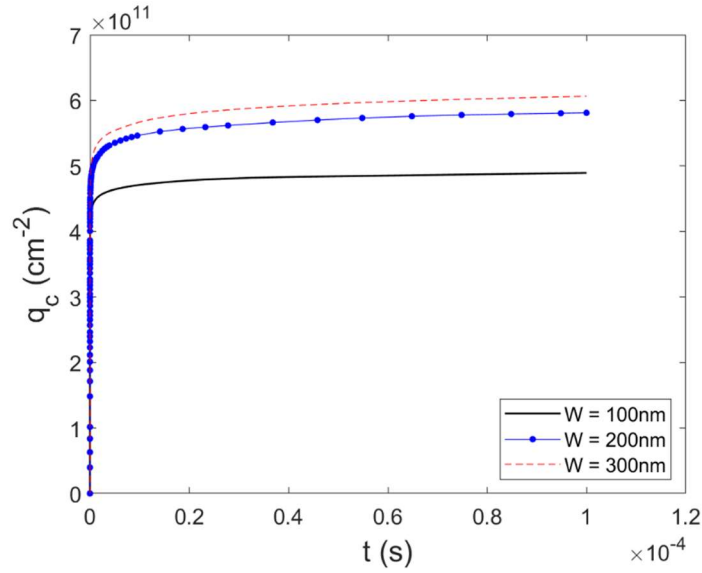


**Figure 20: Adsorption transients for material parameters given in Table 1 and various diameters.**

Equation (118) may have a different adsorption rate constant,  $k_n$ , than the planar materials. For wurtzite metal oxides such as ZnO, most planar devices grow with their c-axis perpendicular to the surface such that the polar (0001) and (000-1) planes are exposed to oxygen. However, the exposed faces on wurtzite nanowires may include the non-polar faces. Each face will likely have a different adsorption rate constant, and therefore (118) will need to be modified accordingly.

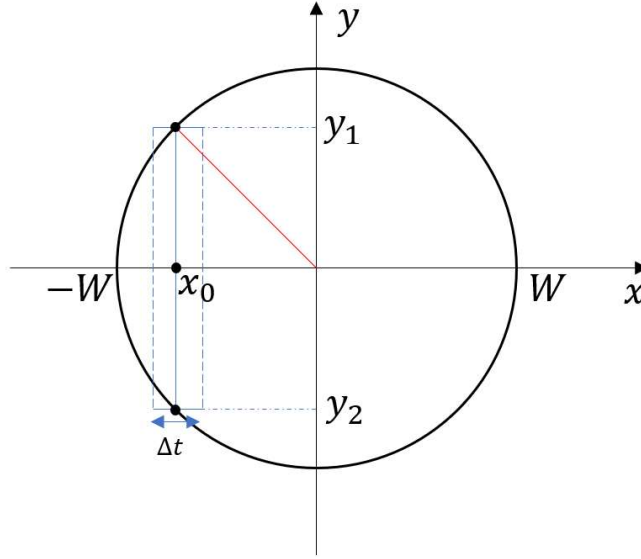


**Figure 21: Nanowire cross-section with infinitesimally thin rectangle centered on  $x = x_0$  and with width  $\Delta t$ .**

The illumination term for nanowires can be included as a desorption rate term as was done in Sections 3.4 and 3.6. However, the absorption of photons in a nanowire differs from that of a planar device. We derive the rate term by integrating over the surface of the nanowire cross-section shown in Figure 21. We examine a differential section of the circle denoted by the rectangle centered at  $x_0$  with width  $\Delta t$ . The generation rate in this section is given by:

$$G_L(y) = G_L(0)e^{-\alpha(y-y_1)} \quad (123)$$

The total number of photons per second absorbed in the volume defined by this section is given by integration:

$$p_{\Delta t} = l\Delta t \int_{y_1}^{y_2} G_L(y) dy \quad (124)$$

$$= \frac{l\Delta t G_L(0)}{\alpha} (1 - e^{-\alpha(y_2-y_1)}) \quad (125)$$

where  $l$  is the length of the nanowire. The depth of the section can be rewritten in terms of the nanowire radius as:

$$= \frac{l\Delta t G_L(0)}{\alpha} \left( 1 - e^{-\alpha \sqrt{W^2 - x_0^2}} \right) \quad (126)$$

We can solve for the total number of photons generated per second in the whole cylinder by integrating across the area of the circle:

$$p_{NW} = \frac{lG_L(0)}{\alpha} \int_{-W}^W 1 - e^{-\alpha \sqrt{W^2 - x^2}} dx \quad (127)$$

Equation (127) does not have a closed-form solution, so it must be solved via a numerical solver. We assume that the total number of absorbed photons is distributed evenly across the surface of the nanowire, thus the rate of electrons to the surface is:

$$L_{NW} = \frac{p_{NW}}{2\pi Wl} \quad (128)$$

This assumption may not be valid in many cases. For example, if most of the photons are absorbed near the surface. Note that we also do not consider the effect of the depletion width on the generation rate. Such an analysis is better performed in a software package such as Sentaurus and therefore will not be done here. However, many nanowires have a diameter that is relatively small compared to both the absorption length and the diffusion length, so this equation is suitable for many practical devices. The photodesorption rate equation is then:

$$\frac{dq_c}{dt} = k_n N_T n_b e^{\frac{qV_{s,nw}}{kT}} - L_{NW} \quad (129)$$

### 3.8 Quantum Dots

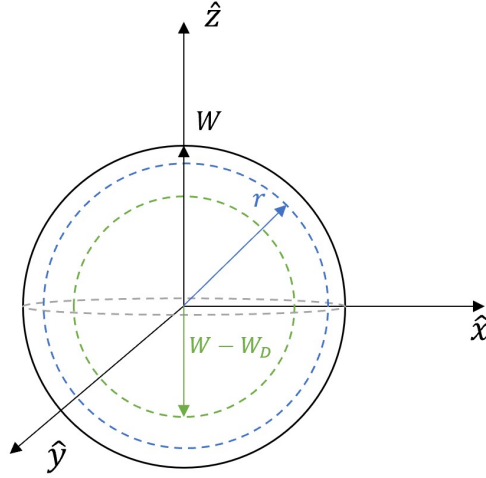


**Figure 22: Quantum electrostatics model and Gaussian surface (dashed blue line).**

Metal oxide quantum dots are researched extensively due to the ability to control the optical bandgap with the size of the quantum dot. The curvature of their surface will change the adsorption rate and their optical response. Similar electrostatics arguments can be made to derive the adsorption rate equation for quantum dots. The electrostatics model is shown in Figure 22. We approximate the shape of the quantum dots to be a sphere and use a Gaussian surface to derive the surface potential. The charge enclosed by the Gaussian surface is equal to the surface integral of the electric flux density:

$$\oint_S \vec{D} \cdot d\vec{s} = Q_{incl} \quad (130)$$

$$\vec{D} = D\hat{r} \quad (131)$$

The total charge enclosed within the Gaussian surface is equal to the charge in the encircled depletion region:

$$\int_0^{2\pi} \int_0^\pi D\hat{r} \cdot \hat{r} r^2 \sin \theta d\theta d\phi = \frac{4\pi q n_b}{3} (r^3 - (W - W_D)^3) \quad (132)$$

Thus, we can solve for the electric flux density and the electric field:

$$D = \frac{qn_b(r^3 - (W - W_D)^3)}{r^3} \quad (133)$$

$$\vec{E} = \frac{D}{\epsilon_s} \hat{r} = \frac{qn_b}{\epsilon_s} \frac{(r^3 - (W - W_D)^3)}{r^3} \quad (134)$$

Using Poisson's equation, we solve for the surface potential:

$$V_{s,QD} = - \int_{(W-W_D)}^W \vec{E} \hat{r} \cdot \hat{r} dr \quad (135)$$

$$V_{s,QD} = - \frac{qn_b}{\epsilon_s} \left( W_D + \frac{(W - W_D)^3}{2W^2} - \frac{W - W_D}{2} \right) \quad (136)$$

We can relate the surface potential to the adsorbed concentration by equating the total charge adsorbed to the total charge in the depletion width:

$$\frac{4\pi qn_b}{3} (W^3 - (W - W_D)^3) = 4\pi W^2 q q_c \quad (137)$$

$$W - W_D = W \sqrt[3]{1 - \frac{3q_c}{Wn_b}} \quad (138)$$

$$V_{s,QD} = - \frac{qn_b}{\epsilon_s} \left( W - \frac{3W}{2} \sqrt[3]{1 - \frac{3q_c}{Wn_b}} + \frac{W}{2} \left( 1 - \frac{3q_c}{Wn_b} \right) \right) \quad (139)$$

The adsorption equation is then written by substituting (139) into (12):

$$\frac{dq_c}{dt} = k_n N_T n_b e^{\frac{qV_{s,QD}}{kT}} \quad (140)$$

The dimensionless for of (140) is:

$$\frac{dQ_c}{dT} = \exp\left(-\psi\left(1 - \frac{3}{2}\sqrt[3]{1 - \kappa Q_c} + \frac{1}{2}(1 - \kappa Q_c)\right)\right) \quad (141)$$

$$\psi = \frac{q^2 n_b W}{kT \epsilon_s} \quad (142)$$

$$\kappa = \frac{2N_T}{W n_b} \quad (143)$$

The adsorption transients for some example quantum dots are shown in Figure 23. The adsorption rate is much slower than that of the nanowires, and it decreases with decreasing radius. Quantum dots also have a much smaller volume of charges to contribute to adsorption, and so their onset of CD will occur at a very small adsorbed concentration given by

$$q_{c,CD} = \frac{W n_b}{3} \quad (144)$$

As with nanowires, the adsorption constant,  $k_n$ , for quantum dots may differ significantly from that for planar devices. The quantum dot will have many different faces exposed, each of which may have a different adsorption constant, and the exposed edges and of the structures may alter the adsorption rate.

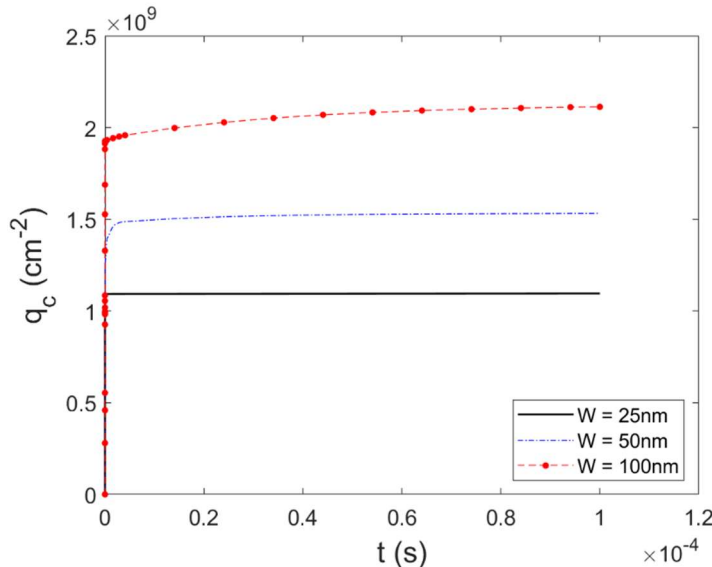


Figure 23: Adsorption transients for quantum dots with different radii and material parameters given in Table 1.

Illumination can be included in the rate equation through a desorption term as was done for other systems. However, we do not derive the form of the illumination term here. It is important to note, however, that a device with large groups of quantum dots stacked on top of each other will experience a photoresponse similar to the porous structures discussed in Section 2.4. That is, different layers will have different incident illumination intensities as the surface layers absorb light.

### 3.9 Junctions

#### 3.9.1 Homojunction

Homojunctions consist of two sections of the same material that have different carrier concentrations. This is a more realistic representation of many metal oxide materials as the number of oxygen vacancies which act as electron donor sites may vary throughout the material. Here we examine the electrostatics for the system shown in Figure 24.

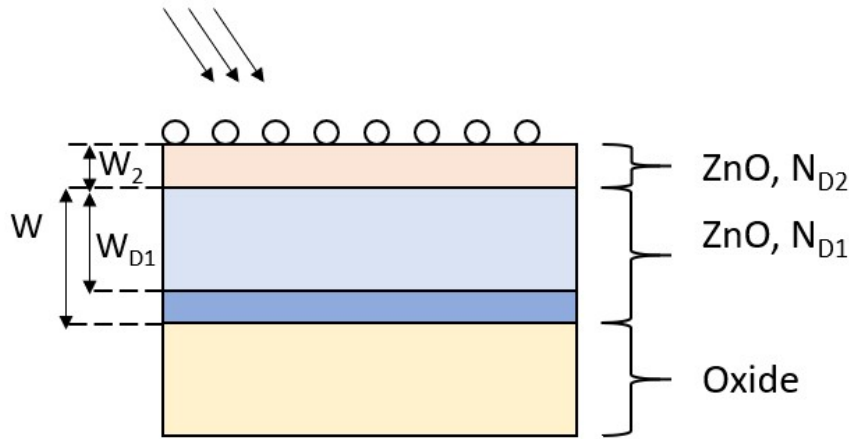


Figure 24: Homojunction device with two different carrier concentrations.

We consider only the case where  $W_2$  is completely depleted. This requires that the adsorbed concentration be:

$$q_c > W_2 N_{D2} \quad (145)$$

The surface potential can be solved by integrating the electric field from the edge of the depletion region to the surface:

$$V_{s,HJ} = - \int_0^{W_2} \frac{qN_{D2}}{\epsilon_s} dx - \int_0^{W_{D1}} \frac{qN_{D1}}{\epsilon_s} dx \quad (146)$$

$$V_{s,HJ} = - \frac{q}{2\epsilon_s} (N_{D2}W_2^2 + N_{D1}W_{D1}^2) \quad (147)$$

Then the surface potential can be related to the adsorbed concentration by equating the adsorbed charge to the charge in the depletion region:

$$q_c = N_{D1}W_{D1} + N_{D2}W_2 \quad (148)$$

$$V_{s,HJ} = - \frac{q}{2\epsilon_s} \left( \frac{q_c^2}{N_{D1}} - \frac{2N_{D2}W_2}{N_{D1}} q_c W_2^2 N_{D2} \left( 1 + \frac{N_{D2}}{N_{D1}} \right) \right) \quad (149)$$

The adsorption rate equation is written by substituting (149) into (12):

$$\frac{dq_c}{dt} = k_n N_{D2} N_T e^{\frac{qV_{s,HJ}}{kT}}, \quad q_c > N_{D2}W_2 \quad (150)$$

$$\frac{dQ_c}{dT} = \exp(-XQ_c^2 + YQ_c - Z) \quad (151)$$

$$X = \frac{q^2 N_T^2}{2kT\epsilon_s N_{D1}} \quad (152)$$

$$Y = \frac{q^2 N_{D2} N_T W_2}{kT\epsilon_s N_{D1}} \quad (153)$$

$$Z = \frac{q^2 W_2^2 N_{D2}}{2kT\epsilon_s} \left( 1 + \frac{N_{D2}}{N_{D1}} \right) \quad (154)$$

Figure 25 and Figure 26 show the adsorption transients and depletion width and rate of adsorption over time for various homojunction structures. In both we examine a heterojunction with a thin film of  $W_2 = 50\text{nm}$  on top of a thick substrate such that the device does not enter CD. In Figure 25, we compare homojunctions where the surface layer has a higher carrier concentration than the underlying bulk layer. Each junction is compared to a non-homojunction with a homogenous carrier concentration. From Figure 25, we can see that the adsorption rate is not significantly affected by the homojunction; the adsorption rate mostly follows that of the substrate layer instead of the surface layer. There is a change in the total amount adsorbed on the surface that is equal to the charge in the surface layer. Thus, the homojunction will adsorb the surface layer charge and then mostly follow the adsorption rate of the underlying bulk. A similar scenario is seen in Figure 26 for homojunctions with a smaller carrier concentration on the surface layer.

### Homojunction for $N_{D1} < N_{D2}$

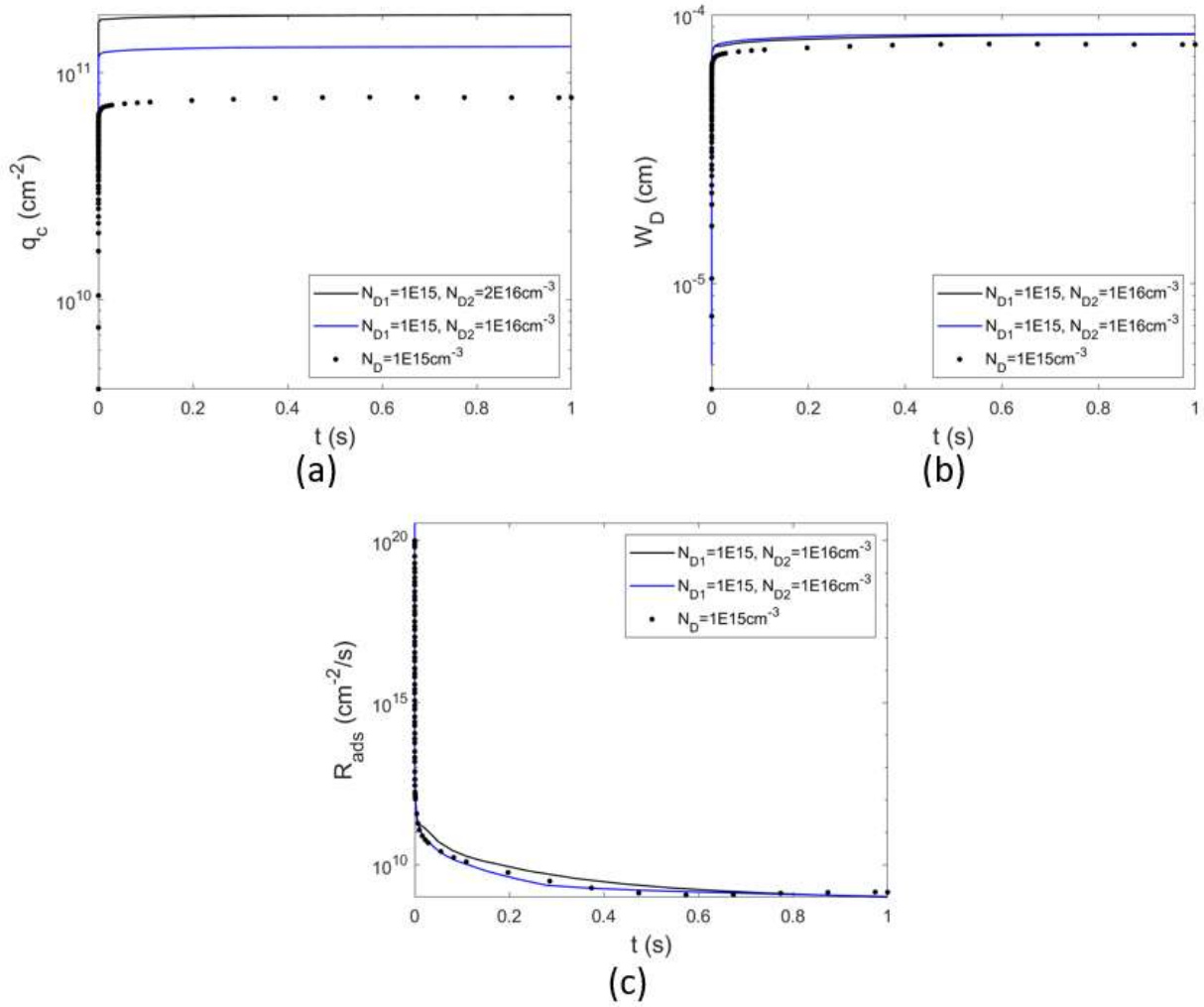


Figure 25: (a) Adsorption transients, (b) depletion width transients, and (c) rate of adsorption over time for homojunctions with the material parameters listed in Table 1 and  $W_2 = 50\text{nm}$ .

### Homojunction for $N_{D1} > N_{D2}$

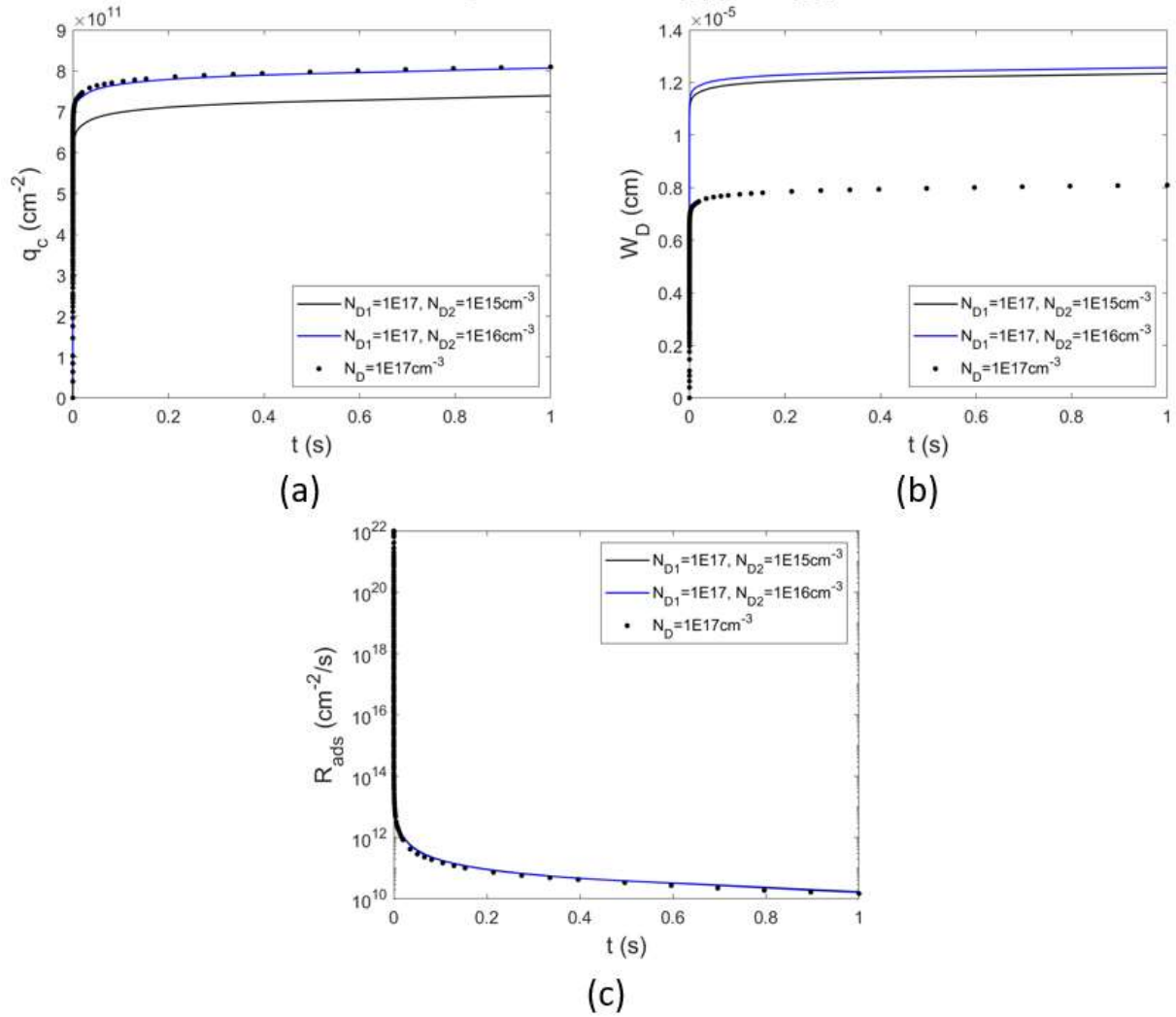


Figure 26: (a) Adsorption transients, (b) depletion width transients, and (c) rate of adsorption over time for homojunctions with the material parameters listed in Table 1.

### 3.9.2 Heterojunction

Metal oxide heterojunctions, like the one shown in Figure 27, have been used recently to improve the performance of metal oxide UV photodetectors [11], [60]–[64]. Generally, the metal oxide is combined with a high-mobility material such as graphene to increase the photoresponsivity of the device. Here we examine the effect of a heterojunction on the adsorption rate. We do not consider the effect of interfacial charge or interfacial barriers.

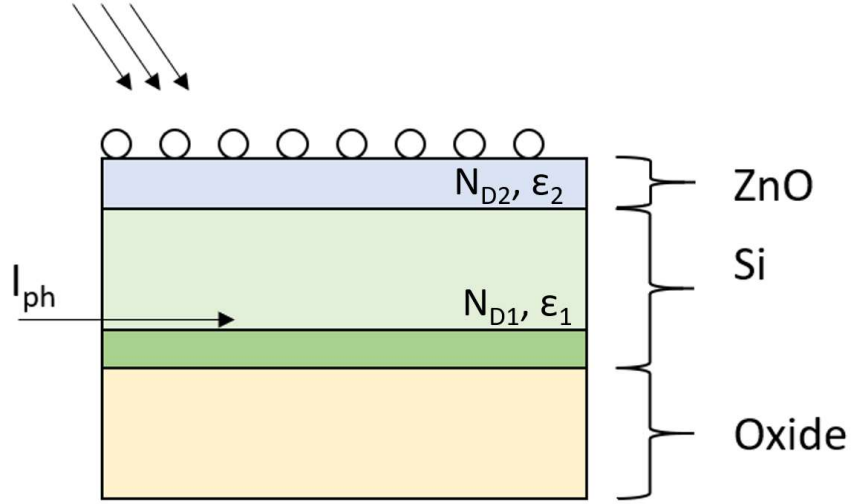


Figure 27: Example ZnO-Si heterojunction.

The rate equation can be derived in the same manner as for homojunctions, but with different dielectric permittivities. The resulting surface potential is given by:

$$V_{s,HJ} = -\frac{q}{2} \left( \frac{q_c^2}{N_{D1}\epsilon_{s,1}} - \frac{2N_{D2}W_2}{N_{D1}\epsilon_{s,2}} q_c W_2^2 N_{D2} \left( \frac{1}{\epsilon_{s,2}} + \frac{N_{D2}}{\epsilon_{s,1}N_{D1}} \right) \right) \quad (155)$$

The dimensionless form of the rate equation is:

$$\frac{dQ_c}{dT} = \exp(-UQ_c^2 + VQ_c - WZ) \quad (156)$$

$$U = \frac{q^2 N_D^2}{2kT\epsilon_{s,1}N_{D1}} \quad (157)$$

$$Y = \frac{q^2 N_{D2} N_T W_2}{kT\epsilon_{s,1}N_{D1}} \quad (158)$$

$$Z = \frac{q^2 W_2^2 N_{D2}}{2kT} \left( \frac{1}{\epsilon_{s,2}} + \frac{N_{D2}}{\epsilon_{s,1}N_{D1}} \right) \quad (159)$$

Figure 28 shows that the heterojunction follows the same trends as the homojunction. That is, the adsorption rate mostly follows that of the underlying substrate.

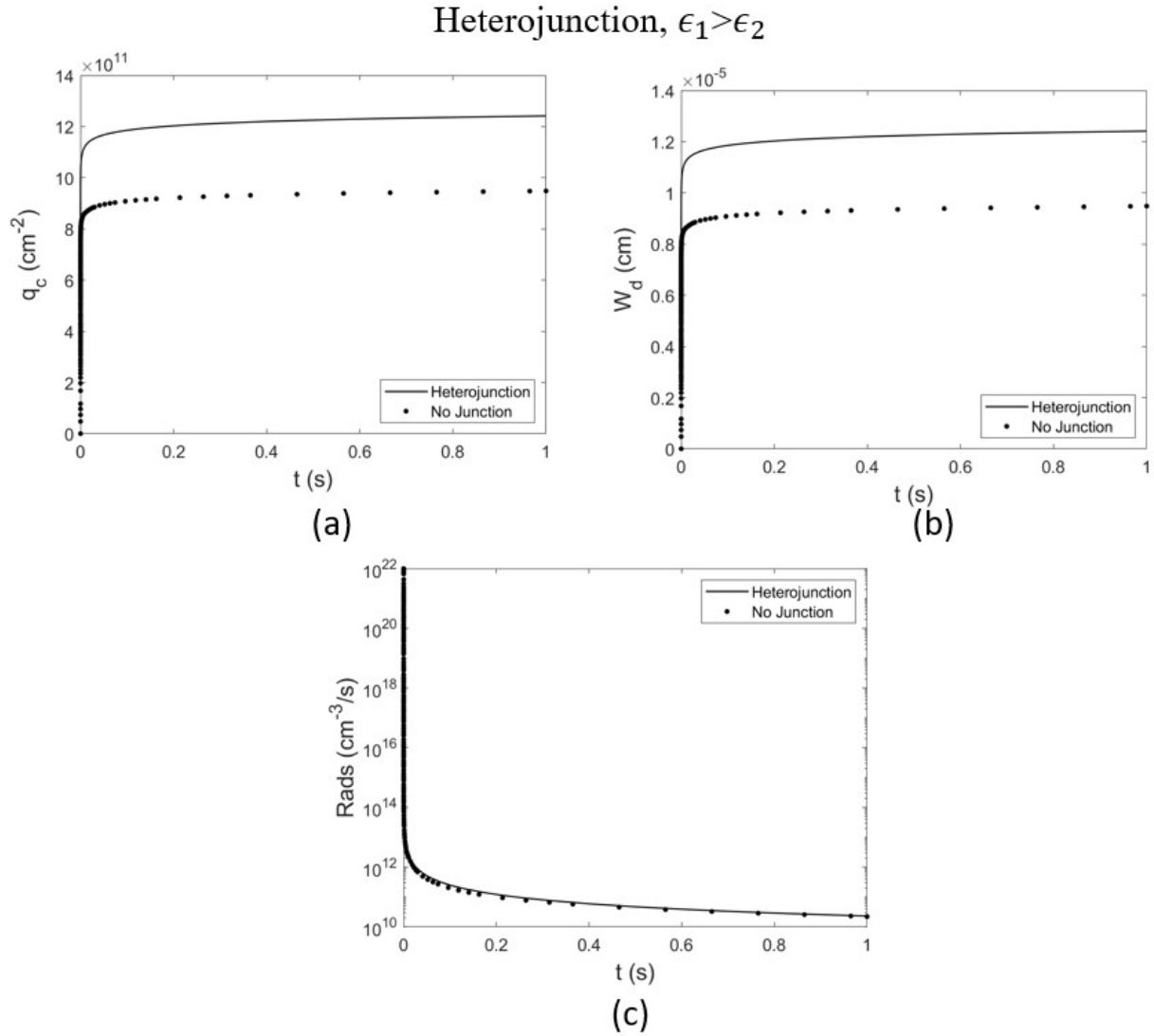


**Figure 28: Adsorption transients for homojunction with  $N_{d1} = N_{d2} = 1 \times 10^{17} \text{ cm}^{-3}$ ,  $W_2 = 50 \text{ nm}$ ,  $\epsilon_{r,1} = 11.9$ ,  $\epsilon_{r,2} = 8.4$ , and junction with  $n_b = 1 \times 10^{17} \text{ cm}^{-3}$ ,  $\epsilon_{r,2} = 11.9$ .**

### 3.10 Multiple Traps

#### 3.10.1 Multiple Acceptor Type Traps

Metal oxides are generally sensitive to gases other than oxygen, such as carbon dioxide, carbon monoxide, hydrogen, and methane. Therefore, it is important to look at the effect of multiple traps on the surface on the adsorption rate. If there are two acceptor-type traps with different adsorption sites and adsorption rates, we can write an adsorption rate equation for both of them:

$$\frac{dq_{c1}}{dt} = k_{n1}N_{T1}n_b e^{\frac{qV_s}{kT}} \quad (160)$$

$$\frac{dq_{c2}}{dt} = k_{n2}N_{T2}n_b e^{\frac{qV_s}{kT}} \quad (161)$$

The total negative trapped charge concentration on the surface can be written as the sum of the individual adsorbed concentration:

$$q_{c,T} = q_{c1} + q_{c2} \quad (162)$$

The surface potential is then given by the total adsorbed concentration:

$$V_s = -\frac{qq_{c,T}^2}{2\epsilon_s n_b} \quad (163)$$

We can write a rate equation for the total adsorbed concentration as a sum of the individual rate equations:

$$\frac{dq_{c,T}}{dt} = (k_{n1}N_{T1} + k_{n2}N_{T2})e^{\frac{qV_s}{kT}} \quad (164)$$

Thus, the rate equation for multiple acceptor type traps has the same form as (12) but with an effective adsorption rate constant and trap concentration. The dimensionless form of (160) and (161) are given by:

$$\frac{dQ_{c,1}}{dT} = e^{-c_2 Q_{c,T}^2} \quad (165)$$

$$\frac{dQ_{c,2}}{dT} = e^{c_4 - c_2 Q_{c,T}^2} \quad (166)$$

$$c_4 = \ln\left(\frac{k_{n2} N_{T2}}{k_{n1} N_{T1}}\right) \quad (167)$$

$$Q_{c,1} = \frac{q_{c,1}}{N_{t1}} \quad (168)$$

$$Q_{c,2} = \frac{q_{c,2}}{N_{t,1}} \quad (169)$$

$$Q_{c,T} = Q_{c,1} + Q_{c,2} \quad (170)$$

$$T = tk_{n1}n_b \quad (171)$$

The dimensionless form of (164) is given by:

$$\frac{dQ_{c,T}}{dT} = e^{c_5 - c_2 Q_{c,T}^2} \quad (172)$$

$$c_5 = \ln\left(1 + \frac{k_{n2} N_{T2}}{k_{n1} N_{T1}}\right) \quad (173)$$

Figure 29 shows the calculated adsorption transient for a material with two traps with different adsorption rate constants.

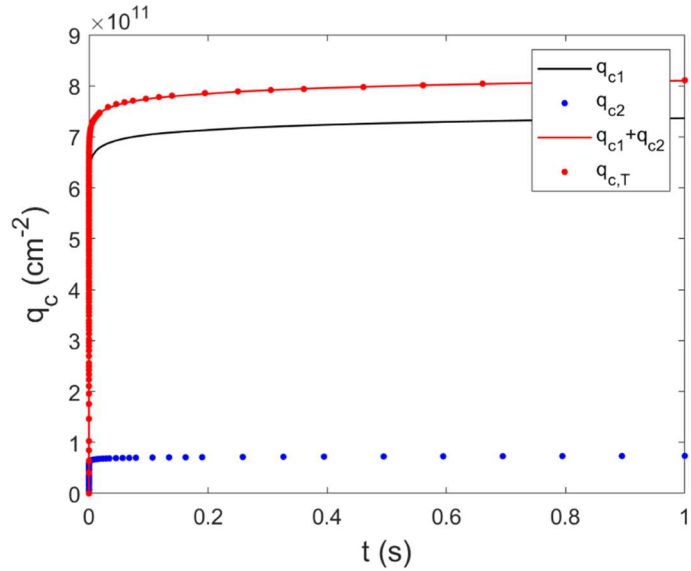


Figure 29: Adsorption transients for multiple traps with  $n_b = 1 \times 10^{17} \text{ cm}^{-3}$ ,  $N_{t1} = N_{t2} = 1 \times 10^{15} \text{ cm}^{-2}$ ,  $q_{c1}(0) = 0$ ,  $q_{c2}(0) = 0$ .

### 3.10.2 Donor Type Traps

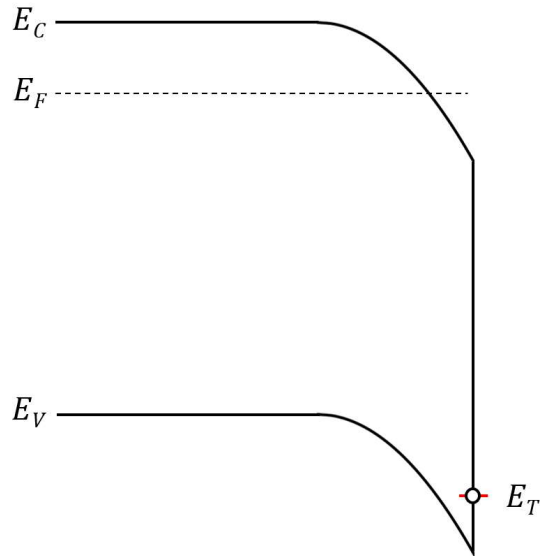


Figure 30: Energy band diagram for an n-type metal oxide with a shallow-hole acceptor trap and a trapped hole.

Adsorption can also occur with donor-like surface traps. These surface traps create a positive charge on the surface either by donating electrons directly to the conduction band or trapping holes from the valence band. An example of such an adsorbate is water. Experimental current measurements of ZnO in wet nitrogen show that the conductivity increases in wet nitrogen and decreases under illumination [55], [65]–[67], indicating that the water is creating a positive charge on the surface. The adsorption rate

equation for a hole trap is similar to that of the electron trap. The rate is the product of the rate constant,  $k_p$ , physically adsorbed concentration,  $P_t$ , and hole concentration at the surface:

$$\frac{dq_c}{dt} = k_p P_t p_b e^{-\frac{qV_s}{kT}} \quad (174)$$

where  $p_b$  is the bulk concentration of holes. The positive adsorbed charge creates an accumulation layer instead of a depletion layer. Thus, the relationship between the surface potential and the adsorbed concentration differs from (10) and (11). The full relationship between the surface charge and the surface potential is given by [68]:

$$q_c = \sqrt{\frac{2kT\epsilon_s}{q^2} \left( p_b \left( \exp\left(-\frac{qV_s}{kT}\right) + \frac{qV_s}{kT} - 1 \right) + n_b \left( \exp\left(\frac{qV_s}{kT}\right) - \frac{qV_s}{kT} - 1 \right) \right)} \quad (175)$$

In an n-type semiconductor with  $n_b \gg p_b$  in accumulation, the surface potential will be positive and (175) will simplify to:

$$q_c = \sqrt{b_p \left( \exp\left(\frac{qV_s}{kT}\right) - \frac{qV_s}{kT} - 1 \right)} \quad (176)$$

$$b_p = \frac{2kT\epsilon_s n_b}{q^2} \quad (177)$$

For  $q_c^2 \gg b_p$ , we can further simplify (175) and solve for the surface potential.

$$V_s = \frac{kT}{q} \ln\left(\frac{q^2 q_c^2}{2kT\epsilon_s n_b}\right) \quad (178)$$

However, in most metal oxide systems,  $n_b$  and therefore  $b_p$  are very large and (178) is not applicable.

Under illumination, the accumulation layer will separate holes and electrons. In this case, it is the electrons which will migrate to the surface to recombine with trapped electrons. The photodesorption equation then becomes:

$$\frac{dq_c}{dt} = k_p P_T p_b e^{-\frac{qV_s}{kT}} - L \quad (179)$$

### 3.10.3 Humidity

Humidity has a significant impact on the photoresponse of metal oxide photodetectors. To model the effect of humidity, we combine the oxygen and water adsorption equations into a system of differential equations:

$$\frac{dq_{c,n}}{dt} = k_n N_T n_b e^{\frac{qV_s}{kT}} \quad (180)$$

$$\frac{dq_{c,p}}{dt} = k_p P_T p_b e^{-\frac{qV_s}{kT}} \quad (181)$$

where  $q_{c,n}$  is the negative charge concentration from electrons trapped by oxygen, and  $q_{c,p}$  is positive charge concentration from holes trapped by water. In experimental measurements of metal oxide current in humid conditions where both oxygen and water are present, the dark conductivity of the samples decrease over time as with pure oxygen environments [69]. Therefore, we assume that the samples operate in the depletion region and the surface potential can be related to the surface charge by:

$$V_s = \frac{q(q_{c,n} - q_{c,p})^2}{2\epsilon_s n_b} \quad (182)$$

Table 5: Adsorption parameters for simultaneous oxygen and water adsorption shown in Figure 31.  $P_{Th}$  is the physically adsorbed water concentration under high humidity, and  $P_{Tl}$  is the physically adsorbed water concentration under low humidity.

$k_n$ ( $cm^3/s$ )	$N_T$ ( $cm^{-2}$ )	$n_b$ ( $cm^{-3}$ )	$k_p$ ( $cm^3/s$ )	$P_{Th}$ ( $cm^{-2}$ )	$P_{Tl}$ ( $cm^{-2}$ )	$p_b$ ( $cm^{-3}$ )
$1 \times 10^{-10}$	$1 \times 10^{15}$	$1 \times 10^{17}$	$1 \times 10^{-10}$	$1 \times 10^{15}$	$1 \times 10^{14}$	$1 \times 10^5$

Table 6: Device parameters for current calculations of simultaneous oxygen and water adsorption shown in Figure 31.

$\epsilon_r$	$V_a$ (V)	$\mu_n$ ( $cm^2/Vs$ )
8.4	1	100
$W$ (nm)	$d$ ( $\mu m$ )	$l$ ( $\mu m$ )
100	1	1

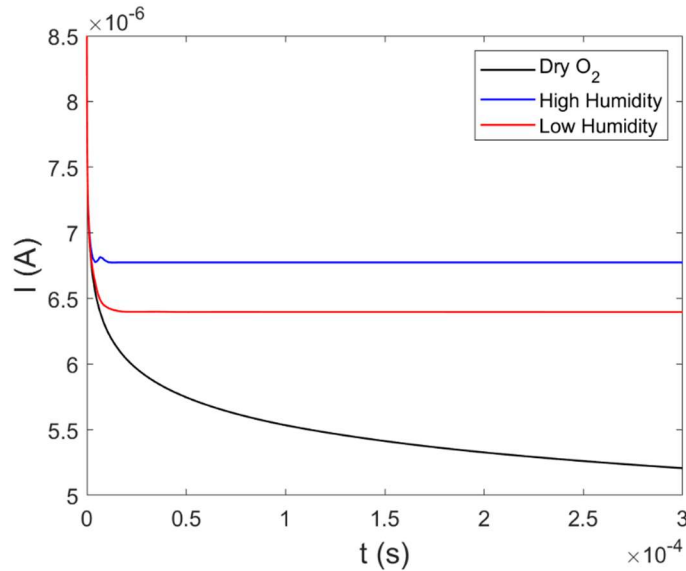


Figure 31: Current for device with parameters given by Table 6 under different humidity conditions. Current is calculated using (190). For dry oxygen, only (180) is used. For high humidity, both equation (180) and (181) are solved simultaneously with  $P_T = P_{Th}$ . For low humidity,  $P_T = P_{Tl}$ .

Figure 31 shows an example of current calculated for a typical ZnO thin film device under different humidity conditions. The change in humidity is modeled by a change in physically adsorbed

water concentration,  $P_T$ . The figure shows that net charge, and therefore the current, tends to saturate. In addition, the conductivity of the sample increases with increasing humidity. Both of these effects are due to the build-up of positive charge from the water molecules, and the steady-state net charge concentration is given by:

$$(q_{c,n} - q_{c,p}) = \sqrt{\frac{kT\epsilon_s n_b}{q^2} \ln\left(\frac{k_n N_T n_b}{k_p P_T p_b}\right)} \quad (183)$$

These trends are similar to those found in experimental measurement; the current in metal oxide samples does tend to increase and saturate with increasing humidity [69].

To determine the effect of illumination on a metal oxide photodetector with both oxygen and water adsorbates, we propose two possible mechanisms and compare their predicted photocurrent transients to experimental photocurrent transients. The first possible mechanism is that adsorbed water molecules act as recombination centers for photogenerated carriers. A similar mechanism has been proposed by Li et al. in [69]. Holes trapped by water recombine with photogenerated electrons at the surface, and then the photodesorbed water molecules re-adsorb with photogenerated holes. We represent this in our system of rate equations as:

$$\frac{dq_{c,n}}{dt} = k_n(N_T - q_{c,n})n_b e^{\frac{qV_s}{kT}} - (1 - \kappa_1)L \quad (184)$$

$$\frac{dq_{c,p}}{dt} = k_p(P_T - q_{c,p})p_b e^{-\frac{qV_s}{kT}} + \kappa_1 L - \kappa_2 L \quad (185)$$

where  $\kappa_1$  is the fraction of photogenerated holes that are trapped by water, and  $\kappa_2$  is the fraction of photogenerated electrons that recombine with trapped holes. Note that we do not include the photoadsorption term as an increase in the bulk concentration of holes (i.e., by adding  $\Delta p_b$  to the  $p_b$  term) because the rate of holes to the surface is determined by the photogeneration rate and not Boltzmann

statistics. The fraction of photogenerated holes trapped by the water molecules is likely a function of the physically and chemically adsorbed concentrations of both water and oxygen, and the local electric fields surrounding the adsorbed molecules. Here, we approximate that the fraction is proportional to the humidity and the ratio of oxygen molecules to water molecules:

$$\kappa_1 = \frac{P_T}{P_T + N_T} \quad (186)$$

This first-order approximation will ensure that the fraction of holes trapped by the water molecules increases with humidity. We arbitrarily set the fraction of captured electrons to

$$\kappa_2 = \kappa_1 \quad (187)$$

so that the adsorbed water molecules act as recombination centers and do not accumulate charge from photogenerated carriers. Figure 32(a) shows the photocurrent for a typical ZnO thin film under different humidity conditions using (184) and (185). The recombination of the photocarriers at the water traps effectively reduces the internal quantum efficiency of the device and decreases the photocurrent. This degradation of the photocurrent has been experimentally observed as shown in Figure 32(c). However, this model does not predict the increase in the adsorption rate with increasing humidity.

There is also some evidence that indicates that under the presence of oxygen, water may dissociate into hydrogen and hydroxyl groups [69], [70]. In this case, water could contribute both acceptor- and donor-type traps. In Section 3.10.1, we determined that multiple acceptor-like surface traps would increase the adsorption rate by changing the effective adsorption rate constant and physically adsorbed concentration. Thus, we replace (184) with (164) and write our system of rate equations as:

$$\frac{dq_{c,n}}{dt} = (k_{n,O_2}N_{T,O_2} + k_{n,H_2O}N_{T,H_2O})n_b e^{\frac{qV_s}{kT}} - L \quad (188)$$

$$\frac{dq_{c,p}}{dt} = k_p P_T p_b e^{-\frac{qV_s}{kT}} \quad (189)$$

where  $k_{n,O_2}$  is the adsorption rate constant for oxygen.  $N_{T,O_2}$  is the physically adsorbed oxygen concentration,  $k_{n,H_2O}$  is the adsorption rate constant for water, and  $N_{T,H_2O}$  is the physically adsorbed water concentration. The surface potential is still given by (182). To isolate the effect of the change in the adsorption rate, the only photogenerated carrier interaction we consider is the recombination of holes with trapped electrons.

**Table 7: Adsorption rate parameters for simultaneous oxygen and water adsorption with dissociated water molecules shown in Figure 32(b). The physically adsorbed donor-type water concentration,  $N_{T,H_2O}$ , is equal to the physically adsorbed donor-type water concentration,  $P_{Th}$  or  $P_{Tl}$ .**

$k_{n,O_2} (cm^3/s)$	$N_{T,O_2} (cm^{-2})$	$n_b (cm^{-3})$
$1 \times 10^{-11}$	$1 \times 10^{15}$	$1 \times 10^{17}$
$k_{n,H_2O} (cm^3/s)$	$N_{T,H_2O} (cm^{-2})$	$p_b (cm^{-3})$
$1 \times 10^{-10}$	$P_t$	$1 \times 10^5$
$k_p (cm^3/s)$	$P_{Th} (cm^{-2})$	$P_{Tl} (cm^{-2})$
$1 \times 10^{-10}$	$1 \times 10^{15}$	$1 \times 10^{14}$

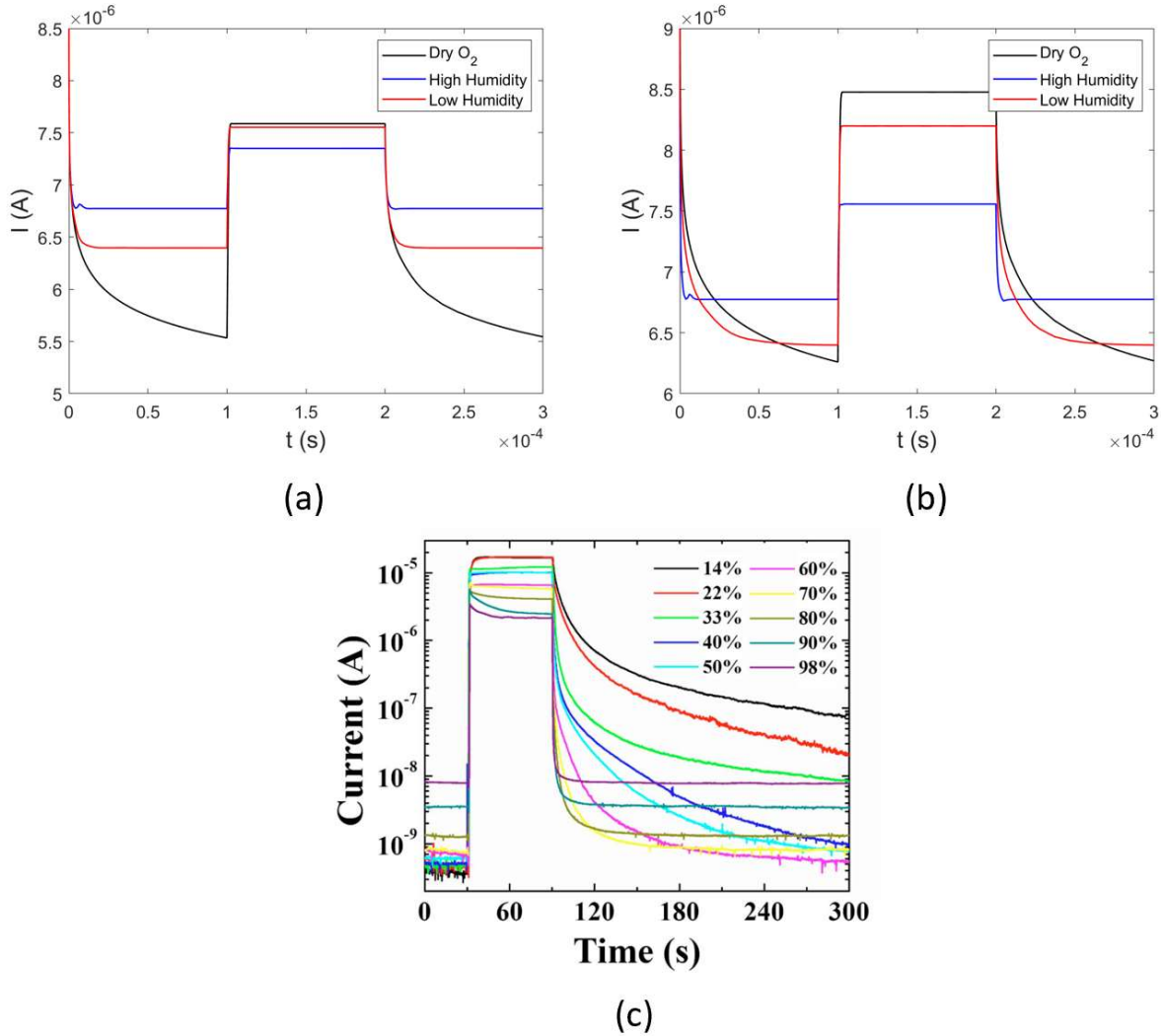


Figure 32: Photocurrent under different humidity conditions. For (a) and (b), photocurrent for dry  $O_2$  is calculated using (180), Table 6, and oxygen adsorption rate parameters in Table 7. For all transients in (a) and (b),  $\lambda = 340\text{nm}$  and  $I_{\text{opt}} = 60\text{mW}/\text{cm}^2$ . (a) Photocurrent for low and high humidity calculated using (184), (185), Table 6, and Table 7. (b) Photocurrent for low and high humidity calculated using (188), (189), Table 6, and Table 7. (c) Experimental measurements of ZnO nanowire photocurrent transients under different relative humidity conditions. Reprinted with permission from Y. Li, F. Della Valle, M. Simonnet, I. Yamada, and J.-J. Delaunay, "Competitive surface effects of oxygen and water on UV photoresponse of ZnO nanowires," *Appl. Phys. Lett.*, vol. 94, no. 2, Jan. 2009, Art. no. 023110, Copyright 2009 AIP, [69].

Figure 32(b) shows the calculated current for a sample in which the water molecules act as both hole and electron traps. The dark current under humid conditions is still larger than that in dry conditions, and the dark current still saturates according to (183) but with a different effective rate constant. Under illumination, the photocurrent decreases with increasing humidity. This is due to the increase in the effective adsorption rate constant which increases the steady-state illuminated surface potential. The

photodecay transients show that the adsorption rate increases for increasing humidity. These phenomena are consistent with experimental measurements shown in Figure 32(c).

It may be that the actual photoresponse is some combination of these effects. There may also be other effects, such as chemical reactions between the water and oxygen, that effect the photoresponse. More experimental studies are needed to determine the actual form of the adsorption rate equations.

### 3.11 Photocurrent

#### 3.11.1 General Case

The primary effect of illumination is a change of the depletion width. We will first examine the current for a single, planar crystal with ohmic contacts as shown in Figure 33. In this configuration, current flows parallel to the adsorption surface.

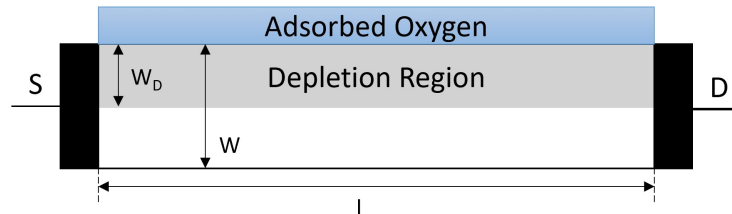


**Figure 33: Geometry of sample analyzed in this section. Not shown is the depth ‘d’ into the page. ‘S’ is source contact, ‘D’ is drain contact.**

We can then divide the sample into two regions: bulk and depletion. The bulk will have a much higher conductivity than the depletion region, and the adsorbed concentration will modulate the widths of the two regions. Thus, over time, the increasing adsorbed concentration will increase the depletion width and reduce the overall conductance of the sample. The sample conductance is given by:

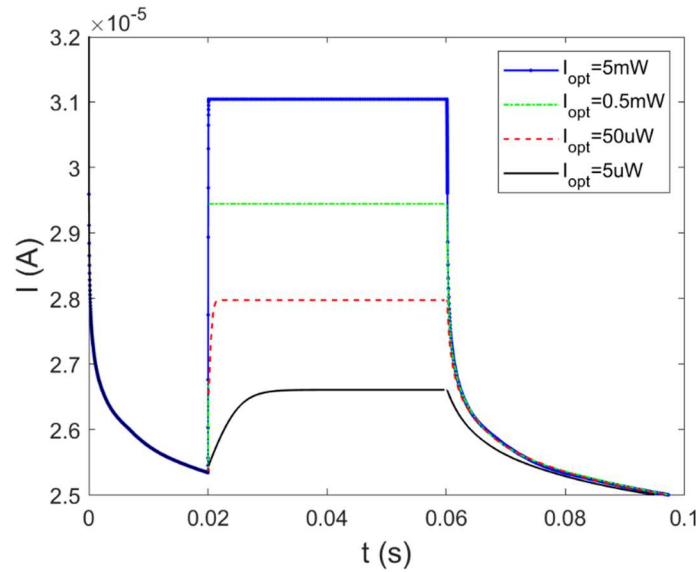
$$G_B = \frac{q\mu_n n_b d(W - W_D)}{l} \quad (190)$$

Figure 34 shows some example photocurrent transients for the PD device with parameters given in Table 8. The plot shows that the current rises linearly with illumination and reaches a saturation value.

When the illumination is removed, the photocurrent shows a fast transient followed by a slow transient. The rate of decay is also proportional to the magnitude of the photocurrent.

**Table 8: Photocurrent calculation parameters for Figure 34.**

$k_n$ ( $cm^{-2}$ )	$N_t$ ( $cm^{-2}$ )	$n_b$ ( $cm^{-3}$ )	$\mu_n$ ( $cm^2/Vs$ )	$\epsilon_r$	$q_c(0)$ ( $cm^{-2}$ )	$d$ ( $\mu m$ )	$l$ ( $\mu m$ )	$W$ ( $nm$ )
$1 \times 10^{-11}$	$1 \times 10^{15}$	$1 \times 10^{17}$	200	8.4	0	1	1	150



**Figure 34: Photocurrent transients for different illumination intensities using the device parameters given by Table 8.**

In the completely depleted case, the depletion approximation cannot be used. Instead we calculate the conductivity through the exact form of the electron concentration:

$$n(x) = N_D \exp\left(\frac{q}{kT} \left(-\frac{qN_D}{2\epsilon} x^2 - \frac{qN_D(W_D - W)}{\epsilon} x + V_{bg}\right)\right) \quad (191)$$

Then, the average conductivity is given by:

$$\bar{\sigma}_d = \frac{q\mu_n N_D}{W} \frac{\sqrt{\pi} e^{\frac{b^2}{4a} + c}}{2\sqrt{a}} \left( \operatorname{erf}\left(\frac{2aW + b}{2\sqrt{a}}\right) - \operatorname{erf}\left(\frac{b}{2\sqrt{a}}\right) \right) \quad (192)$$

$$a = \frac{q^2 N_D}{2kT\epsilon} \quad (193)$$

$$b = \frac{q^2 N_D \left( \frac{q_c}{N_D} - W \right)}{kT\epsilon} \quad (194)$$

$$c = - \frac{q^2 N_D \alpha \left( \frac{q_c}{N_D} - W \right)}{kT\epsilon} \quad (195)$$

And the conductivity is:

$$G_D = \frac{dW \bar{\sigma}_d}{l} \quad (196)$$

### 3.11.2 Back Gate Capacitance

When the metal oxide has an oxide substrate and a back gate, the boundary conditions of Poisson's equation are modified as discussed in the section 'Completely Depleted Case.' This changes the electron distribution in the metal oxide such that some of the counteracting positive charge is placed on the back gate. From conservation laws, any positive charge added to the metal back gate must be compensated by the addition of electrons to the metal oxide. Thus, an 'injection' electron current appears during adsorption, and an 'ejection' current appears during illumination even with zero bias applied. In other words, a metal-oxide-semiconductor capacitor is formed across which a portion of the surface potential is applied. This current may be relatively small compared to the normal conduction current, and its magnitude is strongly dependent on device geometry, back gate bias, and the frequency of illumination.

In the completely depleted case, the voltage across the oxide is given by:

$$V_{ox} = \frac{t_{ox} q N_D}{\epsilon} \left( \frac{q_c}{N_D} - W \right) \quad (197)$$

Thus, the current that must be supplied into the metal oxide to compensate this voltage drop, which we will call the injection current  $I_{inj}$ , is given by:

$$I_{inj} = C_{ox} \frac{dV_{ox}}{dt} \quad (198)$$

$$= C_{ox} \frac{t_{ox}}{\epsilon} q \frac{dq_c}{dt} \quad (199)$$

$$= \frac{\epsilon dl t_{ox}}{t_{ox} \epsilon} q \frac{dq_c}{dt} \quad (200)$$

$$= dlq \frac{dq_c}{dt} \quad (201)$$

$$I_{inj} = dlq k_n N_t n_b \exp\left(\frac{q\phi_s}{kT}\right) \quad (202)$$

The current is referred to as an injection current because electrons are injected from both contacts, source and drain, of the device. Thus, the actual current at the source or drain at 0V bias is actually  $I_{inj}/2$  and will vary with bias.

Under illumination, the electrons that were provided by the injection current for adsorption must now be removed as the surface potential and therefore  $V_{ox}$  decreases. We can follow the same arguments as above but use the rate of change of chemisorbed concentration as given in (103). Additionally, we must consider that electrons are ejected from the sample in this case. Thus, this current is referred to as the Ejection Current,  $I_{ejx}$  and is given by:

$$I_{ejx} = dlq \left( k_n N_t N_D e^{\frac{q}{kT}\phi_s} - \frac{G_L(0)}{\alpha} (1 - e^{-\alpha W}) \right) \quad (203)$$

## 4. PERFORMANCE METRICS AND DESIGN CONSIDERATIONS

Photodetectors are usually characterized in terms of their photocurrent and photoresponsivity. However, here we make the argument that these are not good metrics of photoconductor performance. We do this by examining the signal and signal-to-noise ratio of photoconductors in practical application circuits.

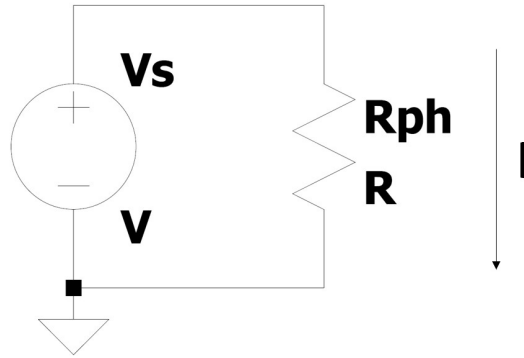


Figure 35: Photoconductor diagram.

We first consider the SNR of a photoconductor as it is traditionally analyzed [71]. The signal of a photoconductor, shown in Figure 35, is generally given by the AC photocurrent. For now, we consider the device to be operated at a frequency such that the amplitude of the AC photocurrent to be determined by the difference between the on-current and the dark current. We will discuss AC currents whose minimum value is not the dark current later. In this case, the magnitude of the RMS photocurrent is defined as:

$$i_{ph} = \frac{I_{on} - I_d}{\sqrt{2}} \quad (204)$$

$$= \frac{V_s}{\sqrt{2}} \left( \frac{1}{R_{phl}} - \frac{1}{R_{phd}} \right) \quad (205)$$

where  $I_{on}$  is the DC current under illumination,  $I_d$  is the dark current,  $R_{phl}$  is the resistance under illumination, and  $R_{phd}$  is the resistance in the dark. The noise is measured as the current noise and is

divided into three components: thermal/Johnson noise, flicker noise, and generation-recombination noise.

The RMS thermal noise current in units of A is given by:

$$i_j = \sqrt{\frac{4kTB}{R_{phd}}} \quad (206)$$

where B is the device bandwidth. The generation-recombination current is given by:

$$i_{GR} = \sqrt{\frac{4q\Gamma_G I_{on} B}{1 + \omega^2 \tau^2}} \quad (207)$$

$$= \sqrt{\frac{4q\Gamma_G \left(\frac{V_s}{R_{ph,l}}\right) B}{1 + \omega^2 \tau^2}} \quad (208)$$

where  $\Gamma_G$  is the photoconductive gain,  $\omega$  is the operating frequency,  $\tau$  is the recombination lifetime.

Usually, the flicker noise is ignored since it is negligible at practical operating frequencies. The power

SNR is given as the ratio of the power associated with the photocurrent and the noise:

$$SNR_R = \frac{i_{ph}^2}{i_j^2 + i_{GR}^2} \quad (209)$$

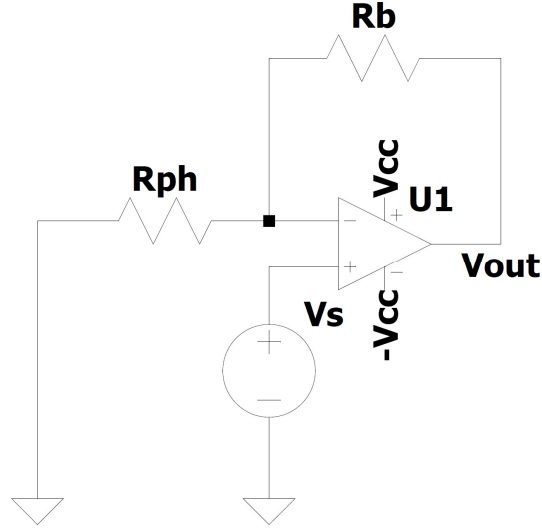


Figure 36: TIA circuit.

The typical circuit used with photodetectors is a transimpedance amplifier (TIA) circuit shown in Figure 36. Here we derive the SNR for the TIA to compare with (209). The RMS photovoltage signal is given by:

$$V_{ph,TIA} = \frac{V_s R_b}{\sqrt{2}} \left( \frac{1}{R_{ph,l}} - \frac{1}{R_{ph,d}} \right) \quad (210)$$

The noise in the circuit has 3 contributions: op-amp voltage noise, op-amp current noise, and biasing resistor thermal noise. Assuming that we are operating at a high enough frequency such that thermal noise is dominant over R-G noise, the RMS thermal noise is given by:

$$i_{j,TIA} = \sqrt{4kTR_{eq}B_c} \quad (211)$$

$$R_{eq} = \frac{R_{ph}R_b}{R_{ph} + R_b} \quad (212)$$

where  $B_c$  is the closed-loop bandwidth of the op-amp given by:

$$B_c = K \frac{B_0}{G} \quad (213)$$

$$G = \frac{R_{ph}}{R_b} + 1 \quad (214)$$

where  $K$  is the brick-wall filter correction factor,  $B_0$  is the unity-gain bandwidth, and  $G$  is the closed-loop gain. The closed-loop gain and the equivalent resistance given in (212) may be determined either by the dark resistance or the illuminated resistance. That is, the noise may be larger in the dark or in the light. Generally, the noise is largest for  $R_{ph,d}$ . However, the op-amp flicker noise may be larger for  $R_{ph,l}$ . When calculating the noise then, we must take the greater of the two. Here we assume that the noise will be greater for  $R_{ph,d}$  and use that in the remainder of our calculations. We also assume the op-amp has a first-order roll-off characteristic of the op-amp so that  $K = 1.57$ .

The voltage noise has two components: broadband noise and flicker noise. The broadband voltage noise is

$$V_{n,BB} = v_{n,BB} \sqrt{B_c} \quad (215)$$

where  $v_{n,BB}$  is the voltage noise density. The flicker noise is given by:

$$V_{n,f} = v_{n,f} \sqrt{f_0 \ln\left(\frac{B_c}{f_L}\right)} \quad (216)$$

where  $v_{n,f}$  is the voltage noise density at the frequency  $f_0$ , and  $f_L$  is the low cut-off frequency, usually around  $\sim 0.1$  Hz in most practical applications. The current noise in the op amp is broadband noise and is given by:

$$V_{n,i} = i_{BB} R_{eq} \sqrt{B_c} \quad (217)$$

The total noise is then:

$$V_{n,TIA} = G \sqrt{4kTR_{eq}B_c + V_{n,BB}^2 + V_{n,f}^2 + V_{n,i}^2} \quad (218)$$

The SNR is given by:

$$SNR = \frac{V_{ph,TIA}^2}{V_{n,TIA}^2} \quad (219)$$

From (219), we can see that the SNR is increased as  $R_b$  is increased due to the increase in gain. However, the gain can only be increased until the signal reaches saturation. The optimal  $R_b$  is then:

$$R_b = R_{phl} \left( \frac{V_{cc}}{V_s} - 1 \right) \quad (220)$$

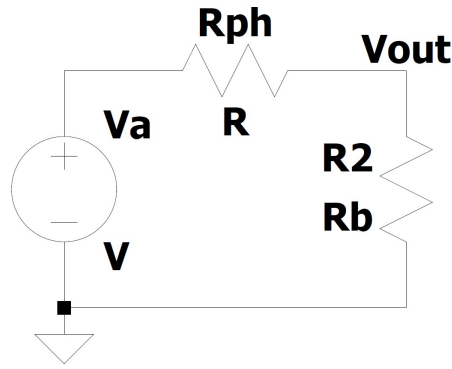


Figure 37: Voltage divider circuit for photodetector.

Voltage dividers are more commonly used in resistive sensor systems. Here we will derive the SNR for the voltage divider circuit shown in Figure 37. The photovoltage signal is given by

$$V_{ph,VD} = \frac{V_a}{\sqrt{2}} \left( \frac{R_b}{R_b + R_{phl}} - \frac{R_b}{R_b + R_{phd}} \right) \quad (221)$$

For now, we will assume that we are operating at a frequency where the thermal noise is dominant. The RMS noise is given by:

$$V_{n,VD} = \sqrt{4kTR_{eq}B} \quad (222)$$

Then, the power SNR is:

$$SNR_{VD} = \frac{V_{ph,VD}^2}{V_{n,VD}^2} \quad (223)$$

We can optimize this SNR by taking the derivative of (223) with respect to  $R_b$ , setting it equal to 0, and solving for the optimal bias resistance,  $R_{b,SNR}$ :

$$R_{b,SNR} = \frac{1}{4} \left( \sqrt{8R_{phl}R_{phd} + R_{phd}^2} - R_{phd} \right) \quad (224)$$

We can now compare the SNR values of these 3 circuits. To do this, we set all circuits to have the same bandwidth and power consumption. To control for the effect of applied voltage on the SNR, we set the supply voltages such that all circuits have the same average power consumption. The average power dissipated for the resistor is:

$$P_{avg,R} = \frac{1}{2} V_s^2 \left( \frac{1}{R_{phl}} + \frac{1}{R_{phd}} \right) \quad (225)$$

The average power for the TIA is:

$$P_{TIA} = \frac{V_s^2}{2} \left( \frac{1}{R_{phl}} + \frac{1}{R_{phd}} \right) + V_{cc} I_Q \quad (226)$$

where  $I_Q$  is the quiescent current. Finally, the voltage divider average power consumption is:

$$P_{avg,VD} = \frac{1}{2} V_a^2 \left( \frac{1}{R_{phl} + R_{b,SNR}} + \frac{1}{R_{phd} + R_{b,SNR}} \right) \quad (227)$$

Figure 38 shows the SNR as a function of the dark resistance for the three circuits using the parameters in Table 9. The SNR, power dissipation, and bandwidth for the TIA is calculated first using the optimized biasing resistor given by (220). The power dissipation is then used to calculate the biasing voltage for the other two circuits, and the closed-loop bandwidth calculated from the TIA is used to calculate the thermal noise for the voltage divider and the resistor. The voltage divider uses the optimized biasing resistor given by (229).

**Table 9: Photoconductor and OPA627 Op-amp parameters [72] for calculations in Table 9.**

$R_{phl} (\Omega)$	$V_{cc} (V)$	$V_{s,TIA} (V)$	$B_0 (MHz)$	$v_{n,BB} (nV/\sqrt{Hz})$	$v_{n,f} (nV/\sqrt{Hz})$
10	20	10	16	5	50
$f_0 (Hz)$		$I_Q (mA)$		$i_{BB} (fA/\sqrt{Hz})$	
1		7		16	

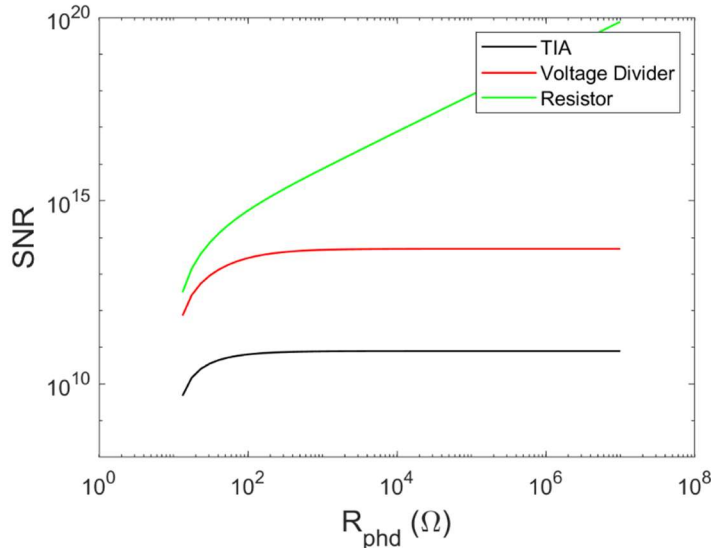


**Figure 38: SNR for parameters shown in Table 9.**

The plot shows that the SNR of both the voltage divider and the TIA differ significantly from that of the resistor. This is because the dark resistance contributes significantly to the voltage noise in both systems, and an increase in the dark resistance will increase the noise through (217) and (222). This means that (209) is not a good representation of the actual SNR in a practical application, and the dark current is not a good metric for characterizing the noise in photoconductors. Note that the SNR values are very large because the resistor noise is very small. For a  $10\Omega$  resistor with a 16MHz bandwidth, the noise current amplitude from (206) is 163nA. This is very small compared to the photocurrent signal. Note that the flicker noise and R-G noise are not considered in Figure 38, and the inclusion of these terms would further decrease the SNR. We have not included these terms because the purpose of the plot is to show that the traditional method of analyzing photoconductor noise deviates significantly from that seen in actual photodetector application circuits.

Figure 38 also shows that the voltage divider circuit outperforms the TIA at every point. Figure 39 shows the TIA compared to the voltage divider for different values of  $R_{phl}$ . Figure 39 (a) shows the case for an ideal op-amp with no noise or power dissipation. The voltage divider outperforms the op-amp except for values of  $R_{phd}$  close to  $R_{phl}$ , however this is only a slight deviation. Figure 39 (b) is the same plot but with a real op-amp. Here we use a relatively low-noise op-amp. The voltage divider outperforms the TIA at every value of  $R_{phd}$ , and outperforms the TIA by several orders of magnitude in some cases. Figure 40 compares the performance between the two circuits as a function of the other two degrees of freedom: the supply voltages. In all cases, the voltage divider outperforms the TIA. The TIA has several other disadvantages. In the cases shown in Figure 39, the signal is operating at the saturation value of the op-amp. For many op-amps, the signal will be degraded close to the saturation value. In addition, since the device is operating at saturation, any increase in the input power (decrease in  $R_{phl}$ ) will not increase the signal and will degrade the SNR. Finally, the power dissipated by the photoconductor is higher in the TIA, which may lead to significant heating which will increase thermal noise and could degrade the photoresponse.

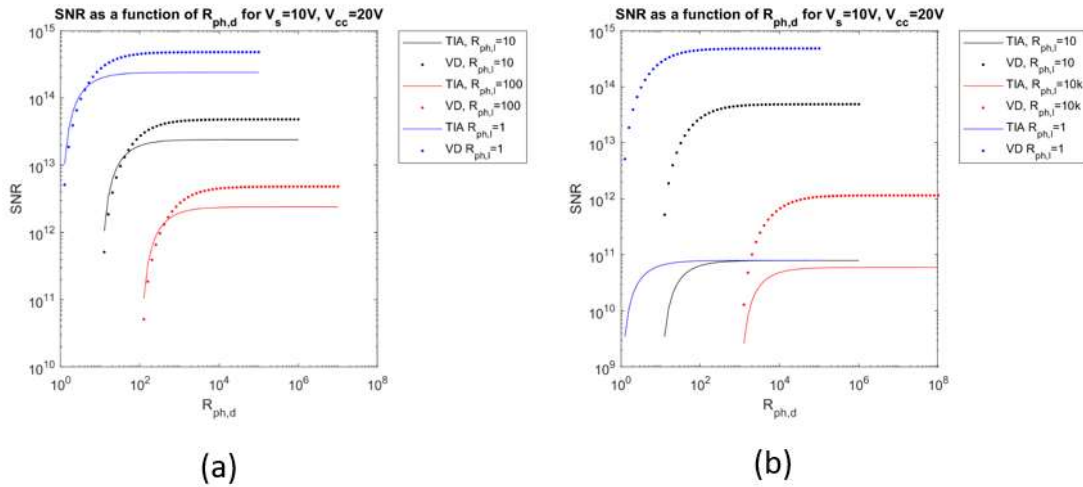
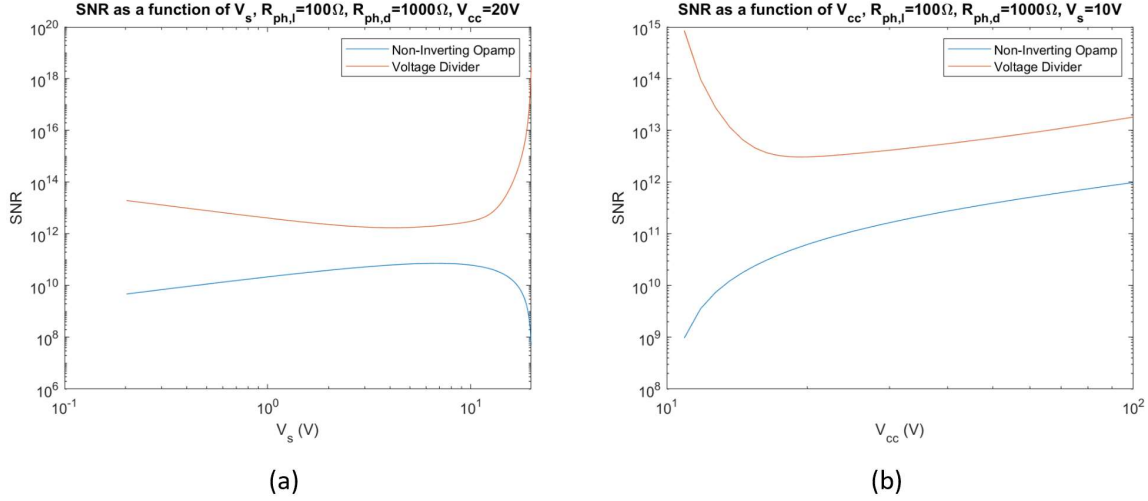


Figure 39: (a) SNR for TIA with ideal op-amp compared to voltage divider (VD); (b) SNR for TIA with op-amp parameters given in Table 9 compared to VD.



**Figure 40:** (a) SNR as a function of  $V_s$  for  $R_{phl} = 100\Omega$ ,  $R_{phd} = 1k\Omega$ ,  $V_{cc} = 20V$ , and  $B_0 = 16MHz$ ,  $v_{n,BB} = 5nV/\sqrt{Hz}$ ,  $v_{n,f} = 50nV/\sqrt{Hz}$ ,  $i_{BB} = 1.6fA/\sqrt{Hz}$  at  $f_0 = 1Hz$ ,  $I_Q = 7mA$  (b) SNR as a function of  $V_{cc}$  for  $R_{phl} = 100\Omega$ ,  $R_{phd} = 1k\Omega$ ,  $V_s = 10V$ , and  $B_0 = 16MHz$ ,  $v_{n,BB} = 5nV/\sqrt{Hz}$ ,  $v_{n,f} = 50nV/\sqrt{Hz}$ ,  $i_{BB} = 1.6fA/\sqrt{Hz}$  at  $f_0 = 1Hz$ ,  $I_Q = 7mA$ .

The voltage divider is clearly the best circuit for optimizing the SNR of photoconductor circuits. However, the photoresponsivity does not characterize the performance of the voltage divider circuit. Figure 41 shows a plot of the voltage divider SNR vs the ratio of the dark resistance to the illuminated resistance for two circuits: one with  $R_{phl} = 10\Omega$  and the other with  $R_{phl} = 100\Omega$ . Both are in series with a resistor optimized for the SNR as given by (224), and both consume a power of 1mW and have a bandwidth of 1GHz. The plot shows that for SNR normalized to power consumption and bandwidth, the SNR depends only on the ratio of the dark to the illuminated resistance. Therefore, we will use the resistive gain to characterize photoconductor performance. Additionally, we redefine the photoresponsivity in terms of the photovoltage produced by the voltage divider circuit:

$$\mathcal{R}_v \equiv \frac{V_{ph,VD}}{I_{opt}} \quad (228)$$

This metric captures the effect of applied voltage and illumination intensity on the photodetector signal. Although applied voltage can increase the SNR, it also increases the current which can cause heating and change, for example, the carrier concentration and therefore the output signal. Instead of normalizing to optical power as is done with the current photoresponsivity metric, we normalize to illumination intensity.

This is because the resistive gain is a function of the illumination intensity and does not change as a function of device area (assuming the entire device area is uniformly illuminated). If we were to normalize to  $P_{opt}$ ,  $\mathcal{R}_v$  could be arbitrarily increased by decreasing the device area even though the resistive gain would remain the same.

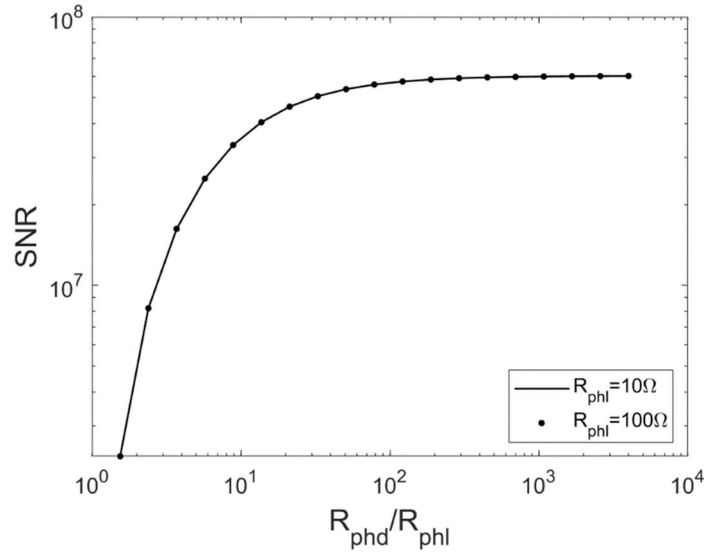


Figure 41: SNR for voltage divider with 1mW of power consumption and B = 1GHz.

Metal oxides also differ from traditional photodetectors in that they do not have a single dark current (or in this case, resistance) value. We have already shown that adsorption is a very slow process, thus the dark resistance can change over a very long time. Therefore, selection of the ‘dark resistance’ must be coupled with a recovery time measurement. This will be discussed in more detail in Section 4.2.

#### 4.1 Resistive and Photoconductive Gain

The resistive gain is given by the ratio of the resistance in the dark to the resistance under illumination:

$$G_R = \frac{R_{phd}}{R_{phl}} \quad (229)$$

In PD planar devices, this equation can be simplified. Assuming the depletion approximation, (229) simplifies to:

$$G_R = \frac{W - W_{D,l}}{W - W_{D,d}} \quad (230)$$

where  $W_{D,l}$  is the depletion width under illumination and  $W_{D,d}$  is the depletion width in the dark. Figure 42 shows a plot of the resistive gain and dark resistance as a function of device width for a planar device with parameters given by Table 1 and Table 10. The illuminated depletion width is calculated from the illuminated steady-state adsorbed concentration given by (78). The plot shows that the gain increases as the device width approaches  $W_{D,d}$  and the device approaches complete depletion. However, the resistance in the dark also increases. Although the dark resistance does not affect the resistive gain, it will affect the noise and the output impedance of the voltage divider circuit. In applications, the voltage divider will be probed directly by an oscilloscope or have buffer stage after it. Generally, the scope or the buffer have a large but finite impedance of about  $1M\Omega$  to  $1G\Omega$ . The dark resistance must be smaller than this input impedance to ensure the signal is not degraded. Additionally, there will be some input current noise from a buffering op amp which will flow through the photoconductor. The voltage noise generated from this will be proportional to the dark resistance. Therefore, while the largest resistive gain is achieved for  $W = W_{D,d}$ , for practical applications the device cannot operate with this geometry.

**Table 10: Device parameters for calculation in Figure 42. The value  $q_{c,d}$  is the adsorbed concentration in the dark.**

$q_{c,d} (cm^{-2})$	$I_{opt} (W/cm^2)$	$\mu_n (cm^2/Vs)$	$l (cm)$	$d (cm)$	$\alpha (cm^{-1})$
$7 \times 10^{11}$	1	200	$1 \times 10^{-4}$	$1 \times 10^{-3}$	$1.414 \times 10^5$

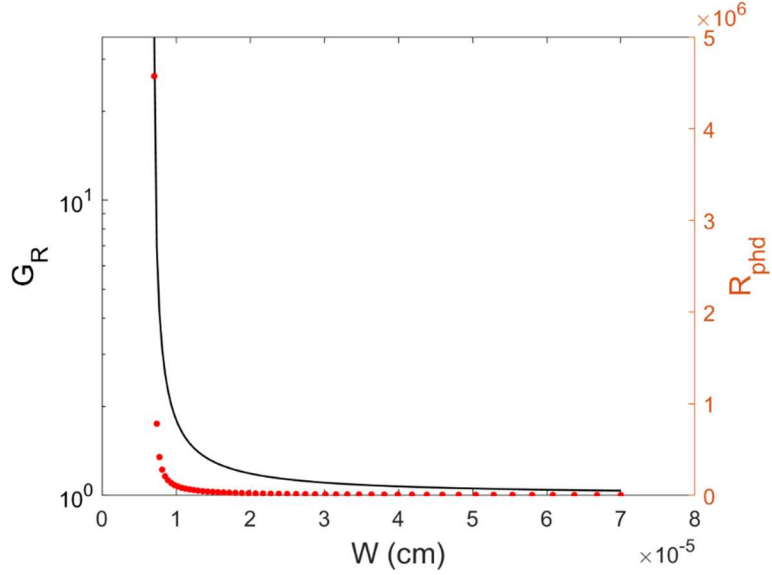


**Figure 42: Resistive gain and dark resistance as a function of device width for a device with parameters given by Table 1 and Table 10.**

One method of achieving high gain with lower resistance values is to employ a completely depleted device geometry. Figure 43 shows the gain and the dark resistance as a function of oxide thickness for the parameters given by Table 1 and Table 10. To ensure the device is well within the CD mode of operation is the dark, we set the width of each device to be slightly smaller than depletion width of the device after 1 second of adsorption with an initial condition of  $q_c(0) = 0$ . That is:

$$W = 0.98 * \frac{q_c(t = 1)}{n_b}, \quad q_c(0) = 0 \quad (231)$$

The plot shows that as the oxide thickness decreases, both the gain and the dark resistance decrease. This is because the CD device geometry enables some of the adsorbing electrons to come from the metal back gate rather than the semiconductor, leaving charge for conduction in the channel while adsorption continues. As the oxide thickness decreases, more charge is placed on the back gate, increasing the semiconductor conductance.

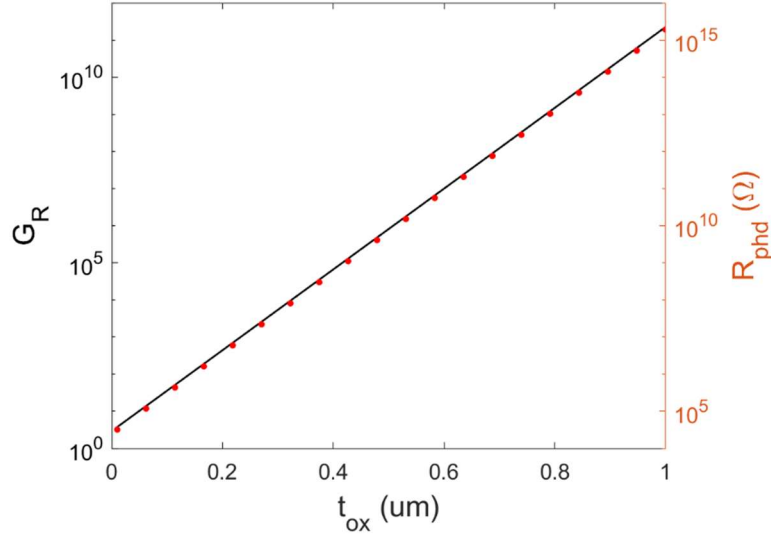


Figure 43: Gain and dark current for device with width  $W = 68.6\text{nm}$  and parameters given by Table 1 and Table 10.

To determine the effect of carrier concentration on the gain, we calculate the gain for several PD devices. The adsorbed concentration is set to an initial value of 0 in each case. Then, the adsorbed concentration after 1 second is calculated and the corresponding depletion width is calculated. This depletion width is the dark depletion width,  $W_{D,d}$ . Then, the steady-state depletion width under illumination,  $W_{D,i}$  is calculated. The semiconductor thickness is set to  $W = W_{D,d}$  to maximize the resistive gain. Because this would result in an infinite gain, we calculate the ratio of the gains to compare them. The reference gain,  $G_{R0}$ , is arbitrarily chosen as the gain for  $n_b = 1 \times 10^{14}\text{cm}^{-3}$ . The ratio of the gain is then calculated as:

$$\frac{G_R}{G_{R0}} = \frac{W - W_{D,i}}{W_{R0} - W_{D,i0}} \quad (232)$$

where  $W_{R0}$  is the width of the reference device and  $W_{D,i0}$  is the illuminated depletion width of the reference device. The results are shown in Figure 44(a). For PD devices, the gain decreases with increasing carrier concentration. The reason for this is demonstrated in Figure 44(b) which shows the depletion width relative to a reference depletion width,  $W_{D0}$ . The reference depletion width is set to the depletion width in a PD device for  $n_b = 1 \times 10^{14}\text{cm}^{-3}$  after 1 second. The depletion widths for the other

devices are calculated after 1 second as well. The plot shows that the depletion width decreases with carrier concentration. The ratio between the depletion widths can be modeled approximately as:

$$\frac{W(n_b)}{W(n_{b0})} \approx 3.1 \log\left(\frac{n_b}{n_{b0}}\right) \quad (233)$$

where  $n_{b0}$  is the reference carrier concentration. Thus, the gain increases with decreasing carrier concentration because the change in the depletion width is much larger.

**Table 11: Device parameters for Figure 44. The adsorbed concentration in the dark is the adsorbed concentration after 1 second for an initial concentration of 0. The device width is the depletion width corresponding to the adsorbed concentration in the dark.**

$k_n$ ( $cm^3/s$ )	$N_T$ ( $cm^{-2}$ )	$I_{opt}$ ( $W/cm^2$ )	$q_{c,d}$ ( $cm^{-2}$ )	$W$ ( $cm$ )	$\epsilon_r$	$\alpha$ ( $cm^{-1}$ )
$1 \times 10^{-10}$	$1 \times 10^{15}$	1	$q_c(t = 1)$	$q_{c,d}/n_b$	8.4	$1.414 \times 10^5$

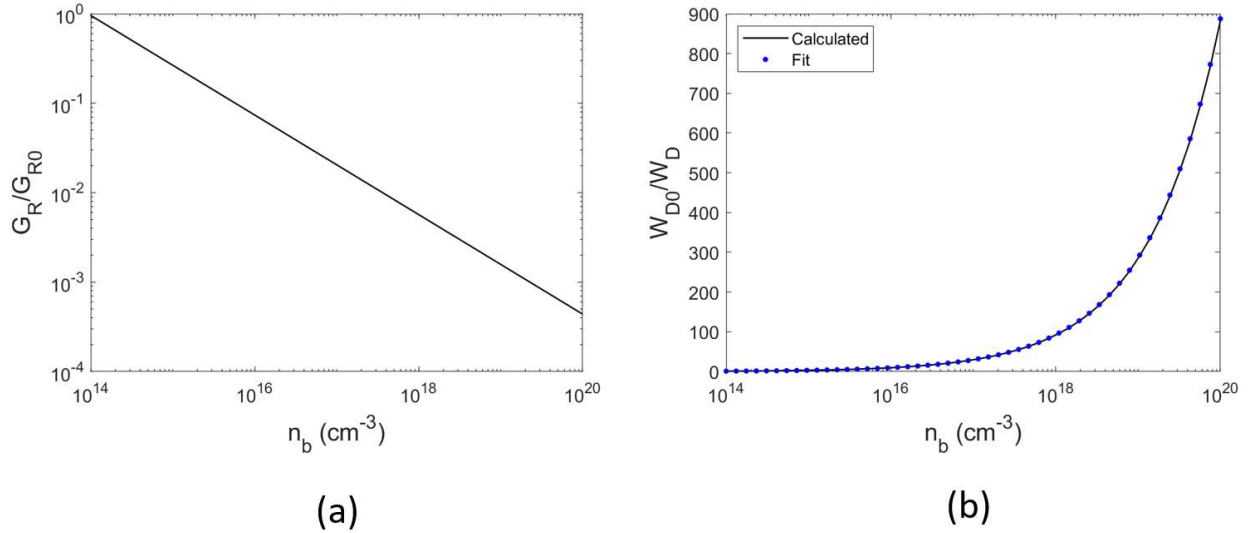


**Figure 44: (a) Gain relative to the reference gain at  $n_b = 1 \times 10^{14} cm^{-3}$ ; (b) Depletion width relative to the reference depletion width for  $n_b = 1 \times 10^{14} cm^{-3}$ , fit is calculated with (233); Both plots calculated using parameters in Table 11.**

The dependence of gain on carrier concentration in the CD case is different from the PD case. To compare the gains in CD devices with different carrier concentrations, we use the parameters in Table 12. Then, the dark resistance is calculated as the resistance in the device after 1 second of adsorption with an initial condition of  $q_c(0) = 0$ . The illuminated resistance is calculated as the resistance for the

illuminated steady-state adsorbed concentration. The width of the device is adjusted to ensure operation in complete depletion in the dark.

**Table 12: Device parameters for Figure 45. The adsorbed concentration in the dark is the adsorbed concentration after 1 second for an initial concentration of 0. The device width is the depletion width corresponding to the adsorbed concentration in the dark.**

$k_n$ ( $cm^3/s$ )	$N_t$ ( $cm^{-2}$ )	$I_{opt}$ ( $W/cm^2$ )	$q_{c,d}$ ( $cm^{-2}$ )	$W$ ( $cm$ )	$\epsilon_r$	$\alpha$ ( $cm^{-1}$ )
$1 \times 10^{-10}$	$1 \times 10^{15}$	1	$q_c(t = 1)$	$0.98(q_{c,d}/n_b)$	8.4	$1.414 \times 10^5$

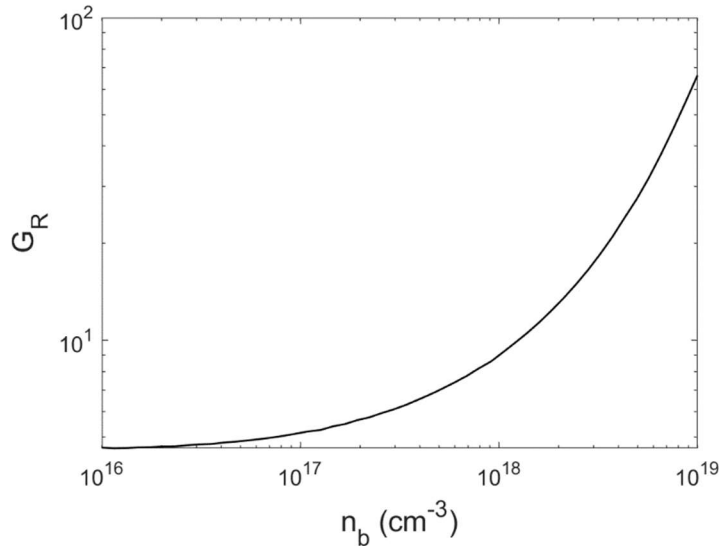


**Figure 45: Gain as a function of carrier concentration for CD case with parameters given by Table 12 and  $t_{ox} = 100nm$ .**

Figure 45 shows that for the CD case, the gain increases with increasing carrier concentration. This is because in CD the dark resistance increases much faster for larger carrier concentrations. This also means that the dark resistance will be much larger, so the tradeoff between dark resistance and gain will need to be considered carefully in device design.

The effect of dielectric permittivity on the gain is calculated for the PD case using Table 1 and Table 10. The device width is set to twice the dark depletion width to ensure the device remains in PD. For the CD case, the parameters in Table 12 are used. The dielectric permittivity is varied within the range of metal oxides commonly used in UV photodetectors [73]–[84]. The plots are shown in Figure 46.

The relative dielectric permittivity has a small effect on the gain within the given range. It increases somewhat in the CD case, and potentially for special materials with very high dielectric permittivity there would be a significant increase in gain. A plot of the gain vs the adsorption constant is constructed with the same devices and is shown in Figure 46. The range of adsorption rate constants is somewhat arbitrary since they have not been characterized for most metal oxides. However, within a large range of  $k_n$  there is very small change in gain for both cases. The number of traps,  $N_T$ , will have a similar effect on gain as the adsorption rate constant, so it is not plotted here.

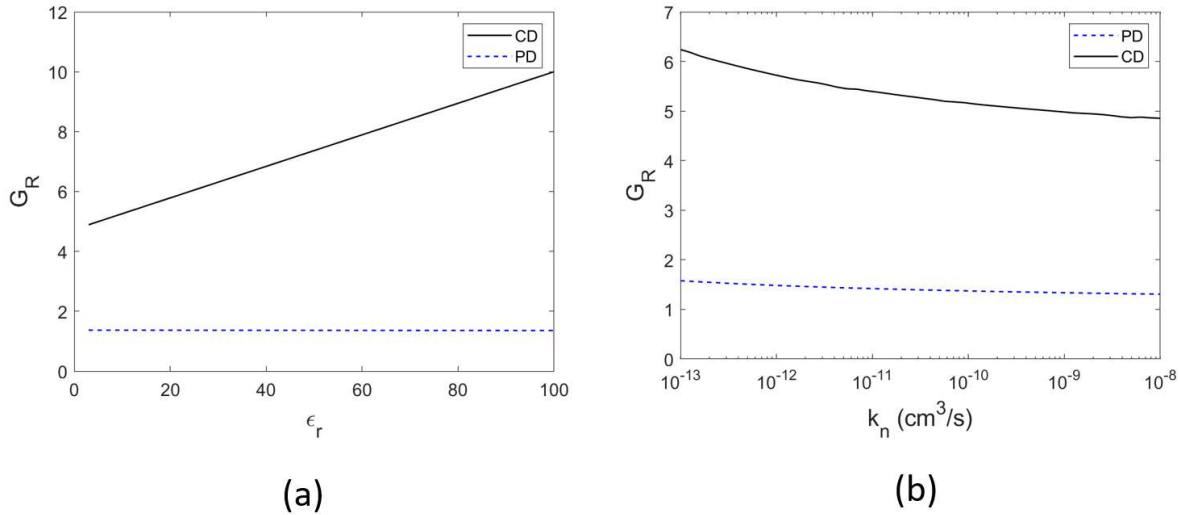


**Figure 46: (a) Gain as a function of dielectric permittivity; (b) Gain as a function of the adsorption constant.**

The gain of a nanowire is given by:

$$G_{R,NW} = \frac{(r - r_{D,l})^2}{(r - r_{D,d})^2} \quad (234)$$

where  $r_{D,l}$  is the radius of the depletion width under illumination and  $r_{D,d}$  is the radius of the depletion width in the dark. Nanowires have similar trends in gain compared to the PD planar devices. Their gain is maximized for the radius equal to the depletion width in the dark, and their gain has a similar dependence on material parameters as the PD planar case. However, it is difficult to say which nanowire geometry is comparable to a given planar geometry, and therefore it is difficult to compare their gain. It is also difficult to compare nanowires of different radii to each other because their geometry cannot be changed

to ensure they deplete at the same time. We compare the gain for nanowires of different radii without optimized geometry in Figure 47. The nanowires have the parameters shown in Table 1 and Table 13. The depletion width in the dark is calculated as the depletion width after 0.1 millisecond from an initial condition of  $q_c(0) = 0$ . The illuminated depletion width is calculated with (129). All incident photons are assumed to be absorbed and photogenerated holes homogenously distributed across the surface – that is,  $L_{nw} = I_{opt}/h\nu$ . The results show that the gain increases with decreasing nanowire radius.

**Table 13: Material parameters for calculations in Figure 47.**

$I_{opt} (W/cm^2)$	$\alpha (cm^{-1})$	$q_{c,d} (cm^{-2})$	$\lambda (nm)$
1	$1.414 \times 10^5$	$q_c(t = 0.1ms)$	340

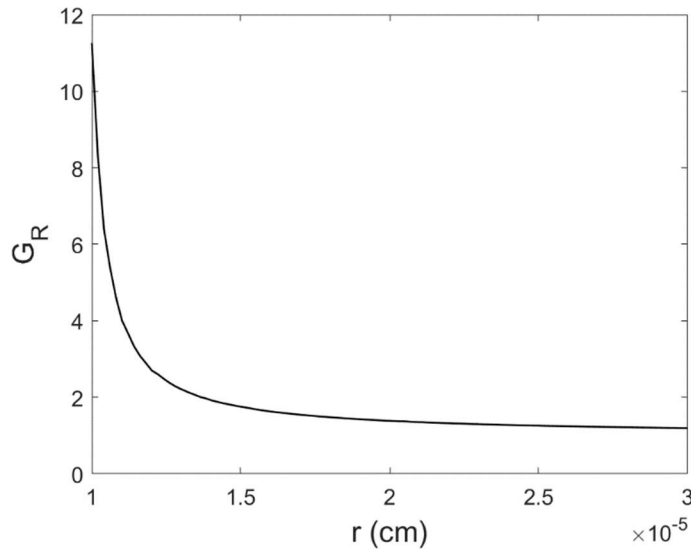


**Figure 47: Gain as a function of nanowire radius for parameters shown in Table 13.**

To compare nanowires to planar devices, we examine a nanowire and a planar device both with optimized geometry – that is their theoretical resistance in the dark is infinite. The ratio of the planar gain to the nanowire gain is then the ratio of their illuminated resistances:

$$\frac{G_{R,nw}}{G_{R,pl}} = \frac{\pi(r - r_{D,l})^2}{d(W - W_{D,l})} \quad (235)$$

where  $r$  is the radius of the nanowire, and  $r_{D,l}$  is the radial depletion width of the nanowire under illumination. The ratio of the gains is dependent not only on the change in the depletion widths but also the depth of the planar device. We examine the ratio of gains for a range of depths which are reasonable within the limits of fabrication technology and common within photodetector devices. The calculations are done using the parameters in Table 1 and Table 14. The nanowire is assumed to absorb all incident photons and distribute the photogenerated holes homogenously across the surface. The results are shown in Figure 48. The nanowire gain is greater than the planar gain for the depth less than about  $1\mu\text{m}$ . As the planar device is made larger, the overall resistance decreases. However, increasing the depth will increase the device area. This may degrade the signal if the incident beam is smaller than the total device area.

**Table 14: Parameters for calculations in Figure 48. The adsorbed concentration in the dark,  $q_{c,d}$  is set to ensure both devices are in CD.**

$q_{c,d} (\text{cm}^{-2})$	$r (\text{nm})$	$W (\text{nm})$	$I_{opt} (\text{W}/\text{cm}^2)$	$\alpha (\text{cm}^{-1})$	$\lambda (\text{nm})$
$q_c(0.87\text{ns})$	75	36.2	100	$1.414 \times 10^5$	340

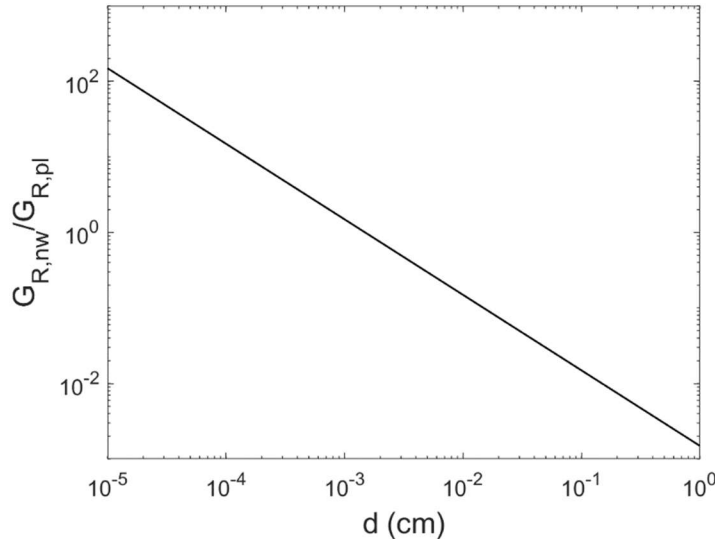


**Figure 48: Ratio of nanowire gain to planar gain as a function of planar device depth.**

Experimental measurements of the gain are consistent with the theoretical analysis presented in this section. Figure 49(a) shows the resistive gain for ZnO thin films fabricated with RF magnetron

sputtering with different thicknesses, and Figure 49(b) shows the gain for ZnO thin films fabricated with a sol-gel method. Both show a trend of increasing gain with decreasing thickness. For the sol-gel fabricated thin films, there is a sharp increase in the gain around a thickness of 785nm, as would be expected as the device thickness approaches the dark depletion width thickness. For smaller thicknesses however the gain starts to decrease. This may be due to a change in the carrier concentration with film thickness.

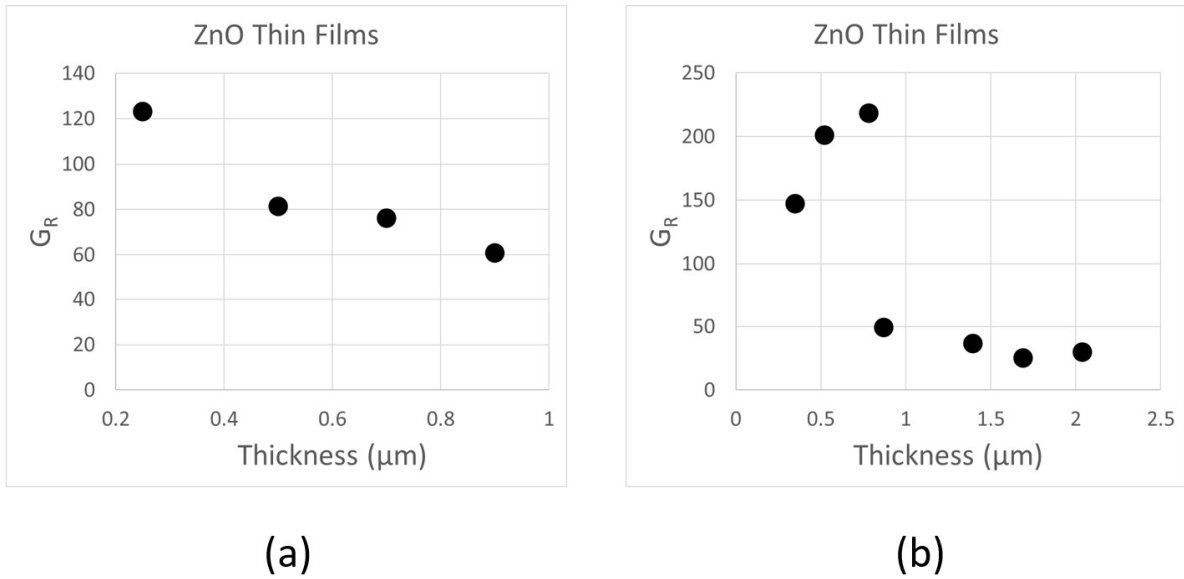


**Figure 49:** Experimental measurements of ZnO thin film resistive gain as a function of thickness, (a) deposited by magnetron sputtering [85], and (b) deposited by sol-gel method [86].

Figure 50 shows a comparison of the performance of ZnO nanowires as a function of nanowire diameter. These nanowires all have contacts such that current flows along the length of the nanowire rather than through the nanowire walls as with vertical nanowire films. The nanowires are illuminated with different illumination intensities, so we normalize their gain to the illumination intensity:

$$G'_R = \frac{G_R}{I_{opt}} \quad (236)$$

As discussed previously, this accounts for the increase in gain with increasing illumination intensity. The plot shows that in general the gain tends to increase with decreasing nanowire diameter.

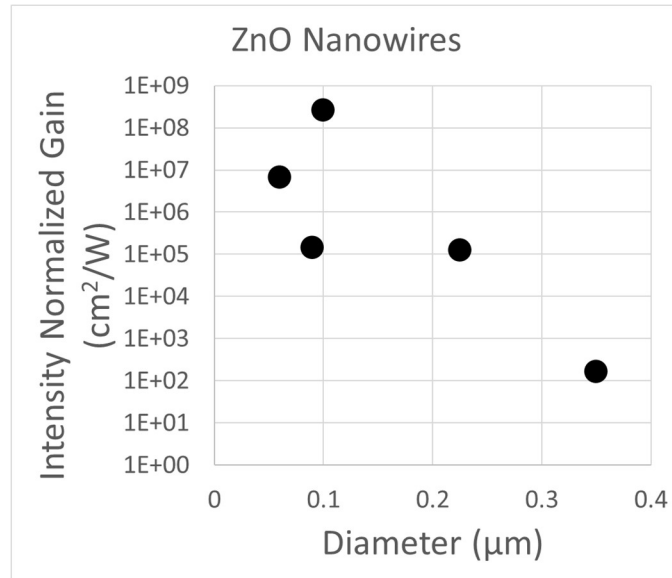


**Figure 50: Intensity normalized gain as a function of nanowire diameter for various ZnO nanowires created with different fabrication processes [9], [69], [87], [88].**

Figure 51 shows a comparison the performance of various ZnO photoconductors. This is an updated version of Figure 1 considering the discussion on photoconductor performance metrics given in this chapter. It is somewhat difficult to compare the performance of these devices from the cited papers for various reasons. First, the performance of the device depends strongly on the humidity as discussed in Section 3.10.3 and experimentally shown in [69]. In the majority of papers, the atmospheric conditions are not measured so the effect of humidity on the measured performance cannot be included. Second, each of these devices is measured under a different illumination intensity. While the illumination normalized gain helps somewhat to represent the effect of the illumination intensity on the gain, the gain is not linearly dependent on the illumination intensity and therefore the metric fails to give an accurate comparison between devices. Finally, because there is no single dark current value for most of these devices, the recovery times are chosen arbitrarily. That is, each of these devices could be just as easily operated at shorter or longer response times in exchange for a decrease or increase in gain.

Despite the difficulties in comparing devices, Figure 51 does show some trends. Nanowire devices tend to have higher gain than the thin film devices. The nanoparticle films (labeled as ‘ZnO

QDs’) tend to have lower gain than the thin film and nanowire devices. The ZnO/Graphene nanocomposite devices have both the largest gain and lowest response times in the plot.

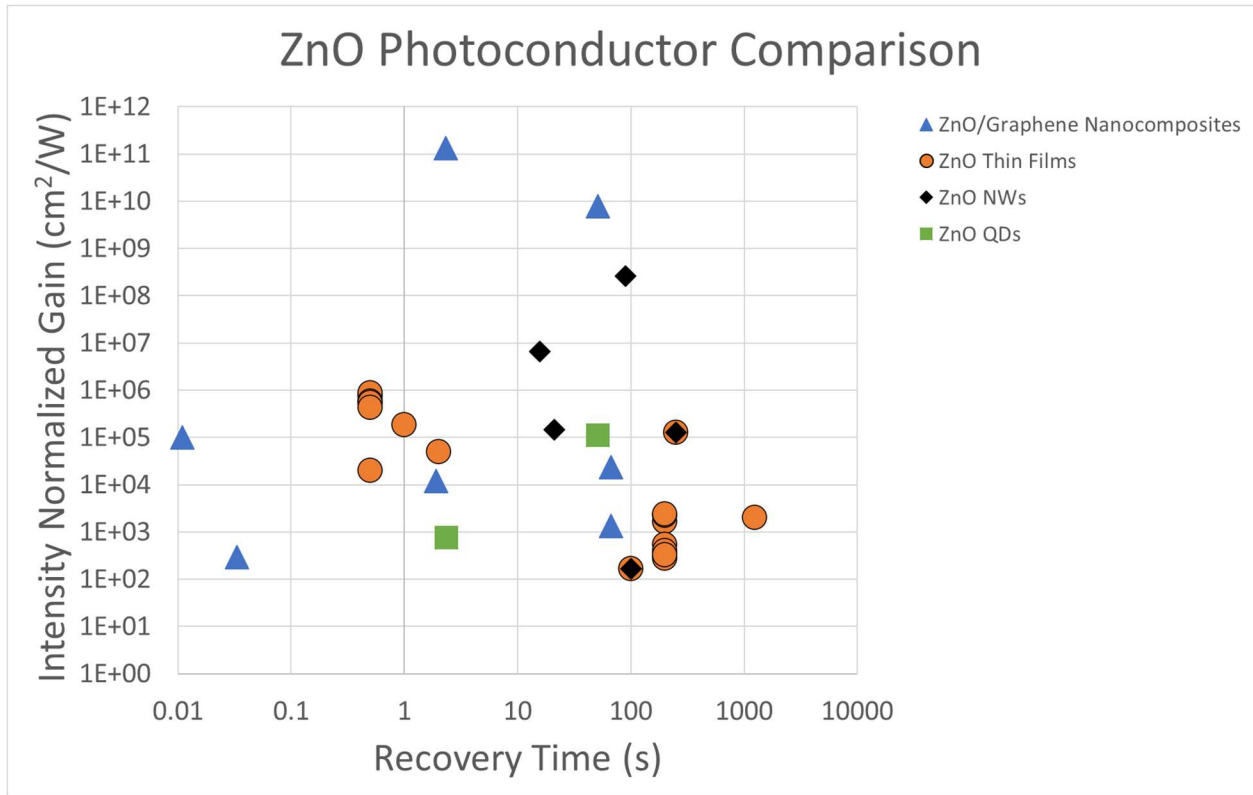


**Figure 51: Intensity normalized gain as a function of recovery time for various ZnO photoconductor devices [9], [11], [13], [41], [43], [50], [69], [85]–[91].**

The analysis in this section shows that the most important parameters for controlling the gain are the carrier concentration, the device thickness, the oxide thickness, and the surface curvature. In general, there is a tradeoff between the gain and the dark resistance. The dark resistance should be made small enough that the output impedance of the voltage divider is much smaller than the input impedance of the following stage and that the input noise current does not generate a large noise voltage across it.

#### 4.2 Response Time, Bandwidth, and Optical Bode Plots

Unlike in traditional photodetectors with an exponential transient response, metal oxide photoconductors do not have a single response time that accounts for both the rise and fall time. The photodesorption transient is generally linear with a slope proportional to the illumination intensity. The

desorption transient is determined by the relevant adsorption equation. In addition, because adsorption takes a very long time to reach equilibrium, there is not necessarily a practical steady-state dark resistance that can be defined. Therefore, the response time cannot be defined independently of the dark resistance, and it will change depending on the chosen dark resistance. To calculate the response time for a given illumination intensity, we first select the dark resistance. The rise time,  $\tau_r$ , is then the time it takes for the device to change from the chosen dark resistance to 95% of the illuminated resistance, and the fall time,  $\tau_f$ , is the time for the device to change from the illuminated resistance to the dark resistance. A plot of this is shown in Figure 52. There are then multiple possible response times depending on the dark resistance chosen. For planar devices, the rise time is given by (85) and the fall time is given by (45). Note that the rise time for the photocurrent,  $\tau_r$ , is referred to as the fall time for the adsorbed concentration,  $t_f$ , and similarly for the photocurrent fall time. We refer to the illuminated response time here as the rise time and discuss the photocurrent instead of the photoresistance to remain consistent with other photodetector literature. The maximum between  $\tau_f$  and  $\tau_r$  is called the response time,  $\tau$ , because it is the limiting factor in the response time.

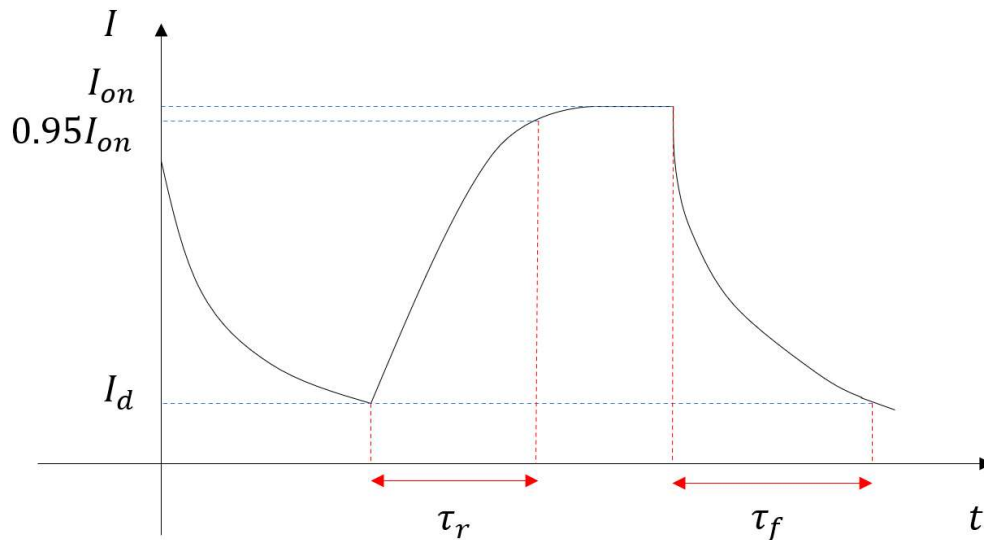


**Figure 52: Photocurrent and response time definitions.**

Although the response time could be defined at an on-current that is not at the illuminated steady-state, we define it as such here because it is the on-current that maximizes the response. This is because the adsorption rate is much higher at  $I_{on}$  than for any current less than  $I_{on}$  and thus will maximize the change in current.

We can use these definitions to calculate device performance metrics as a function of optical frequency. To do this, we first specify an optical power incident on the device. Then for the given optical power, the steady-state illuminated adsorbed concentration is calculated. Then, the rise and fall response times to each adsorbed concentration value greater than the steady-state is calculated. The optical frequency is defined as the maximum of the two response times. The performance metrics are calculated from the dark resistance corresponding to the adsorbed concentration at the given frequency.

The performance metrics for a PD device and the parameters given by Table 1 and Table 15 are shown in Figure 53. The biasing resistor is arbitrarily set to  $1k\Omega$ . The gain, dark resistance, SNR, and photovoltage all decrease with increasing frequency as the dark resistance approaches the illuminated resistance. The average power consumption increases as the dark resistance decreases, increasing the current through the voltage divider. The most important feature of these bode plots however is that they do not have a pass band. This is because the dark resistance does not have a steady-state value but instead continues to decrease with decreasing frequency. The device then does not have a well-defined bandwidth. However, because there is not a well-defined bandwidth (or equivalently, single response time), the standard noise equations for photoconductors have to be redefined. Generally, the bandwidth in the thermal noise term given by (206) and the shot noise given by (207) is defined by the minority carrier recombination lifetime of the photodetector. We cannot define such a term here. In practical applications, the bandwidth can be defined simply as the electrical bandwidth of the noise filter. This allows us to easily calculate the thermal noise. However, the shot noise is based on bulk recombination-generation. Recombination due to adsorption cannot be represented by the same statistics as that for bulk-recombination, so the shot noise term defined by (207) cannot be used. In order to characterize noise due

to fluctuations in generation and recombination, a new shot noise term based on the adsorption equation must be derived.

Table 15: Parameters for calculations in Figure 53.

$W$ ( $\mu\text{m}$ )	$I_{opt}$ ( $\text{W}/\text{cm}^2$ )	$\alpha$ ( $\text{cm}^{-1}$ )	$\lambda$ ( $\text{nm}$ )	$V_a$ (V)	$d$ ( $\mu\text{m}$ )	$l$ ( $\mu\text{m}$ )	$R_b$ ( $\text{k}\Omega$ )
1	$1 \times 10^{-3}$	$1.414 \times 10^5$	340	1	1	1	1

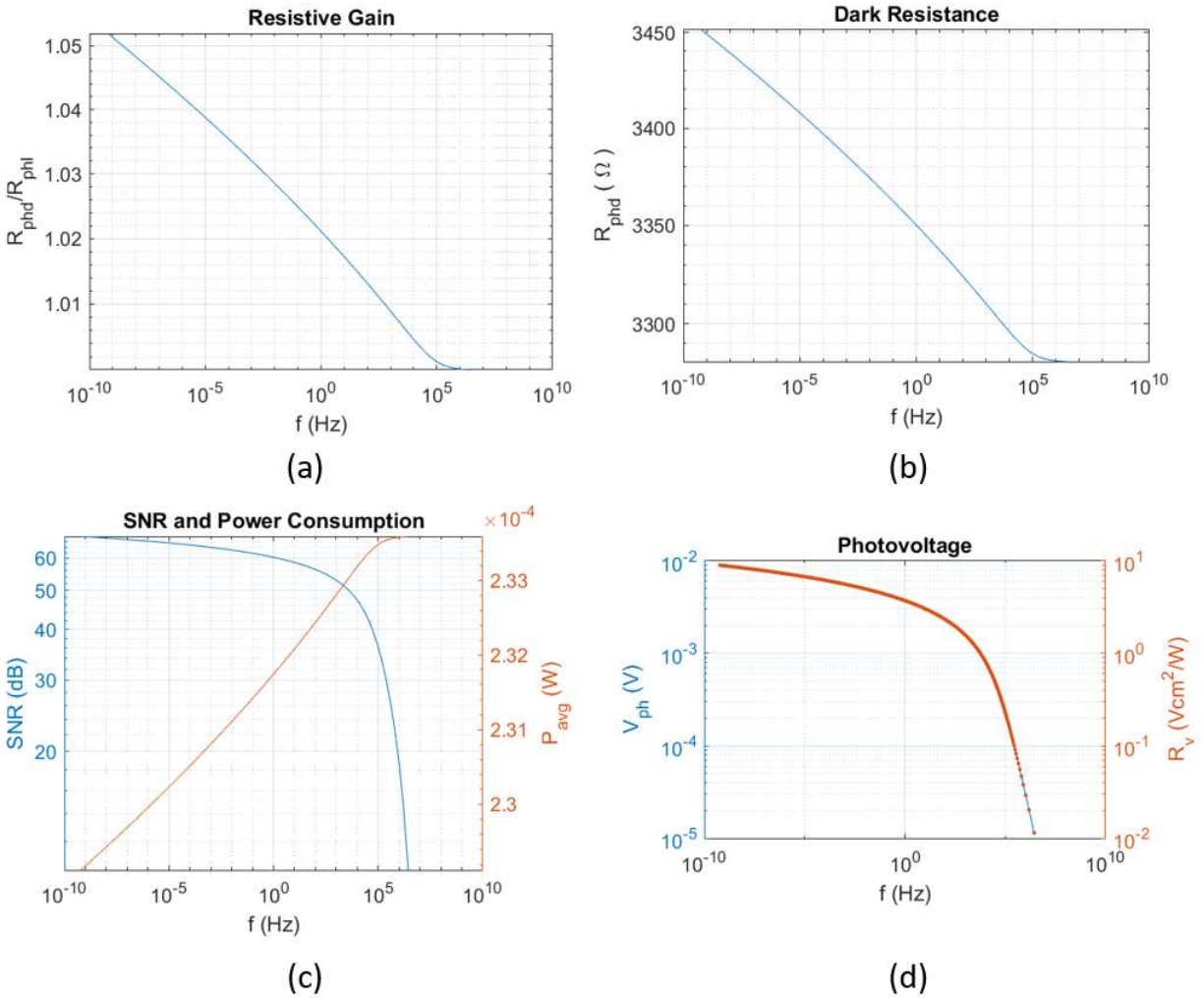


Figure 53: Performance metrics as a function of optical frequency for parameters in Table 1 and Table 15. (a) Resistive gain, (b) dark resistance, (c) SNR and average power consumption for voltage divider circuit, voltage measured across biasing resistor and using a bandwidth of 1MHz (d) photovoltage and voltage responsivity for the voltage divider circuit.

The performance metrics for a similar CD device is shown in Figure 54. The gain and dark resistance increase compared to the device in Figure 53 for each operating frequency. The SNR does not appear to increase significantly because the power dissipation is smaller than that in Figure 53 (d). For the same power consumption, the SNR would be significantly higher. The kinks in the plot occur because two different sets of equations are used to calculate the resistance depending on if the device is PD or CD.

**Table 16: Parameters for CD device shown in Figure 54.**

$t_{ox}$ (nm)	$W$ (nm)	$I_{opt}$ ( $W/cm^2$ )	$\alpha$ ( $cm^{-1}$ )	$\lambda$ (nm)	$V_a$ (V)	$d$ ( $\mu m$ )	$l$ ( $\mu m$ )	$R_b$ ( $k\Omega$ )
100	100	$1 \times 10^{-3}$	$1.414 \times 10^5$	340	1	1	1	1

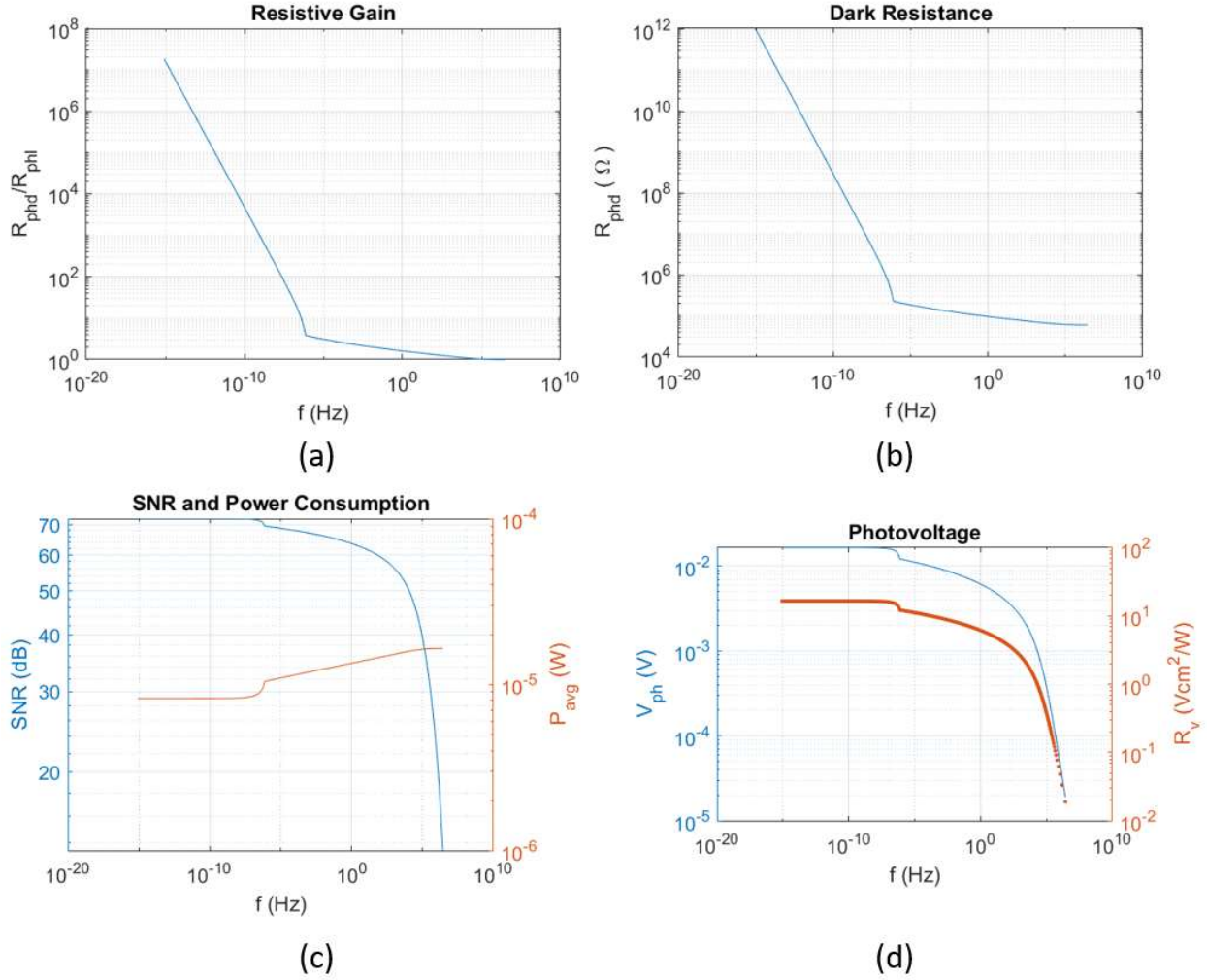


Figure 54: Performance metrics as a function of optical frequency for parameters in Table 1 and Table 16. (a) Resistive gain, (b) dark resistance, (c) SNR and average power consumption for voltage divider circuit, voltage measured across biasing resistor with a bandwidth of 1MHz, and (d) photovoltage and voltage responsivity for the voltage divider circuit.

### 4.3 Minimum Detectable Power

The minimum detectable power is determined not only by the SNR, but also by the adsorption rate. If the photodesorption rate is less than the adsorption rate, the photo-resistance will not decrease but continue to increase until the adsorption and desorption rates are equal. Therefore, the minimum detectable power is determined by the adsorption rate. In planar devices, the adsorption rate can be converted into the corresponding equivalent optical power through the equation:

$$I_{opt,min} = R_{ads}h\nu \quad (237)$$

It is useful to plot the minimum detectable optical power over time to determine if the device will meet certain application requirements. Figure 55 shows the minimum detectable optical power over time for partially depleted devices as a function of carrier concentration. The plot shows that the minimum detectable optical intensity decreases faster for higher carrier concentrations. The dependence of the minimum detectable optical intensity on the adsorption constant is shown in Figure 56. It shows that the adsorption constant has a small impact on the minimum detectable optical intensity.

Table 17: Parameters for Figure 55.

$W$ ( $\mu m$ )	$q_c(0)$ ( $cm^{-2}$ )	$k_n$ ( $cm^3/s$ )	$N_T$ ( $cm^{-2}$ )	$\epsilon_r$	$\alpha$ ( $cm^{-1}$ )	$\lambda$ ( $nm$ )
1	0	$1 \times 10^{-10}$	$1 \times 10^{15}$	8.4	$1.414 \times 10^5$	340

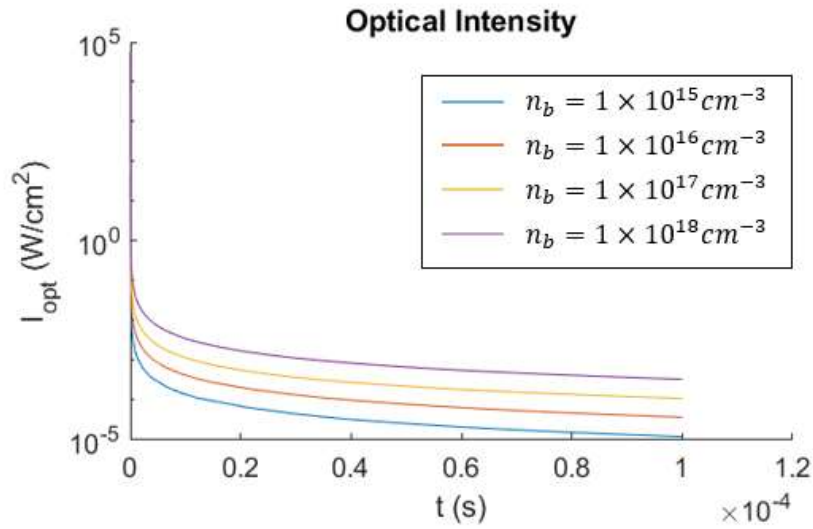
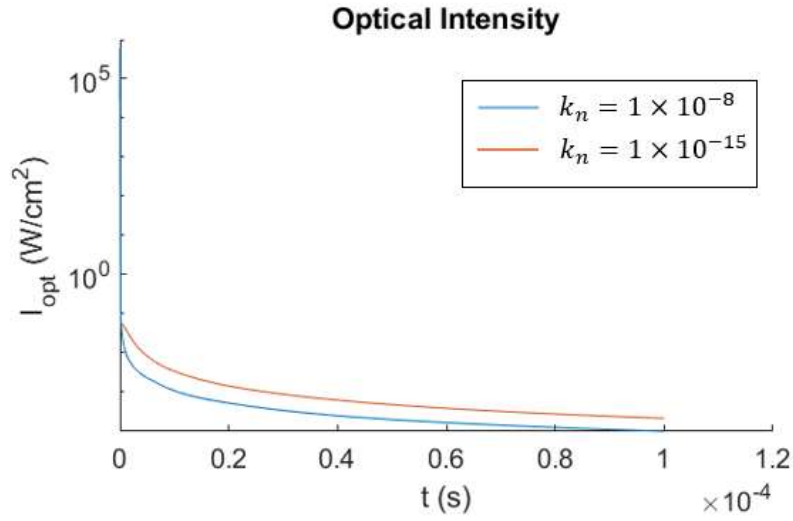


Figure 55: Minimum detectable optical intensity for parameters given in Table 17.



**Figure 56: Minimum detectable optical power for different adsorption rate constants. Parameters are given in Table 17 and  $n_b = 1 \times 10^{17} \text{ cm}^{-3}$ .**

Figure 57 compares the minimum detectable optical power for the PD device in Table 17 and the CD device in Table 18. Both devices have  $n_b = 1 \times 10^{17} \text{ cm}^{-3}$ . As shown in Figure 57, for a backgate voltage of 0, the minimum detectable optical intensity decreases much faster than the PD device. This is because some of the charge for adsorption comes from the metal backgate. For a backgate voltage of 0.5V, the optical intensity decreases significantly faster, reaching  $\sim 0.01 \text{ nW/cm}^2$  about 10 microseconds. This is a significant advantage for applications which require detection of low optical powers at high speeds. The disadvantage of applying backgate voltage is that it creates a very large voltage drop across both the metal oxide and the insulating back gate oxide, and dielectric breakdown might occur.

**Table 18: Parameters for CD devices in Figure 54.**

$W$ (nm)	$q_c(0)$ ( $\text{cm}^{-2}$ )	$k_n$ ( $\text{cm}^3/\text{s}$ )	$N_T$ ( $\text{cm}^{-2}$ )	$\epsilon_r$	$\alpha$ ( $\text{cm}^{-1}$ )	$\lambda$ (nm)	$t_{ox}$ (nm)
50	0	$1 \times 10^{-10}$	$1 \times 10^{15}$	8.4	$1.414 \times 10^5$	340	100

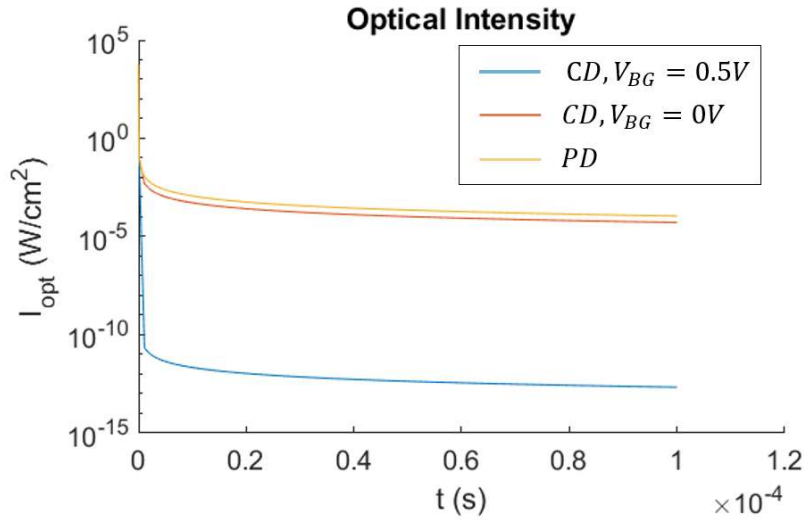


**Figure 57: Minimum detectable optical intensity for completely depleted device (Table 18) and partially depleted device (Table 17) and  $n_b = 1 \times 10^{17} \text{ cm}^{-3}$ .**

Figure 58 shows the minimum detectable optical power for nanowires of different radii. In these calculations, we assume all incident photons are absorbed to demonstrate the best possible performance (for example, if the nanowires are placed on a reflecting surface). The plot shows that the minimum detectable optical intensity decreases with decreasing nanowire radius. It also shows that for small nanowire radii, there is a minimum detectable limit. This occurs when the device becomes completely depleted. As the nanowires becomes smaller, the rate of adsorption decreases much faster, but there is also a smaller volume of electrons to enable adsorption. This is represented by a saturation in the plot. Note that technically the rate of adsorption goes to zero at the onset of complete depletion, but the release of a single electron from the surface due to any illumination intensity will set the adsorption rate to the saturation limit shown in the figure. Thus, the practical detection limit is given by the adsorption rate at the onset of CD. Figure 59 compares the nanowire device performance to the planar device performance. The nanowires can detect lower optical intensities than the planar devices assuming the nanowires absorb 100% of the incident light. Figure 60 shows the effect of partial absorption due to (127) on the minimum detectable optical intensity. As expected, there is a significant increase in the detectable power.

Table 19: Parameters for Figure 58.

$n_b$ ( $cm^{-3}$ )	$q_c(0)$ ( $cm^{-3}$ )	$k_n$ ( $cm^3/s$ )	$N_T$ ( $cm^{-3}$ )	$\epsilon_r$	$\alpha$ ( $cm^{-1}$ )	$\lambda$ (nm)
$1 \times 10^{17}$	0	$1 \times 10^{-10}$	$1 \times 10^{15}$	8.4	$1.414 \times 10^5$	340

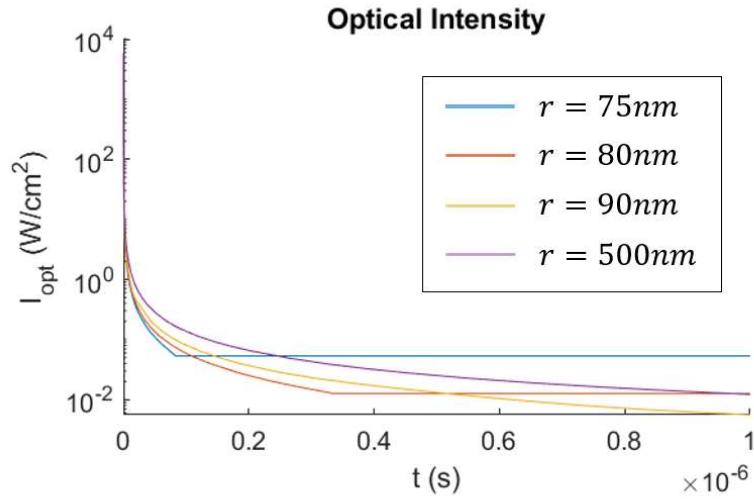


Figure 58: Minimum detectable optical power over time for nanowires with parameters given in Table 19.

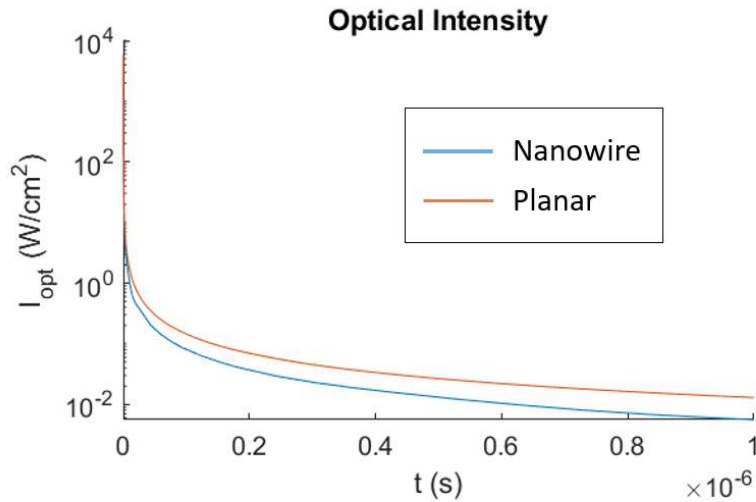


Figure 59: Comparison of minimum detectable optical intensity for nanowire with  $r = 100nm$  and parameters in Table 19 and PD planar device with parameters in Table 17 and  $n_b = 1 \times 10^{17} cm^{-3}$ .

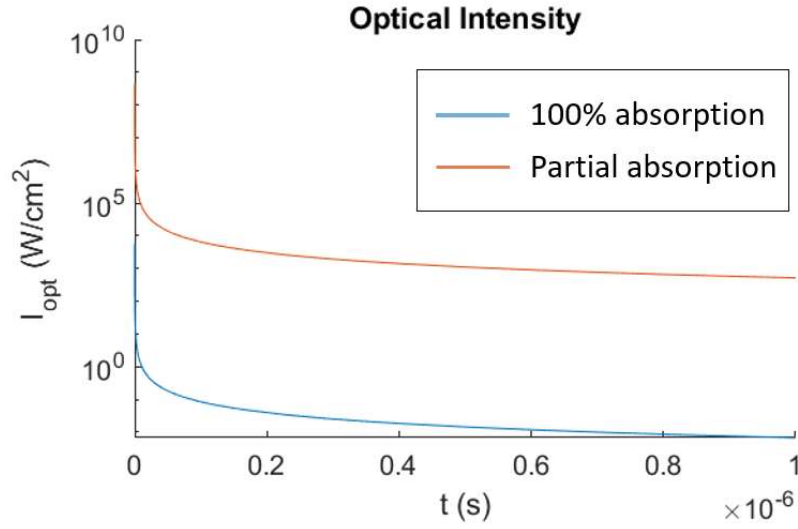


Figure 60: Effect of partial absorption according to (127) on minimum detectable optical intensity. Parameters are given in Table 19 and  $r = 100\text{nm}$ .

#### 4.4 Device Design for Bacterial Fluorescence

The previous sections provide us with tools for designing metal oxide photodetectors for bacterial fluorescence detection. The plots from the prior section indicated that achieving a minimum detectable intensity of  $1\text{nW/cm}^2$  in nanosecond speeds is not feasible with standard planar or nanowire devices. However, based on Figure 57 the CD devices have the ability to achieve low detectable powers at high frequencies by applying a positive back gate bias to increase the adsorption rate. Figure 61 shows the minimum detectable optical intensity for Table 1 and Table 20 and a backgate bias of  $1\text{V}$ . The device is able to reach well below  $1\text{nW/cm}^2$  in under a nanosecond.

Table 20: Parameters for Figure 61.

$W$ (nm)	$t_{ox}$ (nm)	$\alpha$ (cm <sup>-1</sup> )	$\lambda$ (nm)	$V_{BG}$ (V)	$q_c(0)$ (cm <sup>-2</sup> )
30	100	$1.414 \times 10^5$	340	1	0

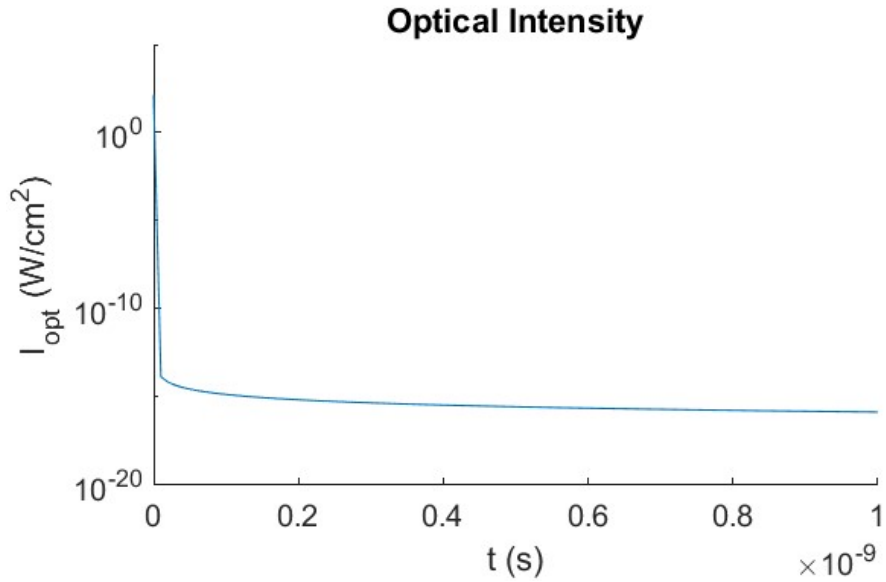


**Figure 61: Minimum detectable optical intensity for CD device with backgate bias of 1V and parameters given by Table 1 and Table 20.**

However, the gain is also degraded when a positive backgate bias is applied. If the backgate is removed, however, the adsorbed concentration remains the same and a low minimum detectable intensity can be achieved with a higher gain. An example of this is shown in Figure 62. A backgate bias is turned on and off and the minimum detectable intensity is calculated at each time for  $V_{BG} = 0V$ . While the bias is applied, the minimum intensity decreases rapidly, and after the bias is removed it remains constant.

**Table 21: Parameters for Figure 62.**

$W$ (nm)	$t_{ox}$ (nm)	$\alpha$ ( $cm^{-1}$ )	$\lambda$ (nm)
60	100	$1.414 \times 10^5$	340

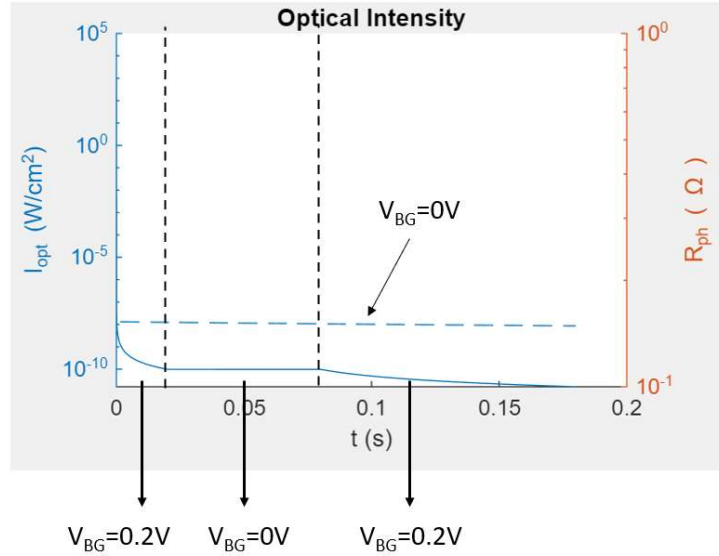


**Figure 62: Minimum detectable intensity for a pulsed backgate. Parameters are from Table 1 and Table 21.**

An example of the photoresponse for a pulsed backgate CD device is shown in Figure 63. A backgate bias of 0.2V is applied to reduce the minimum detectable intensity. The backgate bias is removed to increase the response and the sample is illuminated from  $t=0.02\text{s}$  to  $0.06\text{s}$  with  $10\mu\text{W}/\text{cm}^2$ . In bacterial fluorescence measurements, a phase-locked loop mode is often employed. The pulsing signal in this mode could be applied to the backgate in this mode to sensitize the device to low intensities, increase the gain, and reduce the response time.

**Table 22: Parameters for Figure 63.**

$I_{opt} (W/cm^2)$	$l (\mu m)$	$d (\mu m)$	$\mu_n (cm^2/Vs)$
$1 \times 10^{-5}$	1	100	200

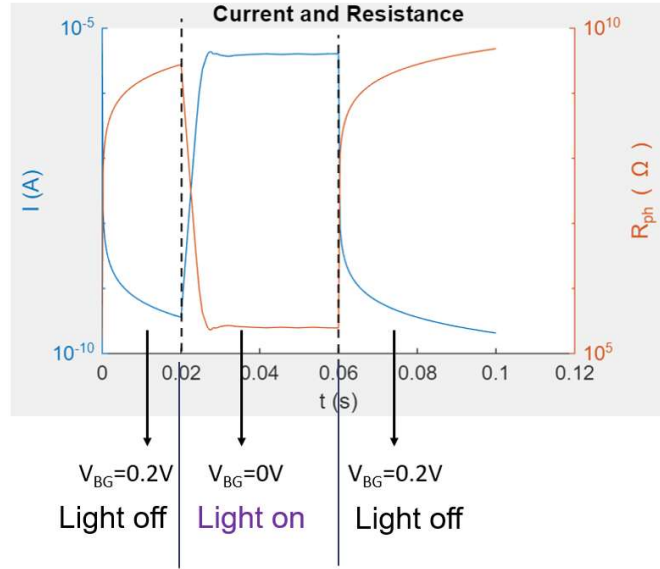


**Figure 63: Pulsed mode CD device for the parameters shown in Table 1 and Table 22.**

To reach low intensities very quickly a CD nanowire could be fabricated as shown in Figure 64. As discussed in the previous section, the minimum intensity for nanowires decreases faster than planar devices, particularly for small radii. However, they completely deplete quickly, limiting their minimum detectable power. In a CD mode, the backgate would enable nanowires with small radii to continue adsorbing past complete depletion. However, these devices would need to be paired with a reflective material to reflect light that is not absorbed and increase the percent of absorption.

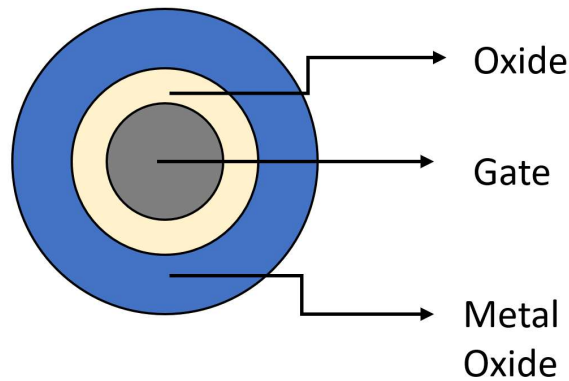


**Figure 64: CD nanowire cross-section schematic.**

The resistance of these CD devices can be very high especially in low-mobility metal oxide materials. It may be advantageous then to form a heterojunction with a high mobility material such a

graphene to increase the resistance while maintaining the gain. As discussed in Section 3.9.1 and 3.9.2 the adsorption rate will mostly be controlled by the bulk material rather than the surface material, so the carrier concentration of channel material should be chosen according to the desired gain and adsorption rate while the UV-sensitive metal oxide surface layer should be made thick enough to ensure a sufficient percentage of the light is absorbed. These types of devices have already been created in a completely depleted form, but the back gate has not been used in a PLL circuit to decrease the response time and the minimum detectable intensity [92].

Another limitation for detecting very low illumination intensities is that the rise time is proportional to the illumination intensity. This can be seen clearly in Figure 34. For optical intensities as low as  $1\text{ nW/cm}^2$ , it may take on the order of seconds to reach steady-state, and operation at high frequencies will significantly degrade the signal. An alternate mode of operation is to place the metal-oxide-semiconductor formed by the CD geometry in series with a resistor, as shown in Figure 65. and use the injection and ejection current to detect the signal at very fast speeds. The equation for the ejection current given by (203) indicates that the current under illumination will change almost immediately and be proportional to the illumination intensity. Realistically, the response time will be limited by the RC time constant determined by the back gate capacitance of the photoconductor and the series resistor.

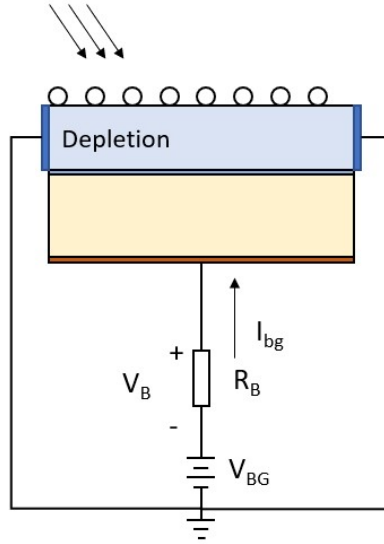


**Figure 65: Capacitive mode circuit. The dark blue sections indicate the contacts.**

An example of the capacitive mode photoresponse is shown in Figure 66. A backgate voltage is applied while the illumination is off (both before and after). The effect of the biasing resistor is not included here. The response time is theoretically instantaneous, and the current is  $\sim 10\text{nA}$ . A biasing resistor of  $1\text{k}\Omega$  will give an output voltage of  $10\mu\text{V}$  and a response time of  $1\mu\text{s}$ . Note that no external power is applied to this circuit – it operates at  $0\text{V}$  and generates its own power to produce a signal.

**Table 23: Parameters for Figure 66. Backgate voltage is pulsed only applied when the illumination is off.**

$W$ (nm)	$t_{ox}$ (nm)	$l$ (cm)	$d$ (cm)	$\mu_n$ ( $\text{cm}^2/\text{Vs}$ )
60	100	0.1	0.1	200
$I_{opt}$ ( $\text{W}/\text{cm}^2$ )	$\lambda$ (nm)	$V_{BG}$ (V)	$q_c(\mathbf{0})$	$\alpha$ ( $\text{cm}^{-1}$ )
$1 \times 10^{-5}$	340	0.3	0	$1.414 \times 10^5$

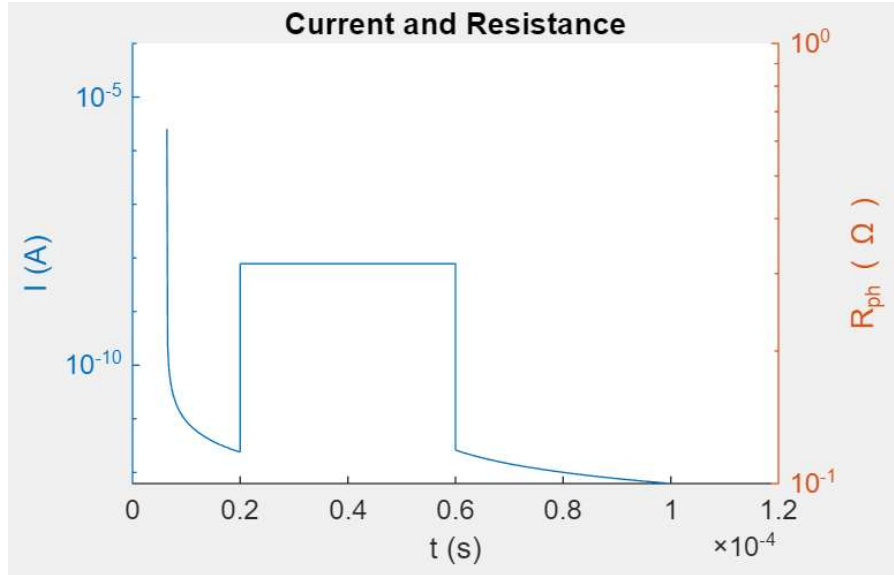


**Figure 66: Photoresponse of a capacitive mode circuit. Parameters given by Table 1 and Table 23.**

One issue with this mode of operation is that the voltage developed across the biasing resistor will affect the adsorption rate and limit the response. Placing the device in a TIA as shown in Figure 67 will prevent this. Additionally, the larger the RC time constant, the more the current may be degraded due to a limitation of the adsorption rate. Finally, although the current is proportional to the device area, the device should be made no larger than the area of the incident illumination, otherwise the signal will be degraded.

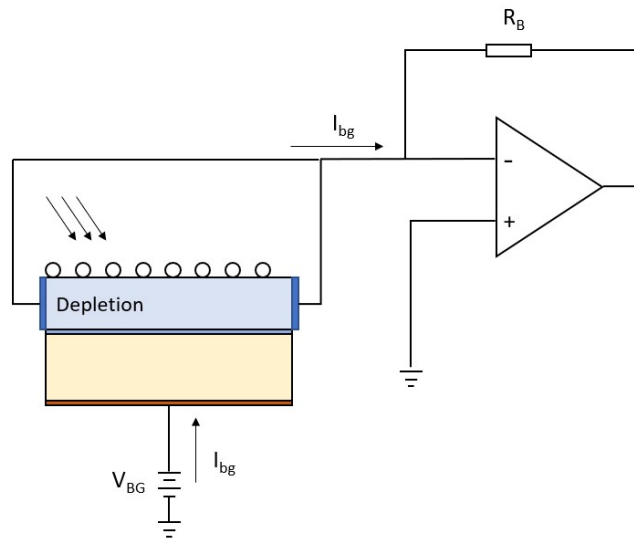


**Figure 67: Capacitive mode device in a TIA circuit.**

## 5. PARAMETER EXTRACTION AND FITTING

### 5.1 Adsorption Rate Constant Measurement

The material parameters required for characterization of the adsorption and photodesorption transients are the absorption coefficient  $\alpha$ , the internal quantum efficiency  $\eta_i$ , the carrier concentration  $n_b$ , the dielectric permittivity of the semiconductor  $\epsilon_s$ , the trap concentration  $N_T$ , and the adsorption rate constant  $k_n$ . In ZnO, the trap concentration at room temperature is generally considered to be a monolayer of oxygen with  $N_T \approx 1 \times 10^{15} \text{ cm}^{-2}$  [93], and this has been confirmed by thermal desorption experiments [37]. The capture cross-section of the trap has been measured for the ZnO  $10\bar{1}0$  face has been measured as  $\sigma = 1 \times 10^{-2}$  [93], and  $\sigma = 1 \times 10^{-2}$  [37]. The capture cross-section is related to the adsorption rate constant through the equation given by (4). However, these papers do not specify the method by which the capture cross-section is measured, the range is very large, and it has only been measured for a single face. Therefore, the adsorption rate constant needs to be measured for accurate modeling of metal oxide devices. Several methods of extracting the constant  $k_n$  are possible. In this section we discuss new methods for characterization of the adsorption constant.

#### 5.1.1 Kelvin Probe Force Microscopy Measurement Method

One method to extract the adsorption rate constant is to measure the surface potential as a function of illumination. The steady-state surface potential can be measured using Kelvin Probe force microscopy while the device is under a known illumination intensity. A similar method is used in [48], however the systems and equations differ. From (69), we can write the steady-state surface potential under illumination as for a PD planar device:

$$V_{s,ss} = \frac{kT}{q} \ln \left( \frac{L}{k_n N_T n_b} \right) \quad (238)$$

where  $L$  is the photodesorption rate. Then, the constant  $k_n N_T$  can be calculated from the steady-state surface potential if the carrier concentration, incident optical illumination intensity, absorption coefficient,

and internal quantum efficiency are known. If the depletion width is large enough in both dark and illumination and all absorbed photons contribute to holes reaching the surface, then the photodesorption term can be given as:

$$L = \frac{I_{opt}}{h\nu} \quad (239)$$

However, if the depletion width is not sufficiently large, the integral of the photogeneration term given by (72) must be used and the minority carrier diffusion length must be known as well.

### 5.1.2 Current Measurement Method

Another method is to plot  $\ln(-dI/dt)$  vs  $I$ , where  $I$  is the current during adsorption in the dark. A similar technique with an approximate form of (69) is used in [29]. The  $I$ -intercept of such a plot would yield:

$$\ln\left(-\frac{dI}{dt}\right)|_{I=0} = \ln\left(\frac{V_a \sigma d}{l} k_n N_T\right) - \frac{q^2 n_b W^2}{kT \epsilon_s} \quad (240)$$

where  $V_a$  is the voltage between the contacts. This method has the advantage that the preceding illumination intensity does not need to be known. Thus, if a majority of photogenerated holes are not swept to the surface, the hole diffusion length does not need to be known. However, it has the disadvantage of error introduced through the calculation of a numerical derivative and requires small time-steps for good accuracy. Furthermore, if the second term on the right-hand side of Eqn. 240 is much larger than the first term, the product  $k_n N_T$  cannot be accurately measured.

## 6. DEVICES

### 6.1 ZnO Thin Film on Thermal Oxide

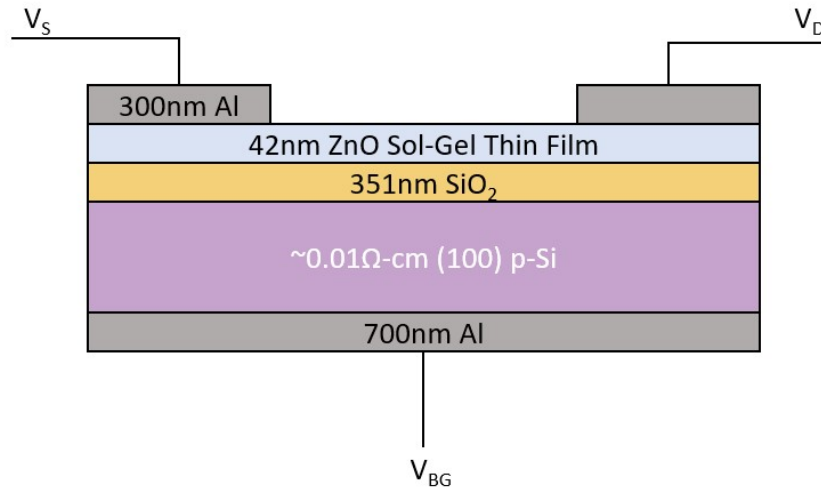


**Figure 68: CD ZnO UV photodetector device.**

The CD ZnO UV photodetector device shown in Figure 68 was fabricated. The device consists of a ZnO thin film created by sol-gel method on top of a p-type thermal oxide Si wafer. The device was used to verify that the adsorption rate of the ZnO can be controlled with the backgate and to verify the existence of the injection and ejection current.

The thermal oxide wafer (purchased from MSE Suppliers) is a Boron-doped (100) p-Si wafer with a conductivity of  $\sim 0.01\Omega\text{-cm}$  and a thermal oxide layer grown on top and polished. The thickness of the  $\text{SiO}_2$  layer is measured using ellipsometry as 351nm. The wafer is diced into  $\sim 1\text{ cm}^2$  pieces with a diamond scribe, and each piece is cleaned by rinsing in acetone, methanol, isopropanol, and DI water and dried with an  $\text{N}_2$  gun. A 700nm layer of Al is deposited on the backside of the samples via electron beam evaporation.

The ZnO thin film is created by the sol-gel method. Here, we follow the fabrication method outlined in [94]. The sol-gel solution is created by dissolving 6.48g of Zinc Acetate Dihydrate (ZAD)

(purchased from Carolina Biological) in 100mL of Methanol. The solution is heated to 62C in a reflux reaction and stirred continuously for 5 minutes until the solution is clear and the ZAD is fully dissolved.

The ZnO sol-gel solution is deposited onto the thermal oxide samples and spin-coated at 5200RPM for 30s. Immediately after spin-coating, the samples are placed on a hot-plate and heated at 120C for 10 minutes. Then, they are placed on the hot plate at 350C for 5 hours. After growth, they are stored in an airtight container with a desiccant.

The thickness of the thin films is measured as 42nm using ellipsometry. To confirm the uniformity and orientation of the thin film, SEM images of the thin films are taken. Figure 69 and Figure 70 show the SEM images of the thin film surface. They show many small columns of ZnO about 20nm in diameter with good uniformity. This is typical of most sol-gel ZnO thin films [94]–[96]. Hexagonal shapes can be seen in some of the columns, indicating c-axis orientation which is typical of ZnO sol-gel films [95]. However, X-Ray diffraction (XRD) measurements should also be taken to confirm the orientation.

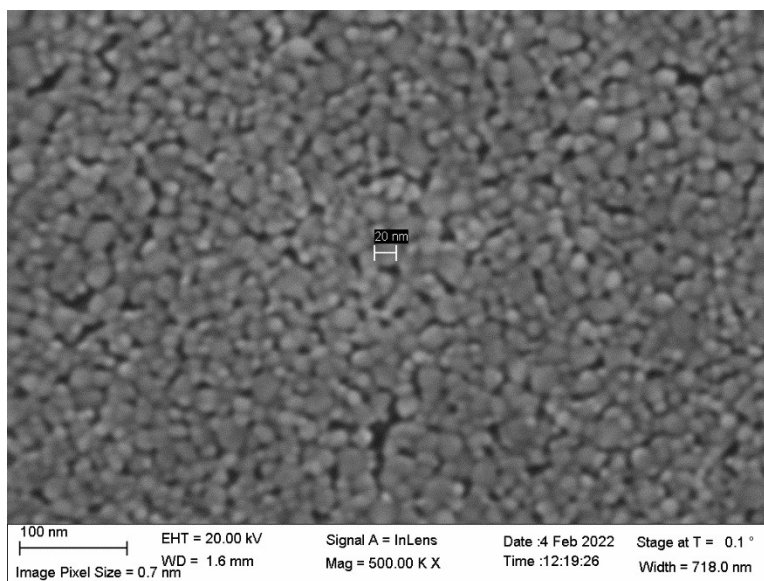


**Figure 69: SEM image of ZnO thin film. Columns are ~20nm in width.**

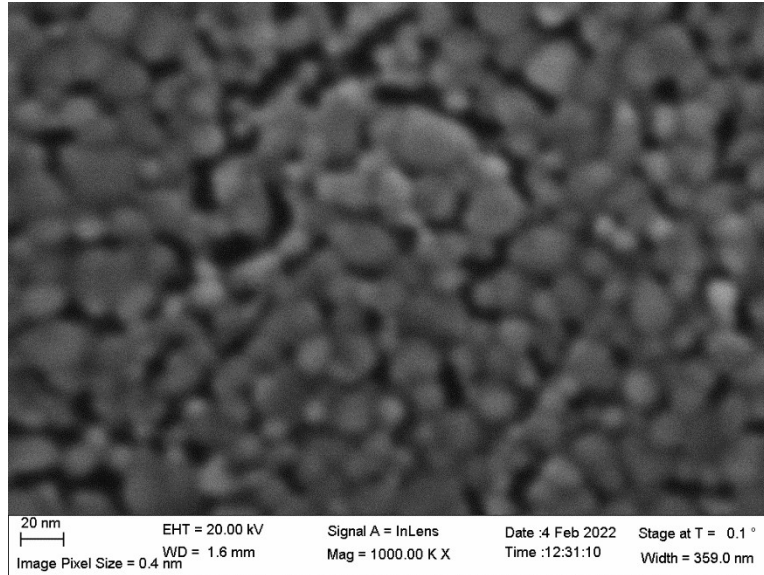


**Figure 70: High magnification of ZnO thin film. Columns appear to have roughly hexagonal geometry.**

Ohmic contacts are created by depositing 300nm of Al on the ZnO thin film via electron beam evaporation and shadow masks made from Aluminum flashing. The I-V curves of the samples are measured and verified to be ohmic.

### 6.1.1 Backgate Control of Adsorption Rate

To test the control of the adsorption rate via the back gate voltage, the setup shown in Figure 71 is constructed. The CD ZnO thin film device, represented by  $R_{ph}$  in the schematic, is placed in series with a 500k $\Omega$  resistor. An Analog Discovery Board is used as both power supply for the voltage divider and oscilloscope to measure the photovoltage. The analog discovery board is connected to a laptop computer via USB, and the computer is not connected to a wall outlet to reduce 60Hz noise. Since the Analog discovery board can only supply -5V to 5V, an external DC power supply is used to apply the backgate bias. The back gate bias is connected to a physical single pole double throw switch to switch between the voltage bias from the power supply and ground. An OSRAM LZ1-00UV0R 365nm LED is used to illuminate the sample. The LED is connected to a current source and supplied with 700mA. A Newport 1928-C optical power meter with 918D-UV photodetector is used to measure the incident illumination as 0.8W/cm<sup>2</sup>.

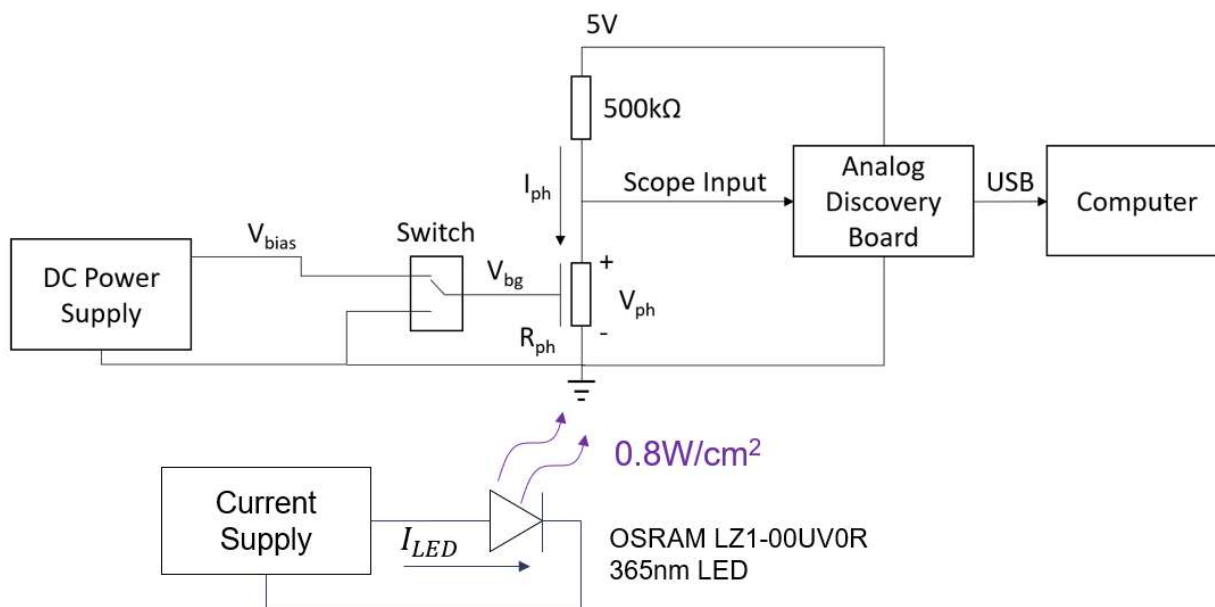


**Figure 71: Experimental setup for adsorption rate control via backgate bias.**

The sample is illuminated with the UV LED, then the light is removed and, the photo-decay is measured. Shortly after the illumination is removed, the backgate bias is applied. For  $V_{bg} > 0V$ , the photocurrent will suddenly decrease as the backgate bias is applied, and for  $V_{bg} < 0V$ , the photocurrent will suddenly increase as the backgate bias is applied. The backgate is maintained for several seconds, and then set back to zero.

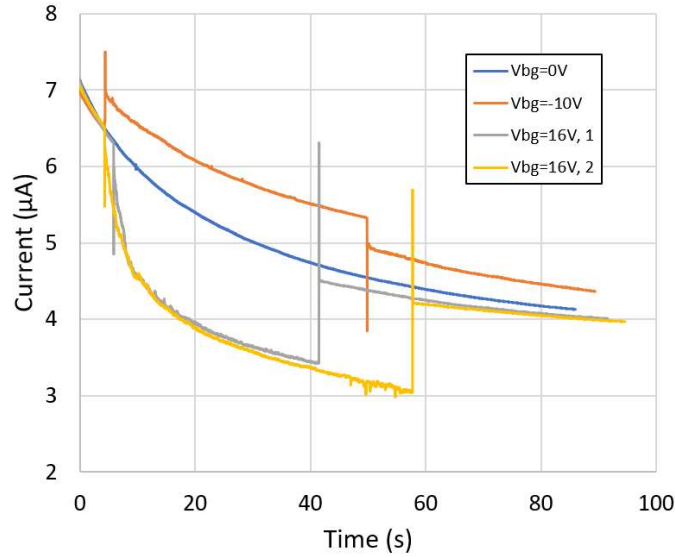


**Figure 72: Photocurrent for different backgate biases. For  $V_{bg} = 0V$ , the backgate bias is turned on at  $t = 4.17s$  and turned off at  $t = 50.13s$ ; for  $V_{bg} = 16V, 1$  (grey) the backgate bias is turned on at  $t = 5.84s$  and turned off at  $V_{bg} = 41.53s$ ; for  $V_{bg} = 16V, 2$  (yellow) the backgate bias is turned on at  $t = 4.21s$  and turned off at  $t = 57.83s$ .**

Figure 72 shows that the photocurrent does decay faster for a positive bias, and that it decays more slowly for a negative bias. Assuming that the photocurrent is related to the adsorbed concentration and not bulk photogenerated carriers, this means that the adsorbed concentration has been adjusted by the backgate. KPFM measurements should be combined with these measurements to confirm that the change in photocurrent is due to a change in the adsorbed concentration.

### 6.1.2 Measurement Injection and Ejection Current

To measure the backgate current, we construct the experimental setup shown in Figure 73. The backgate contact is connected to ground and both front-side contacts are tied together and connected to the biasing resistor. Because the photovoltage is very small relative to the resolution of the measurement equipment, we amplify the signal using a non-inverting op amp circuit with a gain of 101. The amplified signal is passed through a high-pass filter to remove 60Hz noise. The output voltage of the high-pass filter is measured with the Analog Discovery Board oscilloscope. The data is transmitted to a laptop computer which is not connected to a wall outlet to limit 60Hz noise. The OSRAM LZ1-00UV0R 365nm LED used in Section 6.1.1 is used here with the same illumination intensity.

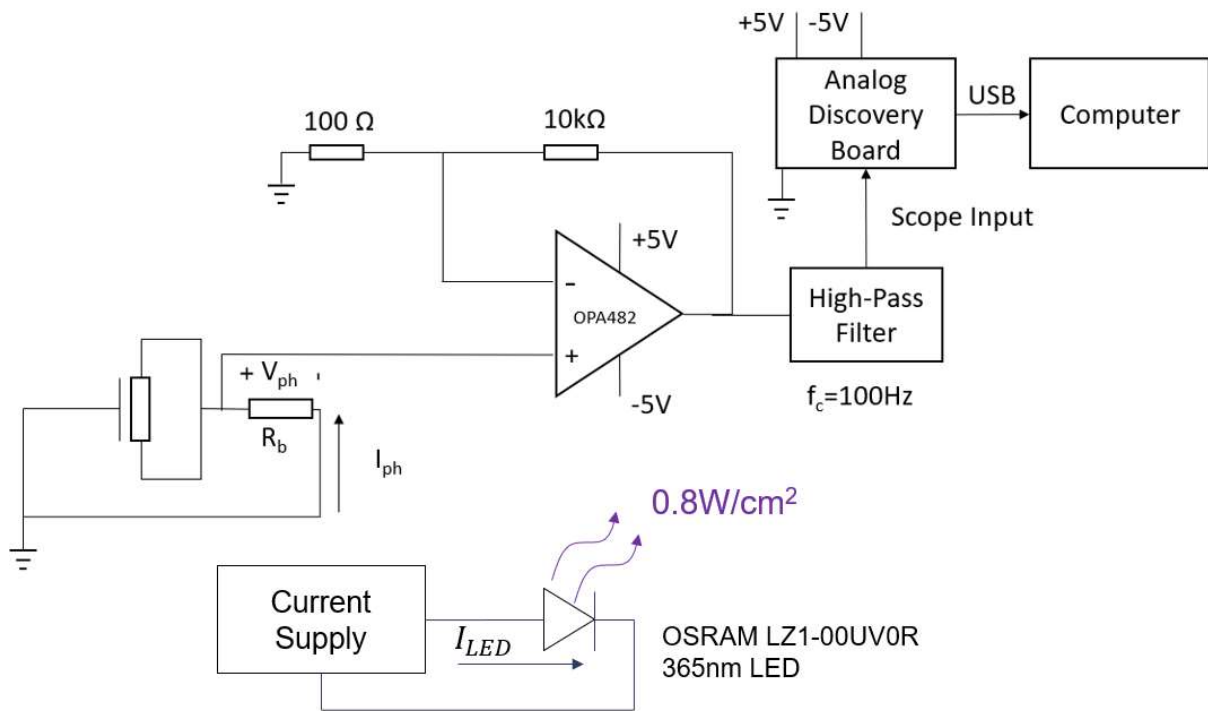


Figure 73: Experimental setup for measuring backgate current.

Figure 74 and Figure 75 show the measurements for two different biasing resistors. The plots qualitatively match the model presented in Section 3.11.2. The backgate current quickly turns on when light is shone on the sample. The photovoltage is negative indicating that the electrons are moving from the semiconductor to the backgate. The current then decays while the light is still on as the adsorption rate reaches the photodesorption rate. When the light is turned off, the current then spikes again as adsorption begins again and electrons move from the backgate to the semiconductor. The photovoltage is now positive consistent with the expected direction of electrons. The response time of the photovoltage is also dependent on the biasing resistor. In Figure 75, the response time is measured as  $0.5\mu\text{s}$ . This is on the order of the sampling time of the oscilloscope, so it is possible that the actual response time is smaller than  $0.5\mu\text{s}$ . The response time of Figure 74(a) is  $30\mu\text{s}$ , a significant increase in the response time. Figure 75(b) shows ringing behavior in the response. It is not clear what is causing this response and requires more investigation.

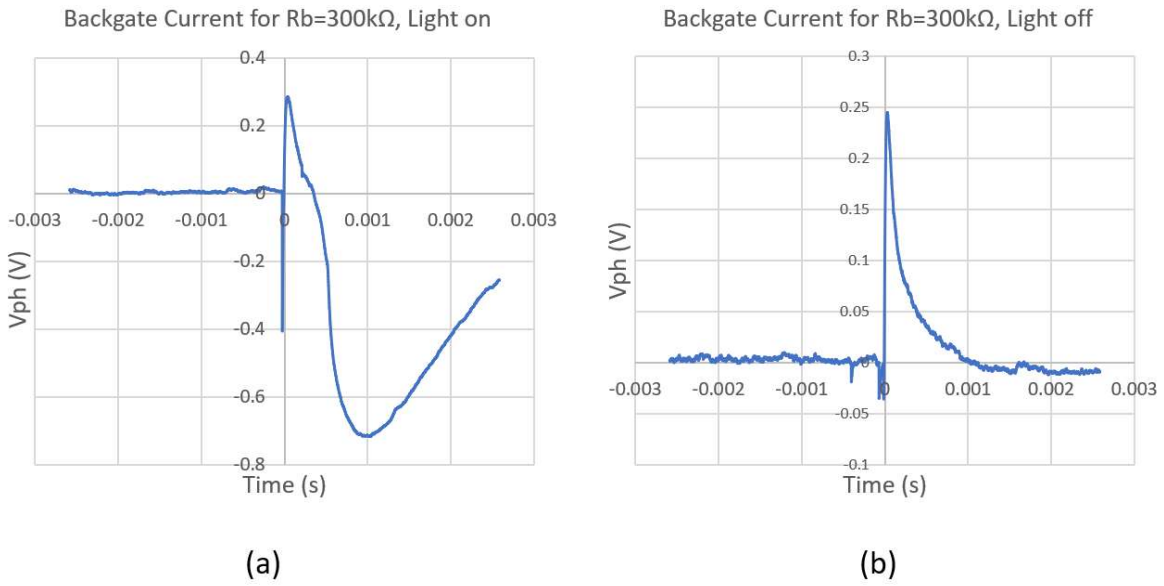


Figure 74: (a) Ejection back gate current under illumination with a biasing resistor of  $300\text{k}\Omega$ . The light is turned on at  $t=0$ s; (b) Injection backgate current after illumination is removed. The light is turned off at  $t=0$ s.

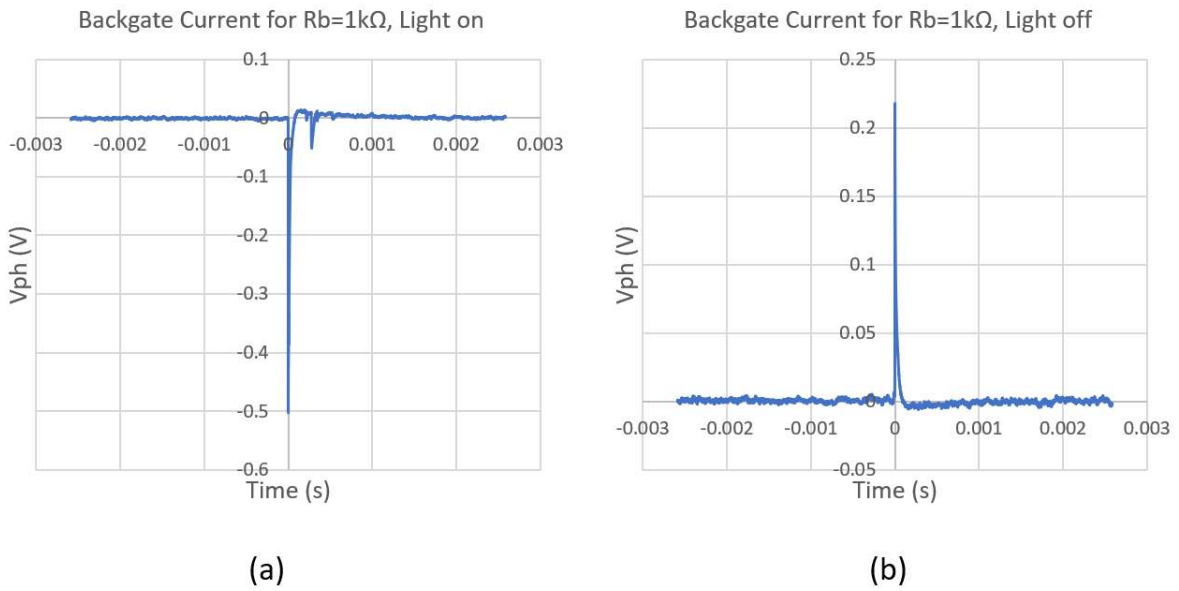


Figure 75: (a) Ejection back gate current under illumination with a biasing resistor of  $1\text{k}\Omega$ . The light is turned on at  $t=0$ s; (b) Injection backgate current after illumination is removed. The light is turned off at  $t=0$ s.

## 7. SIMULATIONS

### 7.1 Sentaurus Simulations

Sentaurus simulations are created to incorporate diffusion, bulk carrier recombination, and Fermi statistics into the metal oxide photoconduction model. These results will be used to verify the derivations of the above adsorption equations and determine if diffusion, bulk carrier recombination, and space charge region recombination and generation play a significant role in the photoresponse of metal oxides. Additionally, simulation in Sentaurus will provide a more accurate calculation of the carrier distribution in the space charge region. This will allow for calculation of the voltage drop across the oxide in the partially depleted case and therefore provide continuity of calculated current when transitioning between the completely depleted case and the partially depleted case. These simulations will be the basis for later studies on more complex devices.

A new material parameter file is created to represent ZnO. The material parameters used are shown in Table 24. The physics models used in the bulk are: Drift-Diffusion, Fermi statistics, and bulk SRH recombination. Illumination is implemented using the transfer matrix method (TMM). A simple light absorption model is used where the quantum yield model is *StepFunction(EffectiveBandGap)* and the optical intensity decays exponentially with the absorption constant shown in Table 24. A monochromatic source with the wavelength of interest, 340nm, is used to illuminate the surface of the metal oxide sample.

**Table 24: Bulk Material Parameters for Metal-Oxide Semiconductor material in Sentaurus.  $N_c$  and  $N_v$  are calculated from the density-of-states effective mass values from the equation given by [68] and the effective mass values  $m_n^* = 0.29$ ,  $m_p^* = 1.21$  given by [51].**

Parameter	Value
$\epsilon_r$	8.49 [97]
$\chi$ (eV)	4.5 [98]
$E_g$ (eV)	3.4 [99]
$N_c$ ( $cm^{-3}$ )	$1.76 \times 10^{17}$
$N_v$ ( $cm^{-3}$ )	$1.67 \times 10^{19}$
$\mu_n$ ( $cm^2/Vs$ )	205 [100]
$\mu_p$ ( $cm^2/Vs$ )	25
$N_D$ ( $cm^{-3}$ )	$1 \times 10^{17}$
$\alpha$ ( $cm^{-1}$ )	$9.145 \times 10^5$
$\tau_n$ (ns)	1 [101], [51]
$\tau_p$ (ns)	1 [101], [51]

Oxygen adsorption is modelled through interface traps. Listing 1 shows the code implemented to create Oxygen surface traps. An interface is created by placing a vacuum region adjacent to the metal oxide region in Sentaurus Device Editor (SDE). Thus, the physics at the interface of the metal oxide and vacuum can be defined in the Sentaurus Device (SDEVICE) file as shown in Listing 1. The trap type is defined as an acceptor so it is neutral when empty and negatively charged when filled with an electron. The oxygen trap has a single energy level which is assumed to be at the mid-gap, although future simulations should use an experimental value. The concentration of physically adsorbed oxygen molecules is represented by the Conc keyword and is set to  $1 \times 10^{15} cm^{-2}$ . The adsorption and desorption rate constants are defined by the capture cross section, *eXsection* and *hXsection*, and the thermal velocity. The thermal velocity is set to  $1 \times 10^7 cm/s$ , and the capture cross section is set to

$1 \times 10^{-17} \text{cm}^2$  to achieve adsorption and desorption rate constants of  $1 \times 10^{-10} \text{cm}^3/\text{s}$ . These settings are summarized in Table 25.

**Listing 1: Oxygen trap definition in sdevice file; region\_1 is the metal oxide and region\_2 is vacuum.**

```
Physics(RegionInterface="region_1/region_2"){
  Traps( Acceptor
    Level fromMidBandGap EnergyMid=0
    Conc=1E15
    eXsection=1e-17 hXsection=1e-17)
}
```

**Table 25: Interface material parameters for Metal-Oxide Semiconductor in Sentaurus.**

Parameter	Value
$E_T$ (eV)	1.7
$k_n$ (cm <sup>3</sup> /s)	$1 \times 10^{-10}$
$N_T$ (cm <sup>-2</sup> )	$1 \times 10^{15}$
Trap Type	Acceptor

In Sentaurus, the electron occupation of a trap,  $f^n$ , is given by the sum of the capture and emission rates,  $r_i^n$ :

$$\frac{\partial f^n}{\partial t} = \sum_i r_i^n \quad (241)$$

$$r_i^n = (1 - f^n)c_i^n - f^n e_i^n \quad (242)$$

where  $c_i^n$  is the capture rate and  $e_i^n$  is the emission rate. A similar equation is implemented for the hole occupation. There are four capture and emission rates: capture of an electron from the conduction band,  $c_c^n$ , capture of a hole from the valence band,  $c_v^p$ , emission of an electron to the conduction band,  $e_c^n$ , and the emission of a hole to the valence band,  $e_v^p$ :

$$c_c^n = \sigma_n v_{th}^n n \quad (243)$$

$$c_v^p = \sigma_p v_{th}^p p \quad (244)$$

$$e_c^n = \frac{v_{th} \sigma_n \gamma_n n_1}{g_n} \quad (245)$$

$$n_1 = N_C \exp\left(\frac{E_{trap} - E_C}{kT}\right) \quad (246)$$

$$\gamma_n = \frac{n}{N_C} \exp(-\eta_n) \quad (247)$$

$$\eta_n = \frac{E_{F,n} - E_C}{kT} \quad (248)$$

$$e_v^p = \frac{v_{th}^p \sigma_p \gamma_p p_1}{g_p} \quad (249)$$

$$\gamma_p = \frac{p}{N_V} \exp(-\eta_p) \quad (250)$$

$$\eta_p = \frac{E_V - E_{F,p}}{kT} \quad (251)$$

$$p_1 = N_V \exp\left(\frac{E_V - E_{trap}}{kT}\right) \quad (252)$$

where  $\sigma_n$  and  $\sigma_p$  are the electron and hole capture cross sections,  $g_n$  and  $g_p$  are degeneracy factors and are set to 1, and  $\gamma_n$  and  $\gamma_p$  are given by Fermi Statistics as shown in the equations above. These capture and emission rates are equivalent to (3) with the additional consideration of Fermi statistics.

An example device structure is shown in Figure 76. The device consists of the metal oxide material on  $\text{SiO}_2$ , two side contacts, and a backgate contact. The side contacts are ohmic with a 2D resistance of 0.001 Ohm/um. The backgate contact has a work function of 4.5eV so that the metal-

semiconductor work function is zero and the system is initially at flat band condition. The mesh size is on the order of the Debye length.

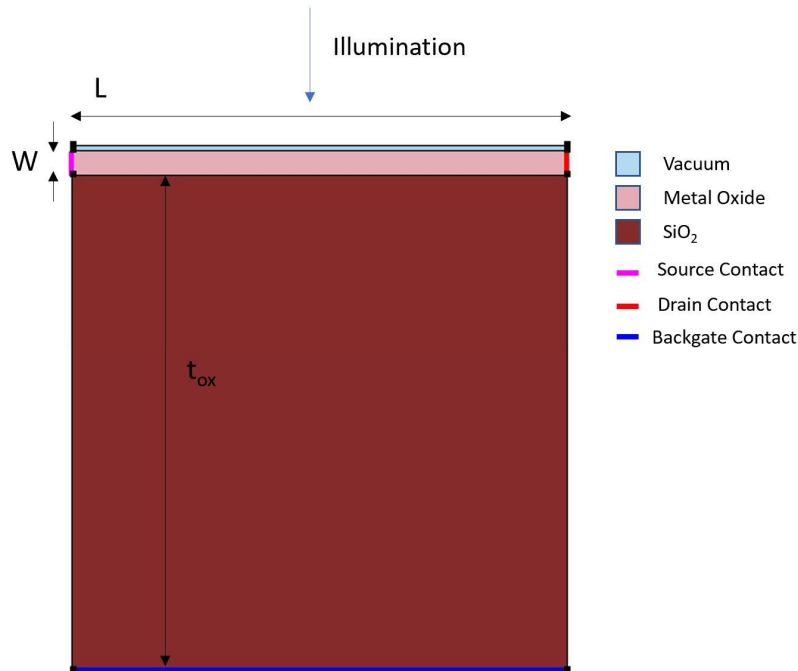


**Figure 76: Example metal oxide photoconductor structure with metal oxide width  $W=50\text{nm}$ , oxide thickness  $t_{\text{ox}}=1\mu\text{m}$ , device length  $l=1\mu\text{m}$ , and illumination at the surface of the device.**

The surface trap occupancy is simulated to examine the adsorption rate. The width of the device is  $1\mu\text{m}$  which is much larger than the maximum depletion width of approximately  $60\text{nm}$  so that the device remains partially depleted. The oxide substrate is removed so that there is no potential drop across the oxide. The simulation first solves the Poisson equation with the trap occupancy fixed to zero. Then the trap occupancy is allowed to change, and a transient simulation is started. The Backward Euler method is used to solve the transient so that fewer time steps are required to solve for the sudden large change in trap occupancy.

Figure 77 and Figure 78 show the results for two different rate constants. The value  $e\text{InterfaceTrappedCharge}$  is extracted from the Sentaurus simulations and is equivalent to  $q_c$ . The Matlab code uses the ode solver `ode15s` to solve Eqn. 46. Comparison of the two plots show similar results, confirming that this setup in Sentaurus does model adsorption in the expected way.

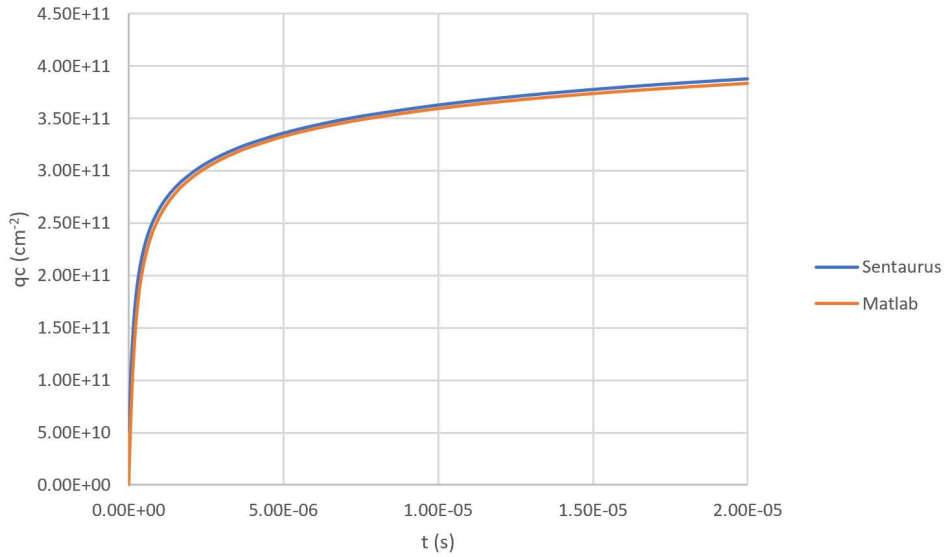


**Figure 77: Adsorption kinetics for  $k_n = 1 \times 10^{-14} \text{ cm}^3/\text{s}$  simulated in Matlab and Sentaurus.**

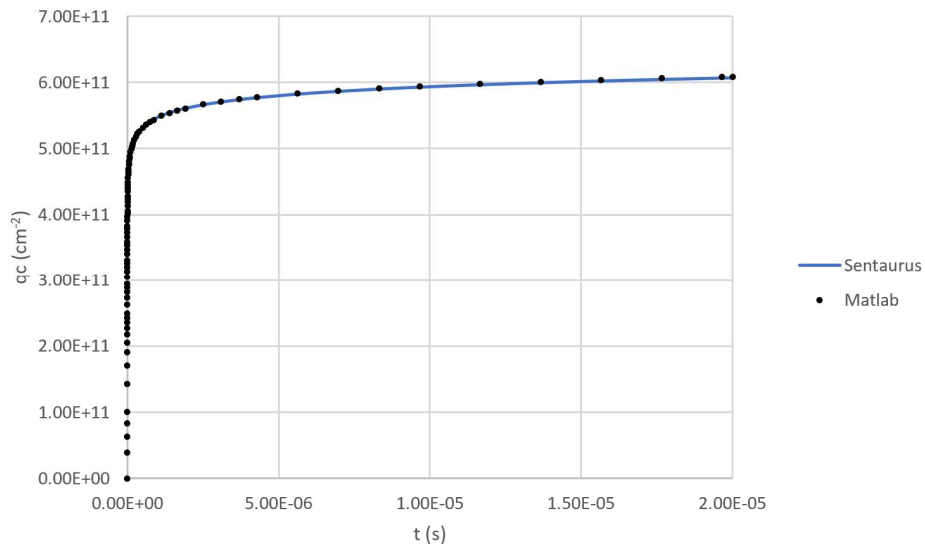


**Figure 78: Adsorption kinetics for  $k_n = 1 \times 10^{-10} \text{ cm}^3/\text{s}$  simulated in Matlab and Sentaurus.**

### 7.1.1 Partially Depleted Case

The dark and illuminated current for a partially depleted structure is simulated in Sentaurus and compared to Matlab calculations. Table 26 shows the settings for the simulation. The device width is sufficiently large to remain in the partially depleted regime, but small enough that the change in depletion width during illumination will cause a significant change in the current. The backgate contact is removed

to simulate a device with an infinitely large oxide thickness so that the oxide capacitance can be ignored. The bias is set to be relatively small to avoid a significant change in the adsorption rate across the length of the device. Initial adsorption is allowed to continue until  $q_c$  is sufficiently large to become sensitive to the given illumination intensity. The light intensity is set to be very large in order to reduce the simulation time. That is, for a smaller illumination intensity,  $t_{on}$  would need to be much larger to wait for  $q_c$  to be sufficiently large to be responsive to the light. For the given models, there is no difference in the simulation between using this high intensity illumination and a low intensity illumination. So, to demonstrate the photoresponse and compare to the previously derived equations, we will use the illumination intensity given in Table 26.

**Table 26: Device parameters and simulation settings for partially depleted simulation.**

$W$ ( $\mu m$ )	$t_{ox}$ ( $\mu m$ )	$l$ ( $\mu m$ )	$k_n$ ( $cm^3/s$ )	$V_{DS}$ (mV)	$I$ (W/cm <sup>2</sup> )	$t_{on}$ ( $\mu s$ )	$t_{off}$ ( $\mu s$ )
0.5	1	1	$1 \times 10^{-10}$	100	10	20	40

To simulate the current of the device with a voltage bias, the bias of the device is first ramped while the trap occupation is set to zero as shown in Listing 2.

**Listing 2: Solve section for Partially Depleted simulation**

```

Set(TrapFilling=Empty)
*- Build-up of initial solution:
NewCurrentPrefix="init_"
Coupled(Iterations=100){ Poisson }
Coupled{ Poisson Electron Hole }
NewCurrentFile="ramp"

*- Bias drain to target bias
Quasistationary(
  InitialStep=0.01 MinStep=1e-5 MaxStep=0.1
  Goal{ Name="Drain" Voltage= @Vds@ }
) { Coupled { Poisson Electron Hole } }

```

```

UnSet(TrapFilling)
NewCurrentFile="trans_"
Transient(
  InitialTime = 0
  FinalTime = @tf@
  MaxStep = @tstep@
){Coupled{Poisson Electron Hole}}

```

Figure 79 shows the results of the Sentaurus simulation and the accompanying MATLAB calculations. The curves show the characteristic fast and slow responses seen in metal oxide photoconductors. The simulated bandstructure prior to and during illumination is shown in Figure 80 and demonstrates the space charge region shrinking under illumination. The current simulated in Sentaurus has a similar order of magnitude of the dark current and photocurrent and similar rise and fall time to the calculated current. However, the simulated current differs in magnitude. This can be attributed to the approximation of the depletion width and electron distribution and a small difference in the calculated value of the adsorbed concentration in the Matlab calculations. The differences in the adsorbed concentration and depletion width are shown in Table 27 and Figure 81 which show the devices simulated in Sentaurus have a lower conductivity.

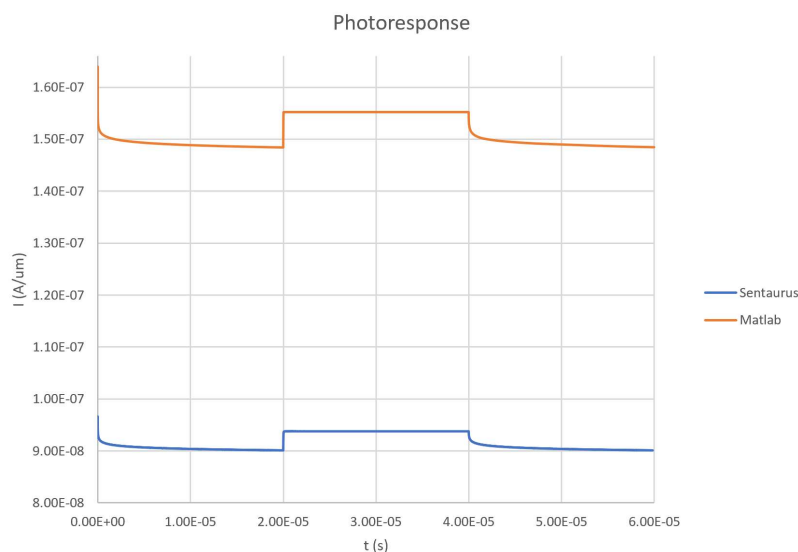


**Figure 79: Current measured from MATLAB and Sentaurus.**

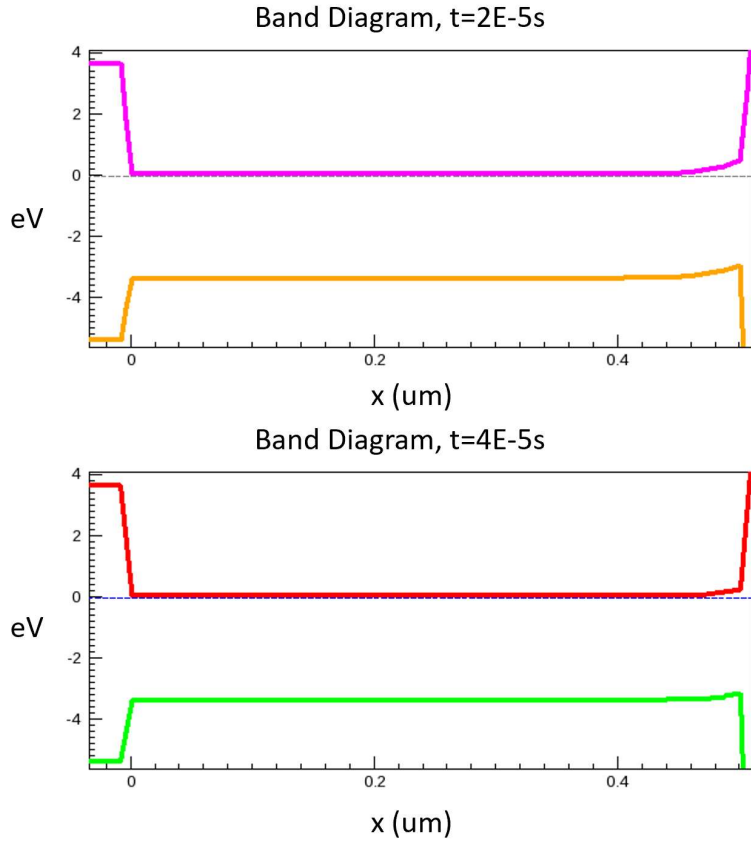
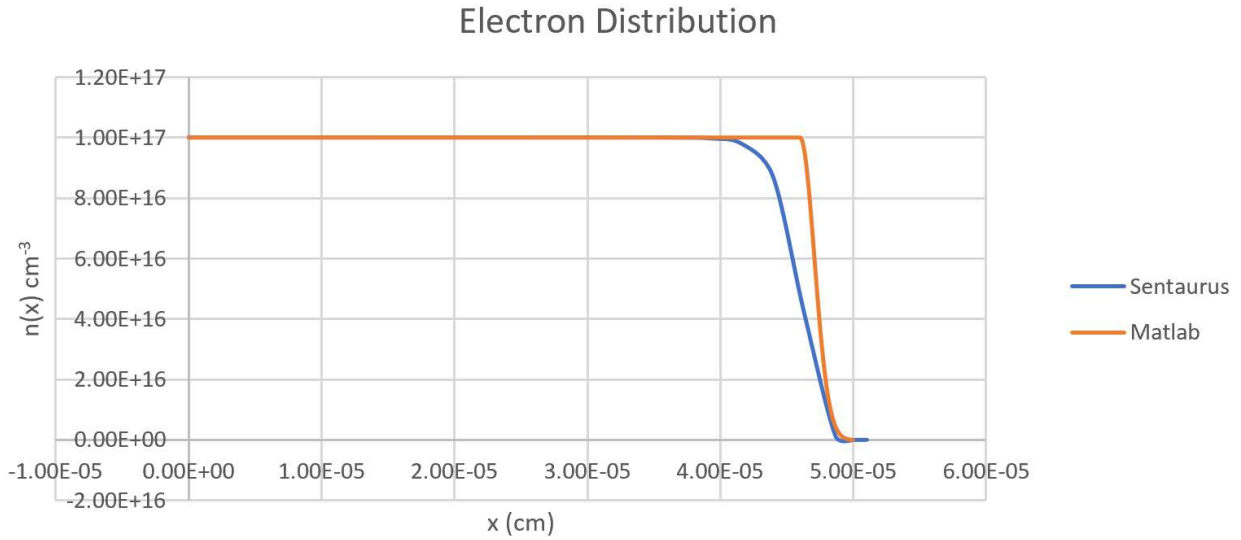


Figure 80: (top) Band diagram for device prior to illumination and (bottom) at steady-state adsorption during illumination. Oxide/metal oxide interface at  $x=0$  and metal oxide surface at  $0.5\mu\text{m}$ .

Table 27: Measured and calculated steady-state illumination values at  $t = 40\mu\text{s}$  for the simulation parameters shown in Table 26.

Parameter	Sentaurus	MATLAB
$q_c$ ( $\text{cm}^2$ )	$4.58822 \times 10^{11}$	$4.0175 \times 10^{11}$
$W_D$ (nm)	90*	40.175

\* Measured at  $\rho(x) = 0.01 * N_D$ .



**Figure 81: Electron distribution near the surface of the device. Oxide/Metal oxide interface at  $x=0$ , and air/metal oxide interface at  $x = 5 \times 10^{-5}$  cm.**

### 7.1.2 Injection and Ejection Current

To demonstrate the injection current, a simulation is created with the settings shown in Table 28. The device width is made sufficiently small to ensure that it will remain in complete depletion throughout the entire simulation. The oxide thickness is made very small to increase the initial adsorption rate so that adsorbed concentration will quickly become much greater than that at the onset of complete depletion. This reduces the simulation time significantly. The bias is set to 0V so that only the injection and ejection current is seen.

**Table 28: Settings for simulating injection current. The rise time refers to the rise time of the illumination pulse.**

Set	$W$ (nm)	$t_{ox}$ (nm)	$L$ ( $\mu$ m)	$k_n$ ( $cm^3$ /s)	$V_{DS}$ (V)	$I_{opt}$ (mW / $cm^2$ )	$t_{on}$ ( $\mu$ s)	$t_{off}$ ( $\mu$ s)	$t_{rise}$ (s)
1	25	10	1	$1 \times 10^{-10}$	0	10	20	40	$1 \times 10^{-9}$
2	25	10	1	$1 \times 10^{-10}$	0	10	20	40	$1 \times 10^{-5}$

Figure 82 shows the results of the simulation and calculations for the parameter Set 1 of Table 28.

To match the calculations to the simulation, the Matlab calculations and Sentaurus have the same  $q_c$

value at  $t=0$ . Their current values differ for the reasons discussed previously. The initial adsorption shows that the injection current decreases rapidly as the rate of adsorption slows. The illumination pulse causes a sharp increase in the current. As steady-state is reached under illumination, the current falls to zero. The current rises again as the illumination is turned off due to the sudden change in  $q_c$ .

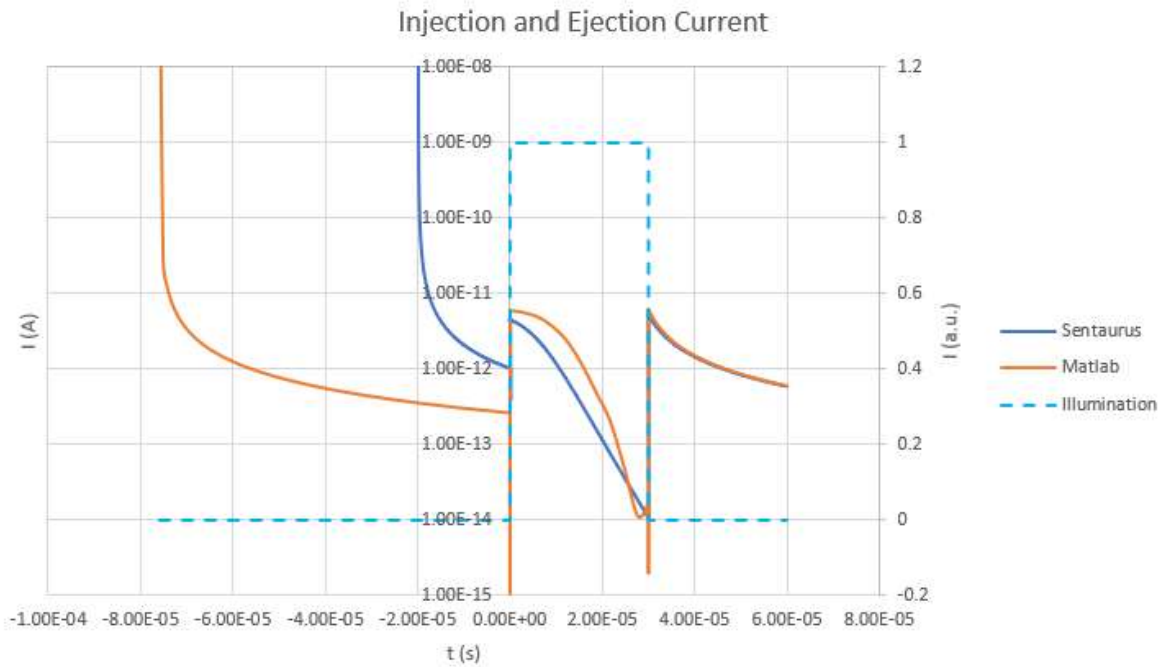


**Figure 82: Ejection and Injection current for settings in Set 1 of Table 28.**

The injection and ejection currents are dependent on the rise and fall time of the illumination pulse.

Figure 83 shows the results of parameter Set 2 of Table 28 which has an increased rise and fall time for the illumination pulse. The peak of the ejection current as measured in Sentaurus decreases from 4.5pA to 2.1pA.

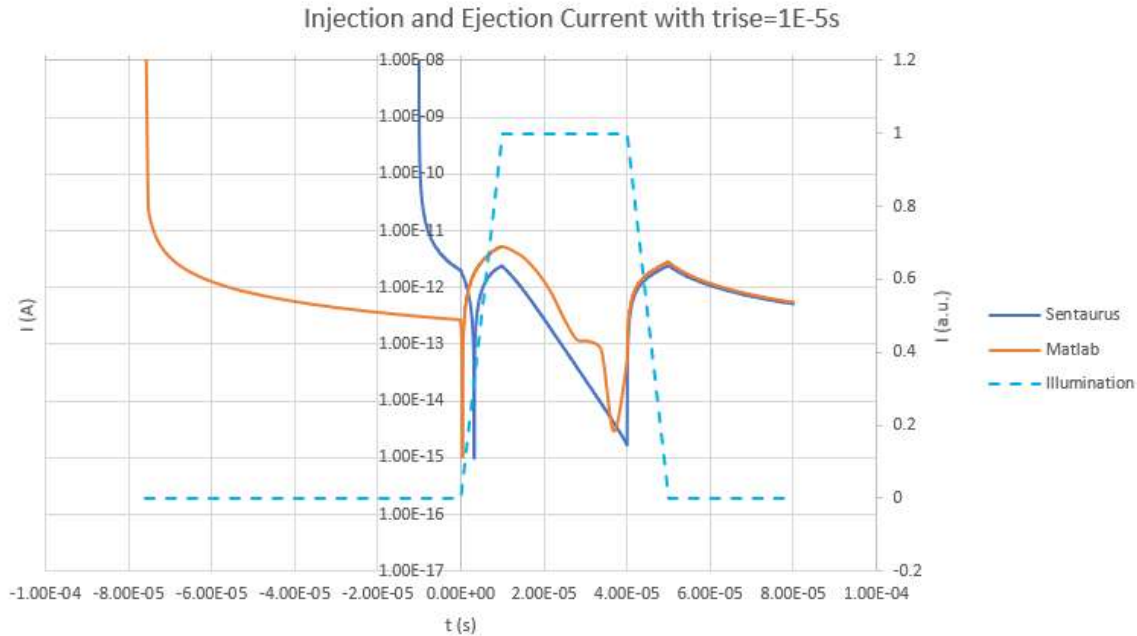


**Figure 83: Ejection and Injection current for the settings in Set 2 of Table 28.**

The injection and ejection currents are also dependent on the area of the device. As indicated by Eqn. 202 and 203, these currents are proportional to the length and depth of the device. Thus, even though these currents are on the order of picoamps in the above simulations, they can become very large with increase device dimensions.

### 7.1.3 Completely Depleted Case

A completely depleted device is simulated with the settings shown in Table 29. The resulting current plots are shown in Figure 84 and Figure 85 as simulated in Sentauros and calculated using the equations derived previously. The plots show the characteristic fast decay followed by a slow decay. There are also current spikes present at the start and end of illumination. These are from the injection and ejection current. The source and drain current differ because of the direction of the injection and ejection current. Under illumination, the electrons are ejected from both contacts, so the ejection current will add to the drain current and subtract from the source current. The calculations again predict currents larger than those simulated by Sentauros for the same reasons discussed previously. However, the

calculations have the same order of magnitude of the currents and rise and fall time as those simulated by Sentaurus.

**Table 29: Settings for completely depleted devices.**

Set	$W$ (nm)	$t_{ox}$ (nm)	$l$ ( $\mu m$ )	$k_n$ ( $cm^3/s$ )	$V_{DS}$ (mV)	$I$ ( $W/cm^2$ )	$t_{on}$ ( $\mu s$ )	$t_{off}$ ( $\mu s$ )	$t_{rise}$ (ns)
1	25	10	1	$1 \times 10^{-10}$	1	10	20	40	1
2	50	100	1	$1 \times 10^{-10}$	10	$1 \times 10^{-2}$	100	130	1

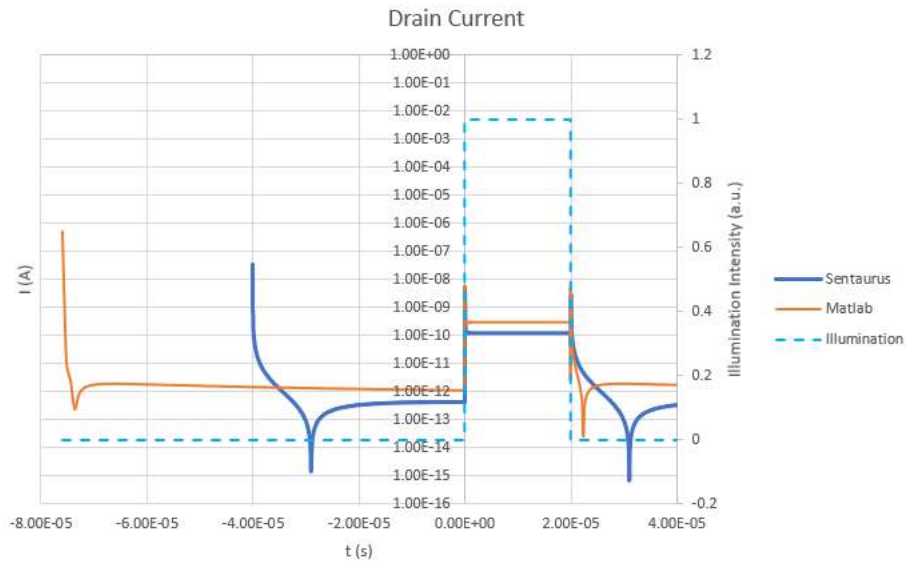


**Figure 84: Simulated and calculated drain current for metal oxide width of 25nm, oxide thickness 10nm, applied bias 1mV, and intensity of illumination of 10W/cm<sup>2</sup>. The rise and fall time of the illumination pulse is 1ns.**

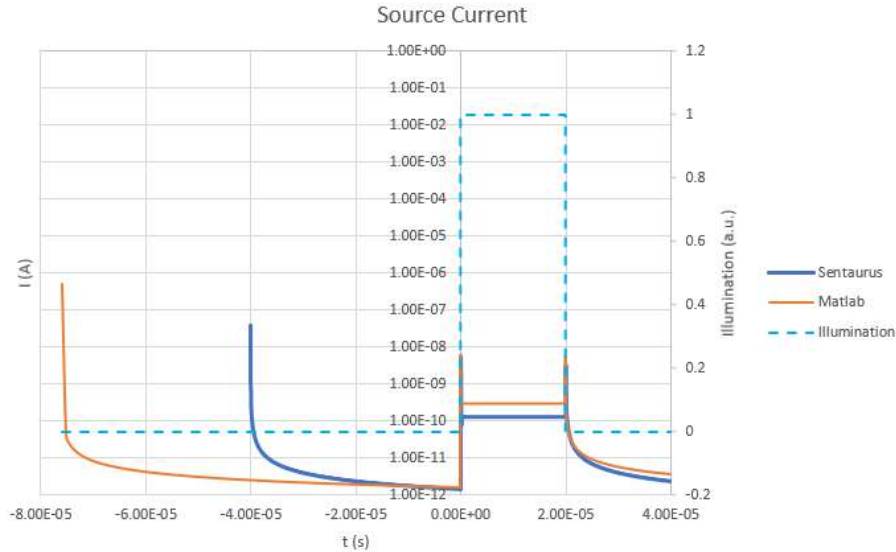


**Figure 85: Simulated and calculated source current for metal oxide width of 25nm, oxide thickness 10nm, applied bias 1mV, and intensity of illumination of 10W/cm<sup>2</sup>. The rise and fall time of the illumination pulse is 1ns.**

A more realistic situation is simulated with the settings in Table 29. The metal oxide and oxide thickness are significantly larger, and the illumination intensity is decreased to 10mW/cm<sup>2</sup>. The bias voltage is increased to overcome any ejection and injection currents. Figure 86 shows the results on a linear scale. Both curves show the characteristic fast decay followed by a slow decay. The magnitudes of currents and response times are again similar for both with the calculated current being about 3.5 times larger than that simulated in Sentaurus. The calculated current shows a peak in the photocurrent not present in the Sentaurus simulation and not related to the ejection current. This can be attributed to an overshoot of the surface potential past its equilibrium value. Such a peak in the current can be observed in many experimental results metal oxide photodetectors [102], [103], [104], [105].

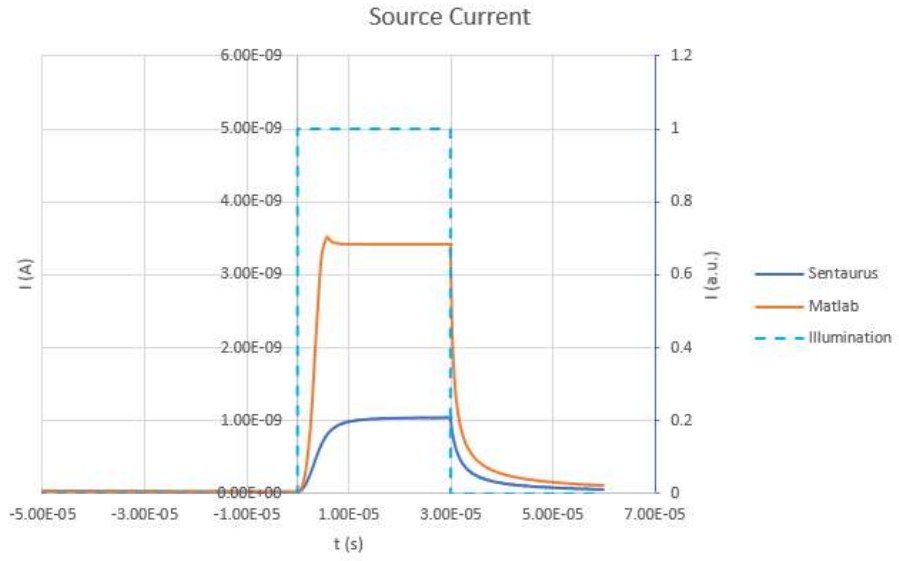


**Figure 86: Simulated and calculated current for parameter Set 2 in Table 29.**

## 8. CONCLUSIONS

In this thesis, new adsorption and photodesorption equations have been derived to describe the photoresponse of metal oxide photodetectors based on material properties, morphology, and device geometry. These equations expand metal oxide adsorption modeling beyond the basic bulk planar equations and enable us to predictively model the photoresponse of modern device structures such as thin films and nanostructures. The figures of merits used to characterize photoconductor devices have also been redefined to accurately portray device performance. A new figure of merit, the voltage photoresponsivity, is defined to characterize the photoconductor signal. The minimum detectable optical power is also redefined based on the adsorption rate.

These new adsorption models and a critical analysis of photoconductor figures of merit indicate the direction metal oxide photodetector design should take to achieve the target metrics for bacterial fluorescence detection (BFD) applications. The major limiting factor in designing a sensor for BFD applications is identified as the slow response time under low illumination intensities. To overcome this, two new device structures are proposed: a backgate-controlled completely depleted device, and a zero-bias capacitive mode device. In the former, the backgate of a thin-film device on insulator can be used to control the adsorption rate and therefore the device response time and minimum detectable optical power. In the latter, the current between the metal backgate and metal oxide surface of a CD device can be measured to decrease the response time of the device at very low optical powers.

A CD device was fabricated using a ZnO sol-gel thin film on a thermal oxide Si wafer. We confirm that the backgate can be used to control the adsorption rate of the device. A positive bias is used to reduce the photodecay response time. The same device is used to confirm the existence of backgate current in capacitive mode. Both of these device structures could be used to enable BFD detection.

The adsorption and photodesorption models presented in this thesis are consistent with many experimental measurements of metal oxide photocurrents. However, until the adsorption rate constants for

metal oxide surface are measured, it is difficult to fit the models to experimental data and compare their validity. The models created in this thesis also have limitations and should be applied with them in mind. In all photodesorption equations, the holes are assumed to reach the surface effectively instantaneously. While this assumption is generally sufficient for holes generated in the depletion width, it may not be for holes generated in the bulk which must diffuse to the surface. No quantum effects are included. For example, electron tunneling across the insulator of CD device is not accounted for, and ballistic transport in nanostructures is not considered. Mobility changes due to scattering at the insulating semiconductor-insulator interface in CD devices is not considered. In Section 3.9.2, bandgap differences and interfacial charge between materials is not considered. In our noise calculations in Section 4, shot noise and flicker noise are not included. Finally, dielectric breakdown of the insulating oxide and metal oxide in CD devices is not considered.

In addition to describing the photoresponse of metal oxide photodetectors, the adsorption and photodesorption rate equations derived in this thesis have many additional potential applications. The adsorption models apply to any semiconductor device with any kind of surface trap. These models could be particularly useful in other semiconductors with gaseous adsorbates such as nitrides and sulfides. These models could also be applied to gas sensors and photo-activated gas sensors. Section 3.10 would be particularly helpful in describing the effect of multiple gaseous adsorbates on gas sensor conductivity. These models also indicate that adsorption and photodesorption can have a significant impact on measurements and characterization. For example, many measurements of the bulk minority carrier lifetime in metal oxide semiconductors have been measured in ambient [9], [11], [106]. Thus, photodesorption and adsorption likely contribute significantly to the photocurrent and the current cannot be described as an exponential decay with a time constant given by the carrier lifetime. These measurements should be taken in an inert atmosphere or with a passivated surface. Time-resolved photoluminescence measurements (TRPL) use UV light to measure photoluminescence. It is common to correlate the luminescence with the concentration of adsorbates on the surface or to attribute emissions to

bulk states. However, based on the models presented in this thesis, UV light will change the adsorbed concentration and green photoluminescent emissions are set by the number of carriers that recombine at the surface. Thus, the interpretations of these measurements should be reconsidered; the photoluminescent measurements are not necessarily proportional to the adsorbed concentration of gases. Furthermore, it may be that many emissions labeled as ‘bulk’ emissions are actually ‘surface’ emissions. To differentiate between bulk and surface emissions, the TRPL measurements should be performed in both inert and ambient atmosphere.

The adsorption rate constants of different faces of metal oxide semiconductors need to be measured to employ this model. There have been very few measurements of these values and there is not a standard method of measurement. In this thesis, we have proposed two new possible methods for measurement. The minority carrier lifetime of metal oxides must be accurately measured. As previously discussed, most measurements are taken in ambient and may therefore be incorrect. This parameter is important in comparing the adsorption-based photoresponse to that of bulk recombination and generation. It may be that the bulk photoresponse has better performance. The heterojunction adsorption models need to be expanded on to include the effect of band gap differences and interfacial charge. Many of the modern metal oxide photodetectors employ a heterojunction, and so having accurate models for them is important. A new shot noise term must be derived for adsorption-based photoconductors. This term is essential for predicting the SNR of metal oxide photodetectors.

## REFERENCES

- [1] L. R. Dartnell, T. A. Roberts, G. Moore, J. M. Ward, and J.-P. Muller, “Fluorescence characterization of clinically-important bacteria,” *PloS One*, vol. 8, no. 9, Sep. 2013, Art. no. e75270.
- [2] P. W. Stone, D. Braccia, and E. Larson, “Systematic review of economic analyses of health care-associated infections,” *Am. J. Infect. Control*, vol. 33, no. 9, pp. 501–509, Nov. 2005.
- [3] M. C. Layton, M. Perez, P. Heald, and J. E. Patterson, “An outbreak of mupirocin-resistant *Staphylococcus aureus* on a dermatology ward associated with an environmental reservoir,” *Infect. Control Hosp. Epidemiol.*, vol. 14, no. 7, pp. 369–375, Jul. 1993.
- [4] F. A. Manian, L. Meyer, and J. Jenne, “*Clostridium difficile* contamination of blood pressure cuffs: a call for a closer look at gloving practices in the era of universal precautions,” *Infect. Control Hosp. Epidemiol.*, vol. 17, no. 3, pp. 180–182, Mar. 1996.
- [5] J. Lakowicz, *Principles of Fluorescence Spectroscopy*, 3rd ed. Baltimore, MD, USA: Springer, 2006.
- [6] J. Bartram, J. Cotruvo, M. Exner, C. Fricker, and A. Glasmacher, Eds., *Heterotrophic Plate Counts and Drinking-Water Safety: the Significance of HPCs for Water Quality and Human Health*. London, UK: IWA Publishing, 2003.
- [7] S. Prachi, “Metal oxide nanostructure based ultraviolet photodetectors for smart lighting applications,” Ph.D dissertation, Dept. Elect. and Computer Syst. Eng., Rensselaer Polytechnic Institute, Troy, 2018.
- [8] D. A. Melnick, “Zinc oxide photoconduction, an oxygen adsorption process,” *J. Chem. Phys.*, vol. 26, no. 5, pp. 1136–1146, May 1957.
- [9] C. Soci *et al.*, “ZnO nanowire UV photodetectors with high internal gain,” *Nano Lett.*, vol. 7, no. 4, pp. 1003–1009, Apr. 2007.
- [10] P. Sharma and S. Sawyer, “A high responsivity SnO<sub>2</sub> hollow nanospheres based ultraviolet photodetector,” in *Lester Eastman Conf.*, Aug. 2016, pp. 46–49.
- [11] D. Shao *et al.*, “Organic–inorganic heterointerfaces for ultrasensitive detection of ultraviolet light,” *Nano Lett.*, vol. 15, no. 6, pp. 3787–3792, Jun. 2015.
- [12] D. Shao, M. Yu, H. Sun, G. Xin, J. Lian, and S. Sawyer, “High-Performance Ultraviolet Photodetector Based on Organic–Inorganic Hybrid Structure,” *ACS Appl. Mater. Interfaces*, vol. 6, no. 16, pp. 14690–14694, Aug. 2014.
- [13] D. Shao *et al.*, “Flexible, thorn-like ZnO-multiwalled carbon nanotube hybrid paper for efficient ultraviolet sensing and photocatalyst applications,” *Nanoscale*, vol. 6, no. 22, pp. 13630–13636, Oct. 2014.
- [14] D. Shao, M. Yu, H. Sun, T. Hu, J. Lian, and S. Sawyer, “High responsivity, fast ultraviolet photodetector fabricated from ZnO nanoparticle–graphene core–shell structures,” *Nanoscale*, vol. 5, no. 9, pp. 3664–3667, Apr. 2013.
- [15] D. Shao *et al.*, “ZnO quantum dots-graphene composite for efficient ultraviolet sensing,” *Mater. Lett.*, vol. 112, pp. 165–168, Dec. 2013.
- [16] D. Shao *et al.*, “A high performance UV–visible dual-band photodetector based on an inorganic Cs<sub>2</sub>SnI<sub>6</sub> perovskite/ZnO heterojunction structure,” *J. Mater. Chem. C*, vol. 8, no. 5, pp. 1819–1825, Feb. 2020.
- [17] D. Shao, W. Zhu, G. Xin, J. Lian, and S. Sawyer, “Inorganic vacancy-ordered perovskite Cs<sub>2</sub>SnCl<sub>6</sub>:Bi/GaN heterojunction photodiode for narrowband, visible-blind UV detection,” *Appl. Phys. Lett.*, vol. 115, no. 12, Sep. 2019, Art. no. 121106.
- [18] D. Shao *et al.*, “Ultrasensitive UV photodetector based on interfacial charge-controlled inorganic perovskite–polymer hybrid structure,” *ACS Appl. Mater. Interfaces*, vol. 12, no. 38, pp. 43106–43114, Sep. 2020.

- [19] “UV-A Sensor GUVA-T11GD.” GenUV, 2018. Accessed: Apr. 04, 2022. [Online]. Available: [www.geni-uv.com/download/products/GUVA-T11GD.pdf](http://www.geni-uv.com/download/products/GUVA-T11GD.pdf)
- [20] “SiC-Photodiode with integrated UV-filter: JEA0.1A, JEA0.1B, JEA0.1C.” Electro Optical Components, Inc., Aug. 2018. Accessed: Apr. 04, 2022. [Online]. Available: <https://eoc-inc.com/wp-content/uploads/2019/04/JEA-01-ABC.pdf>
- [21] “UV/Visible Sensor GVGR-S11SD.” Electro Optical Components, Inc. Accessed: Apr. 04, 2022. [Online]. Available: <https://www.eoc-inc.com/wp-content/uploads/GVGR-S11SD.pdf>
- [22] “APD Module C5331 Series.” Hamamatsu. Accessed: Apr. 04, 2022. [Online]. Available: <https://dtsheet.com/doc/749659/hamamatsu-c5331-04>
- [23] A. H. Peterson and S. M. Sawyer, “Oxygen adsorption and photoconduction models for metal oxide semiconductors: a review,” *IEEE Sens. J.*, vol. 21, no. 15, pp. 16409–16427, Aug. 2021.
- [24] W. H. Brattain and J. Bardeen, “Surface properties of germanium,” *Bell Syst. Tech. J.*, vol. 32, no. 1, pp. 1–41, Jan. 1953.
- [25] W. H. Brattain, “Evidence for surface states on semiconductors from change in contact potential on illumination,” *Phys. Rev.*, vol. 72, no. 4, p. 345, Jul. 1947.
- [26] C. G. B. Garrett and W. H. Brattain, “Distribution and cross-sections of fast states on germanium surfaces,” *Bell Syst. Tech. J.*, vol. 35, no. 5, pp. 1041–1058, May 1956.
- [27] W. H. Brattain, “Physical theory of semiconductor surfaces,” *Phys. Rev.*, vol. 99, no. 2, pp. 376–387, Dec. 1955.
- [28] J. C. Moore and C. V. Thompson, “A phenomenological model for the photocurrent transient relaxation observed in ZnO-based photodetector devices,” *Sensors*, vol. 13, no. 8, pp. 9921–9940, Aug. 2013.
- [29] D. Cammi, “Photoconductivity and gas sensing properties of ZnO nanowire devices,” Ph.D dissertation, Friedrich-Schiller University of Jena, Jena, Germany, 2016.
- [30] J. Bao *et al.*, “Photoinduced oxygen release and persistent photoconductivity in ZnO nanowires,” *Nanoscale Res. Lett.*, vol. 6, no. 1, p. 404, May 2011.
- [31] S. R. Morrison, *The Chemical Physics of Surfaces*. Boston, MA, USA: Springer, 2013.
- [32] D. B. Medved, “Photoconductivity and chemisorption kinetics in sintered zinc oxide semiconductor,” *J. Phys. Chem. Solids*, vol. 20, no. 3, pp. 255–267, Aug. 1961.
- [33] S. R. Morrison, “Surface barrier effects in adsorption, illustrated by zinc oxide,” in *Advances in Catalysis*, vol. 7, W. G. Frankenburg, V. I. Komarewsky, and E. K. Rideal, Eds. Academic Press, 1955, pp. 259–301.
- [34] H. Van Hove and A. Luyckx, “Photoconductivity decay of ZnO crystals in oxygen,” *Solid State Commun.*, vol. 4, no. 11, pp. 603–606, Nov. 1966.
- [35] S. Dhara and P. Giri, “Enhanced UV photosensitivity from rapid thermal annealed vertically aligned ZnO nanowires,” *Nanoscale Res. Lett.*, vol. 6, no. 1, p. 504, Aug. 2011.
- [36] Q. H. Li, T. Gao, Y. G. Wang, and T. H. Wang, “Adsorption and desorption of oxygen probed from ZnO nanowire films by photocurrent measurements,” *Appl. Phys. Lett.*, vol. 86, no. 12, Mar. 2005, Art. no. 123117.
- [37] W. Göpel, “Reactions of oxygen with ZnO–10 $\bar{1}0$ -surfaces,” *J. Vac. Sci. Technol.*, vol. 15, no. 4, p. 1298, Jun. 1998.
- [38] P. Esser and W. Göpel, “‘Physical’ adsorption on single crystal zinc oxide,” *Surf. Sci.*, vol. 97, no. 2, pp. 309–318, Jul. 1980.
- [39] B. F. Spencer *et al.*, “Time-resolved surface photovoltage measurements at n-type photovoltaic surfaces: Si(111) and ZnO(10 $\bar{1}0$ ),” *Phys. Rev. B*, vol. 88, no. 19, Nov. 2013, Art. no. 195301.
- [40] R. Yukawa *et al.*, “Electron-hole recombination on ZnO(0001) single-crystal surface studied by time-resolved soft X-ray photoelectron spectroscopy,” *Appl. Phys. Lett.*, vol. 105, no. 15, Oct. 2014, Art. no. 151602.
- [41] V. Q. Dang *et al.*, “Ultrahigh responsivity in graphene–ZnO nanorod hybrid UV photodetector,” *Small*, vol. 11, no. 25, pp. 3054–3065, Feb. 2015.

- [42] Z. Ke, Z. Yang, M. Wang, M. Cao, Z. Sun, and J. Shao, “Low temperature annealed ZnO film UV photodetector with fast photoresponse,” *Sens. Actuators Phys.*, vol. 253, pp. 173–180, Jan. 2017.
- [43] X. Liu, L. Gu, Q. Zhang, J. Wu, Y. Long, and Z. Fan, “All-printable band-edge modulated ZnO nanowire photodetectors with ultra-high detectivity,” *Nat. Commun.*, vol. 5, no. 1, Art. no. 1, Jun. 2014.
- [44] J. Nahlik, A. Laposa, J. Voves, J. Kroutil, J. Drahoukoupil, and M. Davydova, “A high sensitivity UV photodetector with inkjet printed ZnO/nanodiamond active layers,” *IEEE Sens. J.*, vol. 19, no. 14, pp. 5587–5593, Jul. 2019.
- [45] L. Kronik and Y. Shapira, “Surface photovoltage phenomena: theory, experiment, and applications,” *Surf. Sci. Rep.*, vol. 37, no. 1, pp. 1–206, Dec. 1999.
- [46] H. Zhang *et al.*, “Characterization and modeling of a ZnO nanowire ultraviolet photodetector with graphene transparent contact,” *J. Appl. Phys.*, vol. 114, no. 23, Dec. 2013, Art. no. 234505.
- [47] B. D. Boruah, A. Mukherjee, and A. Misra, “Sandwiched assembly of ZnO nanowires between graphene layers for a self-powered and fast responsive ultraviolet photodetector,” *Nanotechnology*, vol. 27, no. 9, Feb. 2016, Art. no. 095205.
- [48] M. A. Reshchikov, M. Foussekis, and A. A. Baski, “Surface photovoltage in undoped n-type GaN,” *J. Appl. Phys.*, vol. 107, no. 11, pp. 1–13, Mar. 2010.
- [49] N. Barsan and U. Weimar, “Conduction model of metal oxide gas sensors,” *J. Electroceramics*, vol. 7, no. 3, pp. 143–167, Dec. 2001.
- [50] L. R. Covington and J. C. Moore, “Photoconductivity and transient response of Al:ZnO:Al planar structures fabricated via a thermal oxidation process,” *Thin Solid Films*, vol. 540, pp. 106–111, Jul. 2013.
- [51] Ü. Özgür *et al.*, “A comprehensive review of ZnO materials and devices,” *J. Appl. Phys.*, vol. 98, no. 4, Aug. 2005, Art. no. 041301.
- [52] W. Li *et al.*, “Characterization of photovoltage evolution of ZnO films using a scanning Kelvin probe system,” *Phys. B Condens. Matter*, vol. 404, no. 16, pp. 2197–2201, Aug. 2009.
- [53] A. B. Djurišić, A. M. C. Ng, and X. Y. Chen, “ZnO nanostructures for optoelectronics: Material properties and device applications,” *Prog. Quantum Electron.*, vol. 34, no. 4, pp. 191–259, Jul. 2010.
- [54] S. R. Morrison, “Measurement of surface state energy levels of one-equivalent absorbates on ZnO,” *Surf. Sci.*, vol. 27, no. 3, pp. 586–604, Oct. 1971.
- [55] J. A. Röhr, J. Sá, and S. J. Konezny, “The role of adsorbates in the green emission and conductivity of zinc oxide,” *Commun. Chem.*, vol. 2, no. 1, Art. no. 1, May 2019.
- [56] V. Srikant and D. R. Clarke, “On the optical band gap of zinc oxide,” *J. Appl. Phys.*, vol. 83, no. 10, pp. 5447–5451, May 1998.
- [57] D. P. Norton *et al.*, “ZnO: growth, doping & processing,” *Mater. Today*, vol. 7, no. 6, pp. 34–40, Jun. 2004.
- [58] R. Khokhra, B. Bharti, H.-N. Lee, and R. Kumar, “Visible and UV photo-detection in ZnO nanostructured thin films via simple tuning of solution method,” *Sci. Rep.*, vol. 7, no. 1, Nov. 2017, Art. no. 15032.
- [59] P. S. Shewale, N. K. Lee, S. H. Lee, K. Y. Kang, and Y. S. Yu, “Ti doped ZnO thin film based UV photodetector: Fabrication and characterization,” *J. Alloys Compd.*, vol. 624, pp. 251–257, Mar. 2015.
- [60] L. Su *et al.*, “High-performance zero-bias ultraviolet photodetector based on p-GaN/n-ZnO heterojunction,” *Appl. Phys. Lett.*, vol. 105, no. 7, Aug. 2014, Art. no. 072106.
- [61] D. Shao, H. Sun, G. Xin, J. Lian, and S. Sawyer, “High quality ZnO–TiO<sub>2</sub> core–shell nanowires for efficient ultraviolet sensing,” *Appl. Surf. Sci.*, vol. 314, pp. 872–876, Sep. 2014.
- [62] S. Mridha and D. Basak, “Ultraviolet and visible photoresponse properties of n-ZnO/p-Si heterojunction,” *J. Appl. Phys.*, vol. 101, no. 8, Apr. 2007, Art. no. 083102.
- [63] K. Liu, M. Sakurai, and M. Aono, “ZnO-Based Ultraviolet Photodetectors,” *Sensors*, vol. 10, no. 9, Art. no. 9, Sep. 2010.

- [64] J. Chen, W. Ouyang, W. Yang, J.-H. He, and X. Fang, “Recent progress of heterojunction ultraviolet photodetectors: materials, integrations, and applications,” *Adv. Funct. Mater.*, vol. 30, no. 16, Feb. 2020, Art. no. 1909909.
- [65] C. H. Xu, H. F. Lui, and C. Surya, “Optical and sensor properties of ZnO nanostructure grown by thermal oxidation in dry or wet nitrogen,” *J. Electroceramics*, vol. 28, no. 1, pp. 27–33, Feb. 2012.
- [66] C.-C. Huang, B. D. Pelatt, and J. F. Conley, “Directed integration of ZnO nanobridge sensors using photolithographically patterned carbonized photoresist,” *Nanotechnology*, vol. 21, no. 19, Apr. 2010, Art. no. 195307.
- [67] W. Yan, N. Mechau, H. Hahn, and R. Krupke, “Ultraviolet photodetector arrays assembled by dielectrophoresis of ZnO nanoparticles,” *Nanotechnology*, vol. 21, no. 11, Feb. 2010, Art. no. 115501.
- [68] S. M. Sze and N. K. Kwok, *Physics of Semiconductor Devices*, 3rd ed. Hoboken, NJ, USA: Wiley, 2006.
- [69] Y. Li, F. Della Valle, M. Simonnet, I. Yamada, and J.-J. Delaunay, “Competitive surface effects of oxygen and water on UV photoresponse of ZnO nanowires,” *Appl. Phys. Lett.*, vol. 94, no. 2, Jan. 2009, Art. no. 023110.
- [70] B. Meyer *et al.*, “Partial Dissociation of Water Leads to Stable Superstructures on the Surface of Zinc Oxide,” *Angew. Chem. Int. Ed.*, vol. 43, no. 48, pp. 6641–6645, Dec. 2004.
- [71] B. Pallab, *Semiconductor Optoelectronic Devices*, 2nd edition. India: Pearson, 2017.
- [72] “OPA627 and OPA637 Precision High-Speed Difet Operational Amplifiers.” Texas Instruments, 2015. Accessed: Apr. 25, 2022. [Online]. Available: [https://www.ti.com/lit/ds/symlink/opa627.pdf?ts=1648558344911&ref\\_url=https%253A%252F%252Fwww.ti.com%252Fproduct%252FOPA627](https://www.ti.com/lit/ds/symlink/opa627.pdf?ts=1648558344911&ref_url=https%253A%252F%252Fwww.ti.com%252Fproduct%252FOPA627)
- [73] T. Zhai *et al.*, “A comprehensive review of one-dimensional metal-oxide nanostructure photodetectors,” *Sensors*, vol. 9, no. 8, pp. 6504–6529, Aug. 2009.
- [74] D. Nunes *et al.*, “Metal oxide nanostructures for sensor applications,” *Semicond. Sci. Technol.*, vol. 34, no. 4, Mar. 2019, Art. no. 043001.
- [75] M. Osada and T. Sasaki, “Two-dimensional dielectric nanosheets: novel nanoelectronics from nanocrystal building blocks,” *Adv. Mater.*, vol. 24, no. 2, pp. 210–228, Oct. 2012.
- [76] “Tin Dioxide (SnO<sub>2</sub>) Semiconductors,” *AZoM.com*, Apr. 10, 2013. <https://www.azom.com/article.aspx?ArticleID=8456> (accessed Mar. 29, 2022).
- [77] J. W. Hodby, T. E. Jenkins, C. Schwab, H. Tamura, and D. Trivich, “Cyclotron resonance of electrons and of holes in cuprous oxide, Cu<sub>2</sub>O,” *J. Phys. C Solid State Phys.*, vol. 9, no. 8, pp. 1429–1439, Apr. 1976.
- [78] M. Passlack *et al.*, “Ga<sub>2</sub>O<sub>3</sub> films for electronic and optoelectronic applications,” *J. Appl. Phys.*, vol. 77, no. 2, pp. 686–693, Jan. 1995.
- [79] A. Fiedler, R. Schewski, Z. Galazka, and K. Irmscher, “Static dielectric constant of  $\beta$ -Ga<sub>2</sub>O<sub>3</sub> perpendicular to the principal planes (100), (010), and (001),” *ECS J. Solid State Sci. Technol.*, vol. 8, no. 7, pp. Q3083–Q3085, Mar. 2019.
- [80] M. Stokoy *et al.*, “Optical phonon modes, static and high-frequency dielectric constants, and effective electron mass parameter in cubic In<sub>2</sub>O<sub>3</sub>,” *J. Appl. Phys.*, vol. 129, no. 22, Jun. 2021, Art. no. 225102.
- [81] H. Köstlin, R. Jost, and W. Lems, “Optical and electrical properties of doped In<sub>2</sub>O<sub>3</sub> films,” *Phys. Status Solidi A*, vol. 29, no. 1, pp. 87–93, Dec. 1975.
- [82] S. G. Choi, J. Zúñiga-Pérez, V. Muñoz-Sanjosé, A. G. Norman, C. L. Perkins, and D. H. Levi, “Complex dielectric function and refractive index spectra of epitaxial CdO thin film grown on r-plane sapphire from 0.74 to 6.45 eV,” *J. Vac. Sci. Technol. B*, vol. 28, no. 6, pp. 1120–1124, Nov. 2010.
- [83] N. I. Santha *et al.*, “Effect of doping on the dielectric properties of cerium oxide in the microwave and far-infrared frequency range,” *J. Am. Ceram. Soc.*, vol. 87, no. 7, pp. 1233–1237, Jun. 2004.

- [84] M. B. Johansson *et al.*, “Electronic and optical properties of nanocrystalline WO<sub>3</sub> thin films studied by optical spectroscopy and density functional calculations,” *J. Phys. Condens. Matter*, vol. 25, no. 20, Apr. 2013, Art. no. 205502.
- [85] H. K. Yadav, K. Sreenivas, and V. Gupta, “Study of metal/ZnO based thin film ultraviolet photodetectors: The effect of induced charges on the dynamics of photoconductivity relaxation,” *J. Appl. Phys.*, vol. 107, no. 4, pp. 044507–044507–9, Feb. 2010.
- [86] A. E. Jiménez-González, J. A. Soto Urueta, and R. Suárez-Parra, “Optical and electrical characteristics of aluminum-doped ZnO thin films prepared by solgel technique,” *J. Cryst. Growth*, vol. 192, no. 3, pp. 430–438, Sep. 1998.
- [87] M.-W. Chen, J. R. D. Retamal, C.-Y. Chen, and J.-H. He, “Photocarrier relaxation behavior of a single ZnO nanowire UV photodetector: effect of surface band bending,” *IEEE Electron Device Lett.*, vol. 33, no. 3, pp. 411–413, Mar. 2012.
- [88] H. Kind, H. Yan, B. Messer, M. Law, and P. Yang, “Nanowire Ultraviolet Photodetectors and Optical Switches,” *Adv. Mater.*, vol. 14, no. 2, pp. 158–160, 2002.
- [89] M. L. Lu, C. H. Lin, and Y. F. Chen, “Enhanced photocurrent gain and spectrum range based on the composite consisting of SnO<sub>2</sub> nanowires and CdSe quantum dots,” *Appl. Phys. Lett.*, vol. 99, no. 8, Aug. 2011, Art. no. 081109.
- [90] X. Xu, C. Xu, and J. Hu, “High-performance deep ultraviolet photodetectors based on ZnO quantum dot assemblies,” *J. Appl. Phys.*, vol. 116, no. 10, Sep. 2014, Art. no. 103105.
- [91] Z. Jin *et al.*, “Graphdiyne:ZnO nanocomposites for high-performance UV photodetectors,” *Adv. Mater.*, vol. 28, no. 19, pp. 3697–3702, 2016.
- [92] P. Ivanoff Reyes, C.-J. Ku, Z. Duan, Y. Xu, E. Garfunkel, and Y. Lu, “Reduction of persistent photoconductivity in ZnO thin film transistor-based UV photodetector,” *Appl. Phys. Lett.*, vol. 101, no. 3, Jul. 2012, Art. no. 031118.
- [93] D. Eger, Y. Goldstein, and A. Many, “Oxygen chemisorption and photodesorption processes on ZnO surfaces,” *RCA Rev.*, vol. 36, no. 3, p. 508, Sep. 1975.
- [94] A. M. P. Santos and E. J. P. Santos, “Pre-heating temperature dependence of the c-axis orientation of ZnO thin films,” *Thin Solid Films*, vol. 516, no. 18, pp. 6210–6214, Jul. 2008.
- [95] L. Znaidi, “Sol–gel-deposited ZnO thin films: A review,” *Mater. Sci. Eng. B*, vol. 174, no. 1, pp. 18–30, Oct. 2010.
- [96] P. Sagar, P. K. Shishodia, and R. M. Mehra, “Influence of pH value on the quality of sol–gel derived ZnO films,” *Appl. Surf. Sci.*, vol. 253, no. 12, pp. 5419–5424, Apr. 2007.
- [97] T. Yao and S.-K. Hong, Eds., *Oxide and Nitride Semiconductors: Processing, Properties, and Applications*, vol. 12. Berlin, Germany: Springer, 2009.
- [98] S. S. Lin, J. H. Song, Y. F. Lu, and Z. L. Wang, “Identifying individual n- and p-type ZnO nanowires by the output voltage sign of piezoelectric nanogenerator,” *Nanotechnology*, vol. 20, no. 36, Aug. 2009, Art. no. 365703.
- [99] H. Morkoç and Ü. Özgür, *Zinc Oxide: Fundamentals, Materials and Device Technology*. Federal Republic of Germany: Wiley, 2009.
- [100] D. C. Look *et al.*, “Electrical properties of bulk ZnO,” *Solid State Commun.*, vol. 105, no. 6, pp. 399–401, Feb. 1998.
- [101] S. Lettieri, L. Santamaria Amato, P. Maddalena, E. Comini, C. Baratto, and S. Todros, “Recombination dynamics of deep defect states in zinc oxide nanowires,” *Nanotechnology*, vol. 20, no. 17, Apr. 2009, Art. no. 175706.
- [102] L. Zhou *et al.*, “A High-Resistivity ZnO Film-Based Photoconductive X-Ray Detector,” *IEEE Photonics Technol. Lett.*, vol. 31, no. 5, pp. 365–368, Mar. 2019.
- [103] Q. Humayun, M. Kashif, and U. Hashim, “Area-selective ZnO thin film deposition on variable microgap electrodes and their impact on UV sensing,” *J. Nanomater.*, vol. 2013, Jun. 2013, Art. no. 301674.

- [104] S.-J. Young, C.-C. Yang, and L.-T. Lai, "Review - growth of Al-, Ga-, and In-doped ZnO nanostructures via a low-temperature process and their application to field emission devices and ultraviolet photosensors," *J. Electrochem. Soc.*, vol. 164, no. 5, pp. B3013–B3028, Dec. 2016.
- [105] V. Dwivedi, P. Srivastava, and G. Vijaya Prakash, "Photoconductivity and surface chemical analysis of ZnO thin films deposited by solution-processing techniques for nano and microstructure fabrication," *J. Semicond.*, vol. 34, no. 3, Mar. 2013, Art. no. 033001.
- [106] G. Konstantatos *et al.*, "Hybrid graphene-quantum dot phototransistors with ultrahigh gain," *Nat. Nanotechnol.*, vol. 7, no. 6, pp. 363–368, May 2012.

## APPENDIX A SUPPLEMENTAL FILES

### A.1 Permissions for Figure 3

This file contains license details and terms and conditions for the reproduction of the reprinted figure in Figure 3 of this dissertation.

**File name:** Review Paper.pdf

**File type:** Portable Document Format (PDF)

**File size:** 90.9KB

**Required application software:** Adobe Acrobat or any standard PDF viewer

**Special hardware requirements:** None

### A.2 Permissions for Figure 5

This file contains license details and terms and conditions for the reproduction of the reprinted figure in Figure 5 of this dissertation.

**File name:** Melnick.pdf

**File type:** Portable Document Format (PDF)

**File size:** 87.6KB

**Required application software:** Adobe Acrobat or any standard PDF viewer

**Special hardware requirements:** None

### A.3 Permissions for Figure 32 (c)

This file contains license details and terms and conditions for the reproduction of the reprinted figure in Figure 32 (c) of this dissertation.

**File name:** Competitive Surface Effects.pdf

**File type:** Portable Document Format (PDF)

**File size:** 88KB

**Required application software:** Adobe Acrobat or any standard PDF viewer

**Special hardware requirements:** None